

NORTHWESTERN UNIVERSITY

Elasticity of Heterogeneous Gels

A DISSERTATION

SUBMITTED TO THE GRADUATE SCHOOL  
IN PARTIAL FULFILLMENT OF THE REQUIREMENTS

for the degree

DOCTOR OF PHILOSOPHY

Field of Materials Science and Engineering

By

Shuangping Liu

EVANSTON, ILLINOIS

December 2017

© Copyright by Shuangping Liu 2017

All Rights Reserved

## Abstract

Elasticity of Heterogeneous Gels

Shuangping Liu

Gels are three-dimensional polymer networks capable of absorbing a large amount of solvent molecules subject to various external stimuli (pH, temperature, light, etc.). They exhibit a rich mechanical behavior and prominent nonlinearity owing to their high flexibility, stimuli-responsiveness and superabsorbency. More compelling are the intriguing morphologies and novel functionalities achieved by introducing mechanical heterogeneities to an otherwise homogeneous gel. The misfit between heterogeneous components can cause mechanical instabilities that generate complex shapes such as creases, wrinkles, folds and helices. These buckling structures have broad engineering applications, and are also important model systems to understand the shape generation in biological bodies. Additionally, microstructural heterogeneities incorporated into the original gel networks can endow the gel with strong mechanical anisotropy, high toughness and high modulus. Such composite gels are particularly attractive as novel biomaterials due to their structural similarities to many biological systems in nature.

To understand the large deformation behavior and mechanical instabilities of gels with heterogeneities, we employ a finite element approach to investigate three systems with different architectures. The first system regards to a complex contact deformation of an elastomeric pyramid

array which is widely adopted in advanced nanopatterning techniques. Simple scaling laws of the deformation are established and compared with existing experiments. We further show that the distinct deformed shape of the pyramid plays a decisive role in producing the previously unexplained photoresist patterns. In the second system, the mechanical instability in a simple heterogeneous structure is considered. In a bistrrip gel with different prestrains in each strip, perversions and helices can emerge when the ends of the bistrrip approach with each other. Perversions serve as generic domain walls that connect states of opposite chirality. Here we focus on numerical analysis of the intrinsic properties of perversions, including the strain energy condensation over perversions, the repulsive nature of the perversion-perversion interaction and the coalescence of perversions. These findings have implications to the understanding of relevant biological motifs. Finally, we explore the anisotropic contraction of hydrogels reinforced by aligned fibrous heterogeneities, inspired by the recent experimental work of Chin *et. al.* Several strategies are proposed to improve the contraction anisotropy based on Flory-Rehner theory and finite element simulations. The numerical analysis indicates an increasing of contraction anisotropy when the hydrogel is prestretched along the fiber direction. Simulations further show that the contraction anisotropy can be maximized by tuning the structure parameters of the embedded fibers.

## Acknowledgements

First and foremost, I would like to thank my advisor Professor Monica Olvera de la Cruz, not only for her continuous support of my Ph.D. study and research, but also for her patience, motivation, enthusiasm and immense knowledge. Without her guidance and persistent encouragement, this work would never have been successfully completed. I am also grateful to the rest of my thesis committee, Professor John Marko, Professor Peter Voorhees and Professor Kenneth Shull, for their time, interest, and insightful comments.

I would like to express my gratitude to all the former and current members of the Monica Olvera de la Cruz group. Special thanks go to Professor Srikanth Patala, for his early mentorship that lay the foundation of this entire thesis; Professor Zhenwei Yao, for his deep knowledge in elasticity and geometry; Dr. Kevin Kohlstedt, for his unfailing technical support on cluster computing. I would especially thank Dr. Ting Li, who introduced me to the group five years ago.

I would like to thank my other collaborators for their experimental support and stimulating discussions: Kevin Chiou, Stacey Chin, Dr. Christopher Synatschke, Dr. Rikkerd Nap, Dr. Yu Zhou, Professor Samuel Stupp, Professor Zhuang Xie and Professor Keith Brown.

Last but not least, I would like to thank my family. This journey would not have been possible without their encouragement and unconditioned love. I am also deeply indebted to my wife, Yixuan Yuan, for her support, patience and sacrifice throughout this long-term study.

## Contents

Abstract	3
Acknowledgements	5
List of Tables	8
List of Figures	9
Chapter 1. Introduction	19
1.1. Background and Motivation	19
1.2. Finite Element Approach	25
1.3. Outline of Research	32
Chapter 2. Deformation of Elastomeric Pyramid Pen Arrays in Cantilever-free Scanning Probe Lithography	34
2.1. Introduction	34
2.2. Model	36
2.3. Implementation of the Finite Element Model	38
2.4. Results and Discussion	41
2.5. Conclusions	50
Chapter 3. Emergent Perversions in the Buckling of Heterogeneous Elastic Strips	52
3.1. Introduction	52
3.2. Model	54

3.3. Implementation of the Finite Element Model	56
3.4. Results and Discussion	59
3.5. Conclusions	68
Chapter 4. Anisotropic Contraction of Fiber-Reinforced Hydrogels	70
4.1. Introduction	70
4.2. Flory-Rehner theory	72
4.3. Anisotropic contraction of a uniaxially constrained hydrogel	75
4.4. Anisotropic contraction of fiber-reinforced hydrogels: finite element simulations	82
4.5. Conclusions	94
Chapter 5. Summary and Future Work	95
5.1. Summary	95
5.2. Recommended Future Work	96
Bibliography	99
Curriculum Vitae	117
Appendix A. The Flory-Huggins Parameter of Poly(ethlyene oxide) (PEO) in Aqueous Solutions	119
Appendix B. UHYPER Subroutine for Hydrogels	122

## List of Tables

2.1	Parameters for finite element modeling of the compression of the elastomeric pyramid array. The notation of the geometrical parameters follows the same as Fig. 2.1. The vertices of the geometry in Fig. 2.2 are used to represent the faces for the boundary conditions.	40
3.1	Parameters for finite element modeling of the postbuckling of a bistrrip. The bistrrip is assumed to be longitudinally oriented to $z$ -axis. The notation of the geometrical parameters follows the same as Fig. 3.1.	57
4.1	Parameters for finite element modeling of the fiber-reinforced hydrogel. The notation of the geometrical parameters follows the same as Fig. 4.4.	88

## List of Figures

1.1	Mechanical instabilities of gels with heterogeneities. (a) Creases and wrinkles present in the simulation of the gyrification of human brain using bilayered structure. Reprinted with permission from Macmillan Publishers Ltd: Nature Physics [1], copyright 2016. (b) Ripple patterns formed in a swelling gel with radial gradient of monomer concentrations [2]. Reprinted with permission from AAAS. (c) and (d) Formation of folds and ridges on a bilayered gel with misfit prestrains between the two layers [3]. Copyright 2015, with permission from Elsevier. (e) Helices and a perversion formed in a bistrrip with a misfit prestrain.	20
1.2	Schematic of the buckling of a bilayered film with different prestrains. (a) Schematic of the bilayered structure. (b) Bending instability with inner radius $R$ . (c) Wrinkling instability with amplitude $A$ and wavelength $\lambda$ . Reprinted with permission from [4], copyright 2009 by the American Physical Society.	23
1.3	Flow chart for buckling analysis in the FEM.	31
1.4	Algorithms employed in postbuckling analysis. (a) Newton-Raphson algorithm. The searching efficiency is limited at the maximum point of the loading-displacement curve. (b) Modified Riks method.	32
2.1	Schematics of our model for an elastomeric pyramid array. (a) Schematic structure of the pyramid pen array adopted in cantilever-free SPL. (b) Illustration of the loading procedure in our simulations: a rigid substrate is	

- compressed against an elastomeric pyramid array. (c) Schematic geometry of a single pyramid contained in a unit cell with periodic boundary conditions. 37
- 2.2 The geometry and mesh of the finite element model for an elastomeric pyramid array. (a) The geometry of a quarter of the unit cell. The loading and boundary conditions are listed in Table 2.1. (b) The partition method of the texahedron. (c) The hexahedral mesh of the texahedron. 39
- 2.3 The simulated deformation of an elastomeric pyramid under compression. (a) The snapshots of the deformation process with the increasing compression displacement (normalized by  $H$ ). (ii) – (v) demonstrate the distributions of von Mises stress in the cross-section illustrated in (i). The elastomeric base is not displayed in (i) and (vi). (b) The normalized width of the contact surface ( $\tilde{l}_c$ ) as a function of the normalized compression displacement ( $\tilde{d}$ ). The fitting parameters are shown in the upper right corner. All the simulations in (a) and (b) are performed with  $L = 8 \mu\text{m}$  and  $G = 1.0 \text{ MPa}$ . 42
- 2.4 The scaling behaviors of the normalized width of the contact surface  $\tilde{l}_c$  in terms of the compression force  $f$ . (a)  $\tilde{l}_c$  as a function of  $f^{1/2}$  for different initial shear moduli of the elastomeric material. Linear fittings are performed for all of the five data sets and shown as straight lines; all  $R^2 > 0.999$ .  $L = 8 \mu\text{m}$  in all the simulations. (b) The linear fitting of the experimental data (redrawn from Ref. [5]) to the scaling  $l_c \sim f^{1/2}$ . 44
- 2.5 (a) The normalized width of the contact surface  $\tilde{l}_c$  as a function of the normalized compression displacement  $\tilde{d}$  for different inter-pyramid distances  $W$ . The bottom right inset shows the linear relationship between  $\tilde{l}_c$  and the square root of the compression force ( $f^{1/2}$ ) for all the inspected  $W$ . (b) The

cross-sectional view of the deformed pyramid with  $W = 1.5L$  (left) and  $W = 8.0L$  (right).  $\tilde{d} = 0.71$  in both cases. The position of the inspected cross-section is the same as in Fig. 2.1a. The dashed contours depict the undeformed shape of the pyramid. The arrows indicate the separation between the deformed free surface of the base and the substrate. All the simulations in (a) and (b) are performed with  $L = 8 \mu\text{m}$  and  $G = 1.0 \text{ MPa}$

45

2.6

The normalized width of the contact surface  $\tilde{l}_c$  as a function of the normalized compression displacement  $\tilde{d}$  for different thicknesses ( $t$ ) of the base. The bottom right inset shows the linear relationship between  $\tilde{l}_c$  and the square root of the compression force ( $f^{1/2}$ ) for all the inspected  $t$ .  $L = 8 \mu\text{m}$ ,  $G = 1.0 \text{ MPa}$ .

46

2.7

(a) The shape of the contact surface determined by the contact pressure.  $\tilde{d} = 0.8$ ,  $L = 8 \mu\text{m}$ ,  $G = 1.0 \text{ MPa}$ . (b) Lateral view of the FDTD simulation layout to model the patterning process of the apertureless BPL technique. The annotated red lines in the photoresist layer represent the three two-dimensional monitors to record the light intensity. (c) Left: the experimental photoresist patterns generated by the apertureless BPL technique. Copyright Wiley-VCH Verlag GmbH & Co. KGaA. Reproduced with permission from Ref. [6]. Feature sizes are  $3.40 \mu\text{m}$ ,  $2.58 \mu\text{m}$  and  $1.26 \mu\text{m}$  from top to bottom. Scale bar:  $2 \mu\text{m}$ . Right: near-field intensity profiles generated by FDTD simulations using the irregular shapes of the compressed pyramids. From top to bottom:  $l_c = 3.66 \mu\text{m}$ ,  $2.44 \mu\text{m}$ , and  $1.22 \mu\text{m}$  respectively. From left to right: the intensity profiles recorded by the top, middle and bottom monitors in the FDTD simulations. Scale bar:  $2 \mu\text{m}$ .

48

- 2.8 The lateral view of the near-field intensity profiles of the photoresist layer generated by FDTD simulations using the shapes of the compressed pyramids. The inspected plane is a symmetric plane of the pyramid parallel to one of its bottom edges. From top to bottom:  $l_c = 4.24 \mu\text{m}$ ,  $2.83 \mu\text{m}$ , and  $1.41 \mu\text{m}$  respectively. Scale bar:  $0.5 \mu\text{m}$ . 49
- 2.9 Near-field intensity profiles generated by FDTD simulations using the shapes of truncated pyramids. From top to bottom:  $l_c = 4.24 \mu\text{m}$ ,  $2.83 \mu\text{m}$ , and  $1.41 \mu\text{m}$  respectively. From left to right: the intensity profiles recorded by the top, middle and bottom monitors in the FDTD simulations. Scale bar:  $2 \mu\text{m}$ . 49
- 3.1 The illustration of the bistrip model. (a) shows a typical perversion arising in an otherwise uniform helix (the upper figure) by controlling the boundary condition. (b) illustrates the bistrip model we used in the simulation. Strip A has the same cross section as strip B but shorter length in the initial state. Strip A is stretched and glued to strip B; both strips have the same length. One end of the bistrip system is fixed while the other end is allowed to translate but forbidden to rotate. (c) shows the first 5 buckling modes from eigenvalue buckling analysis. 54
- 3.2 Paper experiments to illustrate that the number of perversions on the helical system is not geometrically constrained. By grabbing and rotating a point on the initially straight paper band (a), a perversion can be manually produced as shown in (b). Further rotation of the perversion in (c) can generate more helices. 56

3.3

The effect of the displacement loading rate on the buckling shape of the bistrrip. The original lengths of the bistrrip in (a) and (b) are both 30.0 cm. (a) shows the buckling shape when the moving end stops at 23.3 cm. (b) shows the buckling shape at 23.3 cm while the end-to-end distance will continue shrinking to 9.0 cm.

57

3.4

The energy condensation in the perversion of the bistrrip system. (a) The formation and evolution of one perversion with the reduction of the strip length  $L$ ,  $w = 5$  mm,  $h = 3$  mm,  $L = 30$  cm and  $L' = L/3.5$  following the notation labeled in Figure 3.1b. The stress state of the bistrrip is characterized by the distribution of the scalar von Mises stress which is originally proposed to analyze the yielding of materials [7]. (b) The scaled strain energy profile of the strips in (a).  $\tilde{E}(n) = E(n) / \min_{\{n\}}\{E(n)\} - 1$ , where  $n$  labels the slab of elements as shown in the inset, and  $E(n)$  is the total strain energy of all these elements in the  $n$ -th slab. (c-f) The designed bistrrip system made of polyethylene and pre-stretched rubber strip to confirm the numerically observed energy condensation over the perversions. (c) and (d) show the shape of the bistrrip before and after buckling. The inset in (c) shows the featureless birefringence pattern of the initial bistrrip. The dashed red lines in (e) and (f) indicate the interface of the two strips. The different birefringence patterns in the perversion (e) and the helical (f) regions reflect the distinct strain energy distributions.

60

3.5

The buckling process of the bistrrip in Fig. 3.4a without normalizing the end-to-end distances.

61

3.6 Analysis of the strain energy distribution over the cross section at different sites demonstrates distinct energy transfer modes in the perversion and helical regions. The images below show the distribution of strain energy density ( $\epsilon_s$ ) at sites 1, 2 and 3 in the above image, respectively. The cross sections of strip A and B share different scale bars for the different energy density ranges. The middle inset in the circle depicts the region over the cross section where we inspect. 62

3.7 The formation and evolution of three perversions in a single bistrrip. (a) and (b) show the conformations and the corresponding strain energy distribution. (a) shows that the symmetric bucklings of the perversions are broken by the winding of the rightmost perversion where the strip length is reduced by 35%. In (b), the energy peaks labeled as 1, 2 and 3 correspond to the perversions formed in the buckling. The green arrow in the last figure indicates energy elevation and therefore repulsion between perversions. The geometric parameters of the strips are:  $w = 9$  mm,  $h = 3$  mm,  $L = 30$  cm and  $L' = L/3.5$  following the notation labeled in Fig. 3.1. 64

3.8 The formation and evolution of the perversions in a bistrrip where one of the strips is pre-compressed. (a) shows that eighteen perversions emerges when two ends of the bistrrip approaches. (b) In the right half of this bistrrip, the two perversions in the red dashed boxes annihilate and coalesce into the nearby perversion. (c) shows the ordered perversion line structure (labeled in the black dashed box) eventually formed when the moving end is close enough with the other one. The geometric parameters of the strip are:  $w = 3$  mm,  $h = 3$  mm,  $L = 30$  cm and  $L' = 75$  cm following the notation labeled in Fig. 3.1. 65

3.9 The evolution of the multiple perversions over a pre-compressed bistrip under stretching. The red dashed boxes in (a)-(c) is tracking a typical coalescence and annihilation of perversions. The total number of perversions consequently decreases as shown in (c)&(d). The length of the bistrip is becoming longer from (a) to (d). The geometric parameters of the strips are:  $w = 9$  mm,  $h = 3$  mm,  $L = 30$  cm and  $L' = L/3.5$  following the notation labeled in Fig. 3.1.

66

3.10 The cross section profiles of the strips inspected. The orange color of the strips indicate pre-stretching state; blue strips are stress-free in the initial state. As indicated by the ticks and crosses at the lowerright corner of each figure, (a)-(c) can produce helices and perversions, while (d)-(e) only deform to V-like shape. The geometric parameters of the strips are:  $w_0 = 9$  mm,  $w$  is the width after pre-stretching,  $w'$  can vary from  $5.4 \sim 6.3$  mm,  $h = 3$  mm,  $\tilde{h}' = 0.2$  mm. 67

4.1 Schematic plots of hydrogel contractions in response to increasing  $\chi$ . (a) A fiber-reinforced hydrogel is simplified as a uniform hydrogel subject to a uniaxial constraint along the fiber direction. (b) The contraction of a free-shrinking hydrogel (blue curve) and a uniaxially constrained hydrogel (red curve) with a fixed  $\lambda_{\parallel}$  ( $\alpha_{\parallel} = 1$ ). Both of the contractions start at the intersection point  $\phi_i = \phi'_i = \phi_c = \lambda_{\parallel}^{-3}$ . The arrows represent the direction of contractions along the  $\phi$  axis. 76

4.2 Contraction of uniaxially constrained hydrogels with prestrain  $\epsilon_{\parallel} \neq 0$ . (a) Schematic  $\chi \sim \phi$  plot of a uniaxially constrained hydrogel (red curve) undergoing a stronger volumetric contraction ( $\phi'_f/\phi'_i > \phi_f/\phi_i$ ) than a

free-shrinking hydrogel (blue curve) with  $\epsilon_{\parallel} > 0$ . The arrows represent the direction of the contractions along the  $\phi$  axis. (b) The upper bound of the contraction anisotropy ( $A_{\max}$ ) as a function of  $\phi_i$  and  $\epsilon_{\parallel}$  for different  $N\nu/V_m$ .  $\alpha_0 = 0.8$  in all subfigures. The longitudinally prestretched ( $\epsilon_{\parallel} > 0$ ) and precompressed ( $\epsilon_{\parallel} < 0$ ) states are separated by the dashed lines.  $\phi_i$  is limited within the range  $0 \sim 0.5$  because the final volume fractions  $\phi_f$  and  $\phi'_f$  must be less than 1 due to the specified  $\alpha_0$ .

80

4.3 Contraction of PEO hydrogels upon increasing temperature. (a) The contraction of a free-shrinking (blue curve) and a uniaxially constrained (red curve) PEO hydrogel as the temperature increases from  $T_i$  to  $T_f$ . (b) The upper bound of the contraction anisotropy ( $A_{\max}$ ) as a function of  $\phi_i$  and  $\epsilon_{\parallel}$  for a PEO hydrogel (left) and a generic hydrogel with  $\phi$ -independent  $\chi$  (right).  $N\nu/V_m = 0.002$  and  $\alpha_0 = 0.8$  in all subfigures.

81

4.4 Schematics of the model geometry and periodic boundary conditions in the finite element simulations. Top right: The unit cell in rectangular solid shape with one rigid fiber embedded. Top left: The smoothed end of the fiber using a semi-sphere with the same radius as the fiber's. The bottom illustration shows the correspondence between points on the opposite faces of a unit cell.

83

4.5 Verification of the implementation of the finite element user-defined subroutine. (a)  $\chi \sim \phi$  plot of a free swelling hydrogel. (b) The stress  $\sigma_3$  along the constrained direction for a uniaxially constrained hydrogel. At  $\phi = \phi_c$ , the stress vanished as expected. The inset illustrate the corresponding  $\chi \sim \phi$  curve of the uniaxially constrained hydrogel.

88

- 4.6 The transverse contraction ratio of the fiber-reinforced hydrogel as a function of the transverse fiber-fiber distance at  $L/l = 1$ . The fiber is modeled as a regular cylindrical rod throughout the hydrogel matrix rather than a smoothed one to avoid possible numerical difficulties. The simulations are performed with  $d = 10$  nm and  $L = l = 30$  nm. The lower limit is calculated from the contraction of a uniaxially constrained hydrogel illustrated in Fig. 4.1a with the same set of parameters as used in the finite element simulations. 89
- 4.7 The anisotropic contraction of the fiber-reinforced hydrogel at  $L/l > 1.0$ . (a) Schematic of the geometry to model the anisotropic contraction when  $L > l$ . (b-d) The transverse contraction ratio (b), the longitudinal contraction ratio (c) and the contraction anisotropy (d) as functions of the reduced transverse fiber-fiber distance ( $D/d$ ). The data for  $L/l = 1$  in (b) (dashed curves) are identical to Fig. 4.6 as  $\alpha_{\parallel} \equiv 1$ . The arrows in both (b) and (d) indicate the shifts of the minimum  $\alpha_{\perp}$  and the maximum  $A$ . The legend in (b) is also shared by (c) and (d). All the simulations are performed with  $d = 10$  nm and  $l = 200$  nm. 90
- 4.8 The von Mises stress distribution at (a)  $D/d = 2.5$  and (b)  $D/d = 6.0$ . Only one-eighth of unit cell is shown in the figure due the symmetry of the model. 91
- 4.9 The contraction anisotropy at different  $N\nu/V_m$ .  $L/l = 1.25$ . 92
- 4.10 The contraction anisotropy of the fiber-reinforced hydrogel as a function of the shape aspect ratio of the fiber ( $l/d$ ).  $L/l = 2.0$ . The corresponding transverse contraction ratio ( $\alpha_{\perp}$ , green line) and longitudinal contraction ratio ( $\alpha_{\parallel}$ , red line) are depicted in the inset. The simulations are performed with  $d = 10$  nm and  $D = 40$  nm. 93

## 5.1

Inverse design of surfaces using bilayers with orthotropic growing directions.

Three columns from left to right: the growing process of a snapdragon, a human face and a river horseshoe respectively. Within each column, the initial state (top), two intermediate states(middle) and final state (bottom) are shown. For each state, the growing factors of the top layer (left) and bottom layer (right) are illustrated. Adapted from [8]. Copyright 2017 National Academy of Sciences,

U.S.A.

## CHAPTER 1

### Introduction

#### 1.1. Background and Motivation

##### 1.1.1. Motivation

Gels are three-dimensional polymer networks permeated by solvent molecules [9]. Composed by physically or chemically crosslinked polymer chains, they behave as elastic solids macroscopically, while possessing liquid-like structures in atomic scale [10]. When immersed in an appropriate solvent, they can undergo reversible, dramatic volumetric swelling by absorbing large amount of solvent molecules. The high mechanical flexibility and the superabsorbency of gels lead to rich and unique mechanical behaviors, notably creases [11, 12] and wrinkles [13]. As such, gels have drawn significant interest in understanding the mechanics of complex soft matter in the past decades. Even more compelling is the fact that gels can swell in response to various external stimuli such as temperature, light, pH values and electric field [14, 15]. These environmentally sensitive gels, also known as “smart gels”, are promising materials in drug delivery [16], tissue engineering [17], bioseparation [18], biomimetics [19], biosensors [20], microfluidics [21], among many more.

By introducing mechanical heterogeneities into an otherwise homogeneous gel, more sophisticated morphologies and novel functionalities can be achieved. The misfit strain between heterogeneous components can lead to mechanical instabilities that generate richer two- or three-dimensional shapes such as ripples [2], folds [3], ridges [3], helices and perversions [22, 23] (Fig. 1.1). Owing to the flexible nature of gels, it is possible to repeatedly switch between the normal and buckled states, therefore allowing a variety of applications of these buckling structures in designing actuators [24],

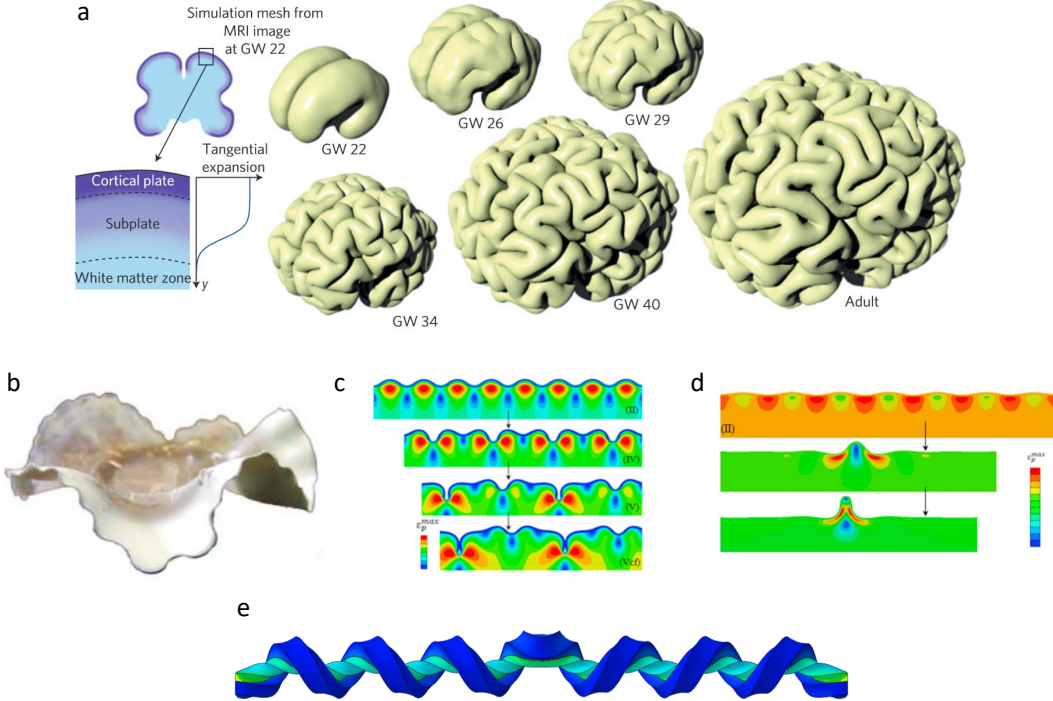


Figure 1.1. Mechanical instabilities of gels with heterogeneities. (a) Creases and wrinkles present in the simulation of the gyration of human brain using bilayered structure. Reprinted with permission from Macmillan Publishers Ltd: Nature Physics [1], copyright 2016. (b) Ripple patterns formed in a swelling gel with radial gradient of monomer concentrations [2]. Reprinted with permission from AAAS. (c) and (d) Formation of folds and ridges on a bilayered gel with misfit prestrains between the two layers [3]. Copyright 2015, with permission from Elsevier. (e) Helices and a persion formed in a bistrip with a misfit prestrain.

microrobotics [25], sensors [26] and flexible electronic devices [27]. These buckling structures also serve as important model systems to understand the growth and morphology evolution of many living organisms in mechanical perspective [28, 29, 1]. Studies on mechanics of gel swelling involving misfit heterogeneities have raised many intriguing questions that prompt interest in both fundamental science and practical applications.

Moreover, the mechanical response of gels can be substantially modified by massively incorporating micro- or nano-sized heterogeneities as fillers into the gel networks. During the past decades, successful efforts have been made to fabricate gels with strong mechanical anisotropy

by introducing various types of oriented fillers [30, 31, 32]. Such anisotropic gels are particularly appealing as novel biomaterials due to their striking structural similarities to many biological tissues like cornea [33], cartilages [34] and muscles [35]. Additionally, stiff micro- and nanofibers have been extensively used as mechanical reinforcement to amplify the mechanical performance of gels [30, 35, 36, 37], which is being actively explored for applications in soft robotics [38] and synthetic tissues [36]. Therefore, a better understanding of the mechanics of these gel composites allows researchers to design novel functional gels for more advanced applications by tuning the morphologies, arrangements and mechanical properties of the embedded heterogeneities.

### 1.1.2. Swelling of Gels

For neutral gels, the swelling is driven by the free energy of mixing of the polymer and solvent [10]. In contrast to a regular polymer solution, the cross-linked polymer chains in a gel do not dissolve when immersed in a good solvent. Instead, the polymer network expands by absorbing solvent molecules and eventually reaches an equilibrium state determined by the elasticity of the polymer chains which counteracts the volume expansion. This competition between the free energy of mixing and elasticity has been the starting point in the pioneering work of Flory and Rehner [39] to describe the swelling of gels. In their formulation, the free energy of mixing is given by the Flory-Huggins polymer solution theory [9], and the elastic energy is derived from rubber-like elasticity. The equilibrated volume of the gel network is therefore obtained by minimizing the total free energy, where the osmotic equilibrium of the gel must be achieved.

The classical Flory-Rehner theory can be generalized to more types of gels by including the free energy from other physical or chemical processes involved in the gel swelling. For polyelectrolyte gels, the electrostatic effects are often introduced as the entropic contribution of ions [14]. There are also efforts to incorporate the free energy of dielectric polarization [40] and the free energy

of dissociation of acidic groups for certain specific systems [41]. Other examples include the energetic contribution of photo-chemical reactions for photo-thermal gel [42], and the energy of magnetization for magnetic-sensitive ferrogels [43].

The most commonly adopted formulation of the elastic energy, first proposed by Wall and Flory [44], is derived based on Gaussian statistical mechanics of the polymer chains, and it possesses the similar form to the neo-Hookean hyperelastic model [45]. It is still widely used to model the stretch of gel networks and has achieved considerable success in the qualitative predictions of gel swelling. However, the Wall-Flory model does not account for the limited extensibility of polymer chains. Thus, alternative hyperelastic models should be considered when the network stretches are excessively large. For example, Deng and Pence have adopted the Mooney-Rivlin model to study the chemo-mechanical behavior of hydrogels [46]; Westbrook and Qi have incorporated the Arruda-Boyce model to simulate the responsive deformations of hydrogels [47]; Chester and Anand have followed a non-Gaussian statistical mechanical approach to capture the effect of limited chain extensibility in gel swelling [48].

Last but not least, the Flory-Rehner theory only describes the thermodynamic equilibrium of gel swelling. In reality, however, the swelling process involves both the evolution of the polymer network and the solvent migration. It takes significant time for the network and solvent molecules to reorganize upon sudden changes of the environment. A classical example, considered by Tanaka and Fillmore in 1979 [49], is the swelling of spherical gels moved from a bad solvent to a good one. It has been revealed that the characteristic time to equilibrate the spherical gel in a good solvent scales with the square of the sphere radius. Transient surface buckling may even occur during the swelling process if the volumetric variation is large enough [11]. In the present thesis, however, the main focus is on the thermodynamic equilibrium attained in a long time limit without considering the complicated swelling kinetics.

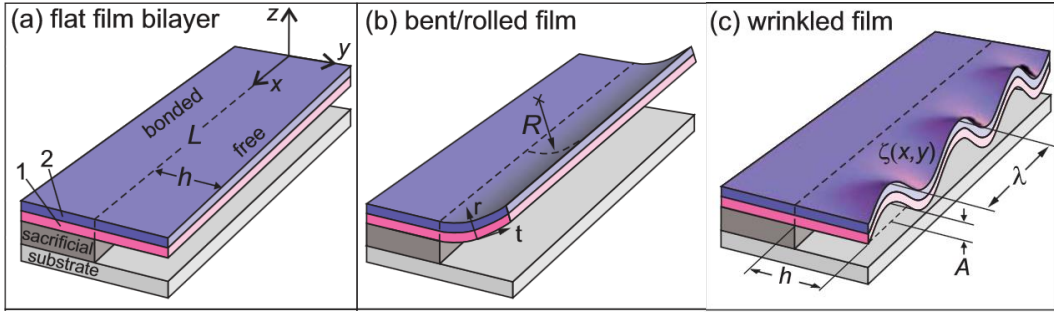


Figure 1.2. Schematic of the buckling of a bilayered film with different prestrains. (a) Schematic of the bilayered structure. (b) Bending instability with inner radius  $R$ . (c) Wrinkling instability with amplitude  $A$  and wavelength  $\lambda$ . Reprinted with permission from [4], copyright 2009 by the American Physical Society.

### 1.1.3. Mechanical Instabilities of Heterogeneous Gels

Gels can undergo very large deformations when being stretched, compressed or twisted, which has long been explored since the early stages of polymer science. For example, recently developed hydrogels with high stretchability can be stretched to 10-20 times of their original lengths without rupture [50]. They also possess high resilience that enables them to quickly recover to their original shape upon release. Such capabilities allow them to conform with complex surface morphologies in a reversible fashion, which has drawn tremendous interest in novel technologies including molecular printing [51, 52], stretchable electronics [27], microfluidics [21] and beyond.

The high flexibility of gels, coupled with their swelling ability, can generate large stress and strain leading to mechanical instabilities, notably at the presence of heterogeneities. Significant researches have been devoted to the spontaneous buckling of bilayered gels, as they are simple and ubiquitous heterogeneous systems in both nature and engineering applications. For a bilayered gel composed by two attached flexible thin layers with different prestrains, if fixed at one end and free the other one (Fig. 1.2), either wrinkling or bending can occur depending on the prestrain difference [4]. The wrinkling instability has also been experimentally observed by introducing an

incompatible swelling instead of a prestrain difference between the gel layers [53]. In contrast, for a bilayered “ribbon” (also known as bistrip) consisting of a prestretched ribbon and a stress-free ribbon (see Fig. 1.2e), helices and perversions can be produced by moving the ends of the bistrip close enough with each other [22]. The shape evolution of this bistrip sheds light on the curling of growing plant tendrils [23]. Shape transitions between helices, twisted ribbons and helicoid are also numerically observed by tuning the geometric parameters and the prestrains [54, 55]. Moreover, by programming the geometry, prestrains, intrinsic curvatures, anisotropy, and swelling or shrinkage of bilayered gels [56, 57, 58, 59, 60], researchers are able to transform 2D patterns into complex 3D structures under diverse stimuli to mimic the shapes of flowers, leaves, and animal organs.

Theoretical methods to analyze the mechanical instabilities are based on minimization of the total strain energy based on linear elasticity. Linear stability analysis with equilibrium equations also serves as an important tool to obtain possible buckling modes and the critical parameters that destabilize the system. Nevertheless, the scope of these theoretical approaches is limited as the nonlinear mechanical responses of gels are usually not taken into account, and they are lacking in predicting post-buckling behaviors where large deformations are expected. Numerical methods such as finite element approach are required to overcome these limitations.

#### **1.1.4. Anisotropic Swelling of Composite Hydrogels**

Hydrogels are gels capable of absorbing large amount of water [9]. They possess high biocompatibility and structural similarities to natural biological tissues, making them particularly attractive in biomedical applications. Inspired by the anisotropic architectures of many biological tissues in plants [61, 62] and human being [33, 34, 35], heterogeneous fillers with high aspect ratio are often embedded into hydrogel matrices to realize anisotropic mechanical responses. The most widely used strategy to achieve this goal is to introduce mechanical reinforcement via oriented stiff fibers.

Due to the high stiffness of fibers and the bonding between fibers and polymer chains, the fiber-reinforced hydrogels have stronger resistance against swelling/shrinking and external mechanical loadings along the fiber direction. Another approach, recently developed by Kim *et. al.* [63], takes advantage of the electrostatic repulsion between cofacially aligned layers assembled by charged titania nanosheets embedded in hydrogels, which hinders the composite hydrogels from shrinking along the normal direction of the layers. Other types of fillers that impart anisotropy to hydrogels are also reported in previous studies, including 2D nanoplates [58], lamellar structures [31], porous structures [32], to name a few.

Although there is a voluminous literature on constitutive models for composite elastomers, notably fiber-reinforced elastomers [64, 65, 66], theoretical and numerical studies on the anisotropic swelling of composite hydrogels remain limited. Phenomenological constitutive models within the framework of the Flory-Rehner theory have been proposed recently [67, 68], which characterize the effect of heterogeneous fillers as an extra free energy. The size, shape and distributions of fillers and the hydrogel-filler interactions are not explicitly included in these models. Therefore, there are new opportunities to explore the impact of the microscopic-level information of fillers on the swelling behavior, which is important for designing composite hydrogels with the desired anisotropic response.

## 1.2. Finite Element Approach

The mechanical equilibrium of gels is formulated as boundary value problems of partial differential equations (PDEs). Due to the complex deformations and non-linear response of heterogeneous gels, analytical solutions of these PDEs are difficult to obtain in many situations. As such, the finite element method (FEM) is employed in the present thesis to numerically compute the approximate solutions. The basic idea of FEM is to discretize the problem domain into a collections of smaller

domains with simpler structures, and transform the PDEs and boundary conditions into a system of equations that can be solved via efficient and robust numerical techniques [69]. The mechanical simulations presented in this thesis are performed in the commercial software ABAQUS, which has strong capability of handling nonlinear and dynamic analysis, and provides great flexibility to customize the constitutive behavior of materials in depth. The general methodology of FEM is briefly reviewed in the following sections.

### 1.2.1. Variational Formulation

The force equilibrium of a deformable body is usually written in differential form:

$$(1.1) \quad \frac{\partial \boldsymbol{\sigma}}{\partial \mathbf{x}} + \mathbf{f} = 0$$

where  $\boldsymbol{\sigma}$  is the Cauchy stress tensor as a function of the displacements  $\mathbf{u}$ ,  $\mathbf{x}$  denote the spatial coordinates of the deformed configuration, and  $\mathbf{f}$  is the body force per unit volume. To obtain an approximate solution of  $\mathbf{u}$  for Eq. 1.1 by discretizing the problem domain, Eq. 1.1 is rewritten as an integral equation which is given by

$$(1.2) \quad \int_V \boldsymbol{\sigma} : \delta \mathbf{D} dV = \int_S \mathbf{t}^T \cdot \delta \mathbf{v} dS + \int_V \mathbf{f}^T \cdot \delta \mathbf{v} dV$$

where  $V$  is the volumetric domain,  $S$  is the surface bounding the domain,  $\mathbf{t} = \mathbf{n} \cdot \boldsymbol{\sigma}$ ,  $\delta \mathbf{v}$  is an arbitrary velocity field and  $\delta \mathbf{D}$  is the virtual strain rate (the rate of deformation). Indeed, Eq. 1.2 is nothing more than the principle of virtual work: for an arbitrary virtual velocity field, the rate of work done by the body forces and surface tractions equals the rate of strain energy generated by the internal stresses. In the context of FEM, Eq. 1.2 is termed as the variational formulation, or “weak form”, of Eq. 1.1, as it imposes less restrictions to the continuity of  $\mathbf{u}$  and its derivatives. Since the stress tensor  $\boldsymbol{\sigma}$  is usually related to the first derivative of  $\mathbf{u}$ , the accurate solution of Eq. 1.1 requires

the second derivative of  $\mathbf{u}$  to be continuous within the problem domain, which may not be satisfied when the problem domain is discretized. In contrast, such discontinuity is allowed in the variational formulation since it does not invalidate the integration procedure.

### 1.2.2. Discretization of Problem Domains

In principle, the solution of Eq. 1.2 belongs to a infinite-dimensional function space  $\mathcal{H}$ , known as Hilbert space, thus it is infeasible to find the solution by verifying an infinite number of candidate functions in  $\mathcal{H}$ . Instead, by discretizing the problem domains into smaller elements, we are able to search for the solution of Eq. 1.2 in a finite-dimensional function subspace of  $\mathcal{H}$ . The approximate solution can therefore be expressed as a linear combination of basis functions  $\mathbf{N}^n$ , i.e., any value within the element can be interpolated using the basis functions:

$$(1.3) \quad \mathbf{u} = \mathbf{N}_n u^n$$

Here the summation convention is adopted for the index  $n$ . Similar to Eq. 1.3, the virtual velocity field  $\delta\mathbf{v}$  can be expressed as

$$(1.4) \quad \delta\mathbf{v} = \mathbf{N}_n \delta v^n$$

Since Eq. 1.2 must hold for any  $\delta v^n$ , we therefore obtained a system of equilibrium equations that is able to be solved numerically. Assuming a linear elasticity and infinitesimal deformations, these equations can be written as a matrix equation:

$$(1.5) \quad K_{mn} u^m = F_n$$

where  $K_{mn}$  is determined by the basis functions, which is also known as the stiffness matrix, and  $F_n$  stems from the external mechanical loadings.

The most commonly used basis functions are Galerkin Basis functions. For a one-dimensional problem defined in a evenly discretized interval, they are given by

$$(1.6) \quad N_n(x) = \begin{cases} (x - x_{n-1})/d & x_{n-1} \leq x < x_n \\ (x_{n+1} - x)/d & x_n \leq x \leq x_{n+1} \\ 0 & \text{otherwise} \end{cases}$$

where  $d$  is the distance between adjacent points. For 2D and 3D problems,  $N_n$  is usually determined by the type of element used for discretization, and it can possess more sophisticated form than a simple generalization of Eq. 1.6 to higher dimensional spaces.

### 1.2.3. Nonlinear Effects in the FEM

Soft materials like gels exhibit highly nonlinear behaviors when undergoing significant deformations. In particular, the assumption of infinitesimal strain is invalid if there are remarkable differences between the original and deformed shapes. Let  $\mathbf{X}$  and  $\mathbf{x}$  be the coordinates of undeformed and deformed body respectively, and  $\mathbf{u}$  denotes the displacement field. The finite strain tensor (Lagrangian strain tensor) can be written in terms of the displacement gradient tensor

$$(1.7) \quad \mathbf{E} = \frac{1}{2} \left[ \left( \frac{\partial \mathbf{u}}{\partial \mathbf{x}} \right)^T + \frac{\partial \mathbf{u}}{\partial \mathbf{x}} + \left( \frac{\partial \mathbf{u}}{\partial \mathbf{x}} \right)^T \left( \frac{\partial \mathbf{u}}{\partial \mathbf{x}} \right) \right]$$

In linear elasticity, the last quadratic term of Eq. 1.7 is neglected in the limit of infinitesimal deformation. It is more fundamental to express  $\mathbf{E}$  in terms of the deformation gradient tensor

$\mathbf{F} = \partial\mathbf{x}/\partial\mathbf{X}$ :

$$(1.8) \quad \mathbf{E} = \frac{1}{2}(\mathbf{C} - \mathbf{I})$$

where  $\mathbf{C} = \mathbf{F}^T \mathbf{F}$  is known as the right Cauchy-Green tensor, and correspondingly the left Cauchy-Green tensor is defined as  $\mathbf{B} = \mathbf{F}\mathbf{F}^T$ .  $\mathbf{C}$  and  $\mathbf{B}$  have the same eigenvalues  $(\lambda_1^2, \lambda_2^2, \lambda_3^2)$  which are the square of the principal stretches [70]. Therefore, the strain invariants  $(I_1, I_2, I_3)$  of  $\mathbf{C}$  and  $\mathbf{B}$  are also identical,

$$(1.9) \quad \begin{aligned} I_1 &= \text{tr}\mathbf{B} = \lambda_1^2 + \lambda_2^2 + \lambda_3^2 \\ I_2 &= \frac{1}{2} [(\text{tr}\mathbf{B})^2 - \text{tr}\mathbf{B}^2] = \lambda_1^2\lambda_2^2 + \lambda_2^2\lambda_3^2 + \lambda_3^2\lambda_1^2 \\ I_3 &= \det \mathbf{B} = \lambda_1^2\lambda_2^2\lambda_3^2 \end{aligned}$$

Because the deformations of many isotropic soft materials are path-independent, i.e., these materials can recover to their original shape upon release of the external loadings, their constitutive behavior can be described using a strain energy density that only depends on the strain invariants  $(I_1, I_2, I_3)$ . Such materials are termed as *hyperelastic* materials [70], as aforementioned in section 1.1.2.

In the present thesis, the neo-Hookean hyperelastic model is mostly employed to characterize the constitutive behavior of gels. The strain energy density of an incompressible neo-Hookean solid is given by [70]

$$(1.10) \quad U = \frac{1}{2}G(I_1 - 3)$$

For consistency with linear elasticity, the constant  $G$  represents the “initial” shear modulus, i.e., the shear modulus at infinitesimal deformation ( $I_1 \rightarrow 3$ ). The Cauchy stress of neo-Hookean model can

be derived by differentiating the strain energy density [70]:

$$(1.11) \quad \boldsymbol{\sigma} = -p\mathbf{I} + 2G \left[ \frac{1}{2}(\mathbf{B} - \mathbf{I}) \right]$$

where  $p$  is the hydrostatic pressure determined by the external loading. In contrast, considering an incompressible linear elastic solid with the shear modulus  $\mu$ , its Cauchy stress is written as [71]

$$(1.12) \quad \boldsymbol{\sigma} = -p\mathbf{I} + 2\mu\boldsymbol{\epsilon}$$

where  $\boldsymbol{\epsilon}$  is the infinitesimal strain tensor. The comparison between Eq. 1.11 and 1.12 indicates that the incompressible neo-Hookean model essentially generalizes Hooke's law by replacing the infinitesimal strain tensor with finite strain tensor, therefore introducing nonlinearity in the constitutive behavior.

The nonlinear mechanical behavior of gels result in a huge system of nonlinear equilibrium equations after discretizing Eq. 1.2, rather than the simple form of Eq. 1.5. As such, solving the mechanical equilibrium states of soft materials generally requires algorithms with iterative solution procedures. In many commercial FEM packages, Newton-Raphson method and its variants are adopted due to their high efficiency and robustness. Details of the Newton-Raphson method can be found to Ref. [72].

#### 1.2.4. Buckling Analysis in the FEM

The general procedure of buckling analysis in the FEM is illustrated in Fig. 1.3 To investigate the mechanical instabilities of gels, the first step is to perform a linear pre-buckling analysis to determine the critical buckling load and initial buckling modes which can be rescaled as small imperfections in the postbuckling analysis to destabilize the system. By applying a small perturbation load, we assume a linear response from the inspected system such that the governing equations for the

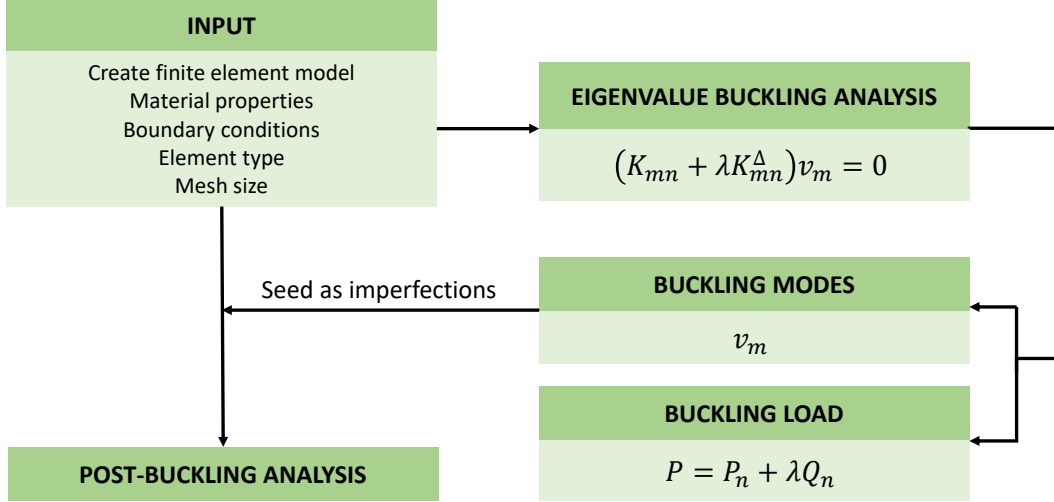


Figure 1.3. Flow chart for buckling analysis in the FEM.

buckling in the context of finite element discretization take the form of the eigenvalue problem:

$$(1.13) \quad (K_{mn} + \lambda K_{mn}^\Delta)v_m = 0$$

Here  $K_{mn}$  is the stiffness matrix at the base state, and  $K_{mn}^\Delta$  is the differential stiffness due to the perturbation. The eigenvector  $v_m$  of Eq. 1.13 is the buckling mode associated with the eigenvalue  $\lambda$ . In general, the lowest values of  $\lambda$  are of the most interest as they correspond to the most probable buckling modes that may emerge. The linear combination of these buckling modes can therefore be rescaled and added to the base state as a geometric imperfection. The critical buckling load is given by  $P = P_n + \lambda Q_n$  where  $P_n$  and  $Q_n$  denote the preload and perturbation load respectively.

Once the geometric imperfections are introduced to the system, the postbuckling analysis can then be performed to obtain the nonlinear solutions. However, the Newton-Raphson algorithm often has poor performance for postbuckling problems, because the stiffness matrix becomes singular at the load maximum point as shown in Fig. 1.4. The modified Riks method has been proposed to overcome this difficulty [72]. It traces the loading curve along an arc (or a spherical plane in multi-dimension space) so that it can produce a smooth solution of the buckling (Fig. ). For

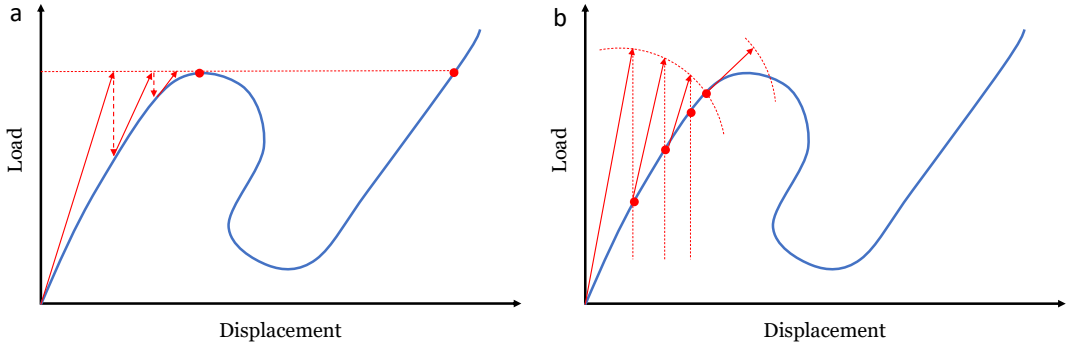


Figure 1.4. Algorithms employed in postbuckling analysis. (a) Newton-Raphson algorithm. The searching efficiency is limited at the maximum point of the loading-displacement curve. (b) Modified Riks method.

certain problems with dramatically large deformations, it is more effective to carry out a quasi-static analysis, which is essentially a dynamic analysis with a slow enough loading rate to minimize inertial effects and therefore delivers equilibrated solutions in the long time limit.

### 1.3. Outline of Research

The objective of my research is to understand the large deformation behavior and mechanical instabilities of soft matter systems, with special emphasis on the mechanics of heterogeneous gels and elastomers. The motivation and big picture of this thesis have been reviewed in the previous two sections of this chapter. The original work begins in Chapter 2 by investigating the large contact deformations of an elastomeric pyramid array, a soft periodic structure with broad applications in unconventional nanopatterning techniques. The distinct deformed shape of these pyramids is presented, and its pivotal role in generating the unusual features reported in the previous experimental study is validated using electromagnetic simulations. Chapter 3 explores the intrinsic properties of perversions that emerge from the helical instability of a heterogeneous bistrip gel. Rich physics of perversions is unveiled and analyzed through both simulations and experiments, including the strain energy condensation, perversion-perversion repulsion, hierarchical buckling

and coalescence of perversions. Chapter 4 proceeds to inspect the anisotropic contraction of fiber-reinforced hydrogels, inspired by the experimental work by Chin *et. al.* [73]. The approaches to optimizing the contraction anisotropy of the hybrid hydrogels are proposed and discussed. In the end, Chapter 5 concludes the thesis and recommended directions for future research.

## CHAPTER 2

# **Deformation of Elastomeric Pyramid Pen Arrays in Cantilever-free Scanning Probe Lithography**

## **2.1. Introduction**

Nanopattern fabrication in a high resolution, massively multiplexed and inexpensive manner is in great demand for a variety of biological, chemical synthesis and micro-electronics applications [74]. Cantilever-free scanning probe lithography (SPL) has recently been developed to address such challenges. It not only inherits the high resolution and precise controllability of SPL, but also makes a breakthrough toward a high-throughput nanopatterning approach [75, 76]. The cantilever-free architecture essentially replaces the expensive and delicate cantilevers in SPL with a low cost nano- or micro-scale pen array resting on an elastomeric film that adheres to a hard backing, allowing millions of pens to simultaneously write arbitrary patterns on the substrate. Based on this concept, different types of cantilever-free SPL techniques, including polymer pen lithography (PPL) [52], beam pen lithography (BPL) [77] and hard-tip soft-spring lithography (HSL) [78], have successively emerged as potent and versatile tools for nanopatterning applications in diverse fields [79, 80, 81, 82].

The morphology and material of the pen array undoubtedly play a decisive role in the performance of the cantilever-free architecture. Microscale elastomeric pyramid arrays, the first adopted pen structure in the development of cantilever-free SPL, have been extensively employed in previous work [52, 77, 6, 83] owing to their unique structural and mechanical properties. They can be easily fabricated using soft-lithography techniques in a well-controlled manner [84]. By anchoring the

base of the pyramid array to a hard backing, the co-planarity between the pyramids and the substrate is readily ensured for high precision lithographic operations. More importantly, due to the extremely small radius of curvature of the pyramid apex, the deformation scale of a microscale pyramid can vary from as small as sub-100 nanometers [52] to micrometers depending on the compressive force. In addition, the pyramidal structure naturally possesses better mechanical stability compared with the other structures where unexpected buckling behaviors are widely reported in former research [85].

Besides cantilever-free SPL, many other applications have also taken advantage of the distinct properties of elastomeric pyramid arrays to realize a variety of functions, notably by coupling the controllable deformations with other physics. In microcontact printing, a well-known soft lithography technique for micro- and nanofabrication, pyramidal polydimethylsiloxane (PDMS) stamps have long been adopted to obtain a more stable and reliable molecular printing process [51, 86, 87]. The recent development of highly sensitive resistive pressure sensors has demonstrated that a PDMS pyramid array coated with a conductive flexible layer can serve as a deformable electrode whose electrical resistance changes sensitively with the change of pressure [88, 89, 90]. For triboelectric nanogenerators, which harvest the mechanical energy through the triboelectrification between two contacting dissimilar materials, remarkable improvements of the performance can be achieved by using a deformable pyramid array as the interfacial microstructure [91, 92].

Analytical and numerical studies on the deformation of a single elastomeric pyramid have been conducted in previous research. The most intuitive and broadly used approach treats the deformed shape as a truncated pyramid [5, 93]. With this approximation, relationships between the width of the contact surface and the loading conditions can be readily established based on simple geometric analysis. In addition, Kim, *et. al.* have modeled the PDMS pyramids with cones to investigate the variation of the adhesive contact area under compression, assuming a small deformation that only

occurs at the apex of the pyramid [94]. Although these simplified analytical models are easy to understand and convenient to use, they do not fully capture the mechanical behavior and the irregular shape of the deformed pyramid. In order to improve our understanding, Jin, *et. al.* numerically explored the frictionless adhesive contact between a deformed PDMS pyramid and a glass substrate with different adhesion models [95]. Moreover, finite element simulations of a few specific systems involving deformed pyramid arrays have been performed to compare with the experimental data [86, 89, 96]. However, to the best of our knowledge, systematic studies on the deformation of an elastomeric pyramid array, especially the effect of the inter-pyramid interactions and the unique shape of the contact surface, are lacking.

In this paper, we develop a comprehensive numerical study on the compression of an elastomeric pyramid array in a non-adhesive and frictionless contact with a rigid substrate. For a single pyramid, the scaling laws of the width of the contact surface are established with respect to the compression displacement and force, and are compared with the available modeling and experimental results. By reducing the inter-pyramid distance and the thickness of the elastomeric base, we also inspect the deviation from these scaling laws for a pyramid array. Furthermore, the unique shape of the contact surface is investigated and employed in electromagnetic simulations to explain the unusual inhomogeneous BPL features reported in the previous study. Our findings bring insight into the fine control of the feature shape and patterning resolution in the common cantilever-free SPL techniques such as PPL, BPL and their variants, and may also potentially facilitate the design of other functional devices involving compressed elastomeric pyramid array.

## 2.2. Model

In present work, we use the following generic model to describe the compression of the pyramidal pen array in a typical lithographic operation of cantilever-free SPL. As illustrated in

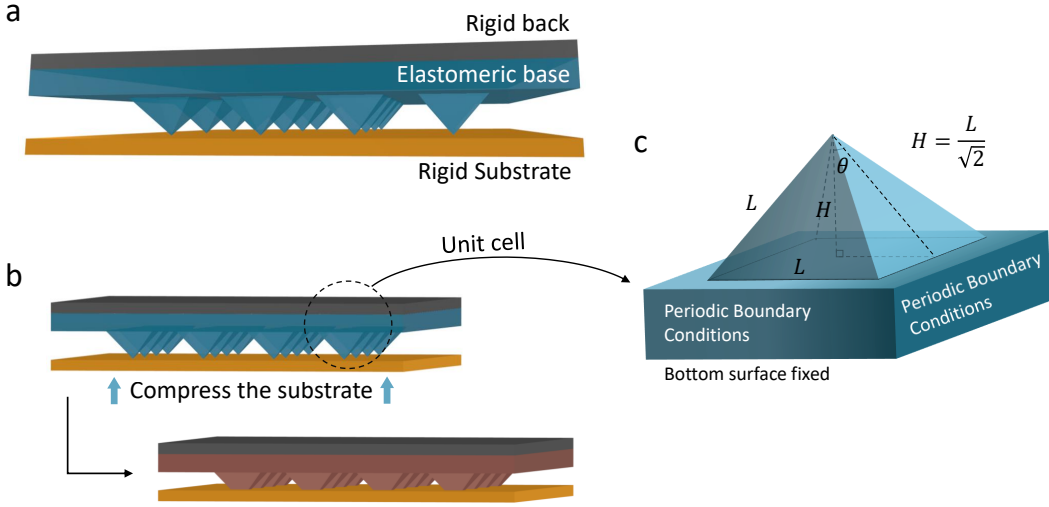


Figure 2.1. Schematics of our model for an elastomeric pyramid array. (a) Schematic structure of the pyramid pen array adopted in cantilever-free SPL. (b) Illustration of the loading procedure in our simulations: a rigid substrate is compressed against an elastomeric pyramid array. (c) Schematic geometry of a single pyramid contained in a unit cell with periodic boundary conditions.

Fig. 2.1a, we consider an elastomeric base patterned with a periodic array of pyramids that is anchored on a rigid backing and placed parallel to another rigid flat substrate. By externally controlling the distance between the base and the substrate, the pyramids deform responsively upon a conformal contact with the rigid substrate (see Fig. 2.1b). We represent the pyramid array as a two-dimensional square lattice of unit cells. Within each unit cell, an elastomeric pyramid is associated with a square base (Fig. 2.1c); both the pyramid and the base are made of the same material.

The geometry of a pyramid is defined by the width of the square bottom plane ( $l$ ) and the semi-apex angle ( $\theta$ ), as depicted in Fig. 2.1c. In the present study, we set  $\theta \equiv \arctan(1/\sqrt{2})$ , thus all the edges of the pyramid must possess equal length  $l$ , and the height of the pyramid  $H = l/\sqrt{2}$ . This value of  $\theta$  results from the particular shape of the square pyramidal pits in a silicon  $\langle 100 \rangle$  wafer used as the replica mold to fabricate the elastomeric pyramid array; such pyramidal pits are often

produced by anisotropically etching the wafer along the  $\langle 111 \rangle$  directions [97, 84]. Therefore, the semi-apex angle of the pyramid is well-defined by the angle between  $\langle 100 \rangle$  and  $\langle 111 \rangle$  directions.

By definition, the area of the contact surface, denoted by  $A_c$ , can be numerically estimated by accumulating the area with non-zero contact stresses. Experimentally, however, it is often convenient to characterize the contact area with the width of the contact surface (denoted by  $l_c$ ). For simplicity, we assume a frictionless and non-adhesive contact between the pyramid and the rigid substrate in our generic model. It is observed in our simulations that the friction has negligible effect on the force-displacement relationship of the pyramid: the overall difference between the frictionless contact and the contact with a large friction coefficient is less than 1%. On the other hand, using an adhesive contact may notably impact the mechanical behavior of the pyramid [95]. However, since the adhesion highly depends on the nature of the specific materials involved in the contact, we herein do not incorporate it into our model.

Considering the potentially large deformations of the pyramids, we employ the incompressible neo-Hookean model, which is the simplest hyperelastic model that can capture the elasticity of various elastomeric materials used for fabricating pyramid pens. Eq. 1.10 gives the strain energy density function of an incompressible neo-Hookean solid.

### 2.3. Implementation of the Finite Element Model

#### 2.3.1. Geometry and mesh

We resort to finite element analysis using the commercial code ABAQUS to track the deformations of the pyramid array. Non-linear static analyses are performed in *a quarter of* the unit cell considering the four-fold symmetry of the geometry. As illustrated in Fig. 2.2a, the geometry built in the FEM consists of a tetrahedron and a rectangular block, and the substrate is modeled as a rigid analytical surface which has an initial contact with the apex of the tetrahedron. In particular, the tetrahedron

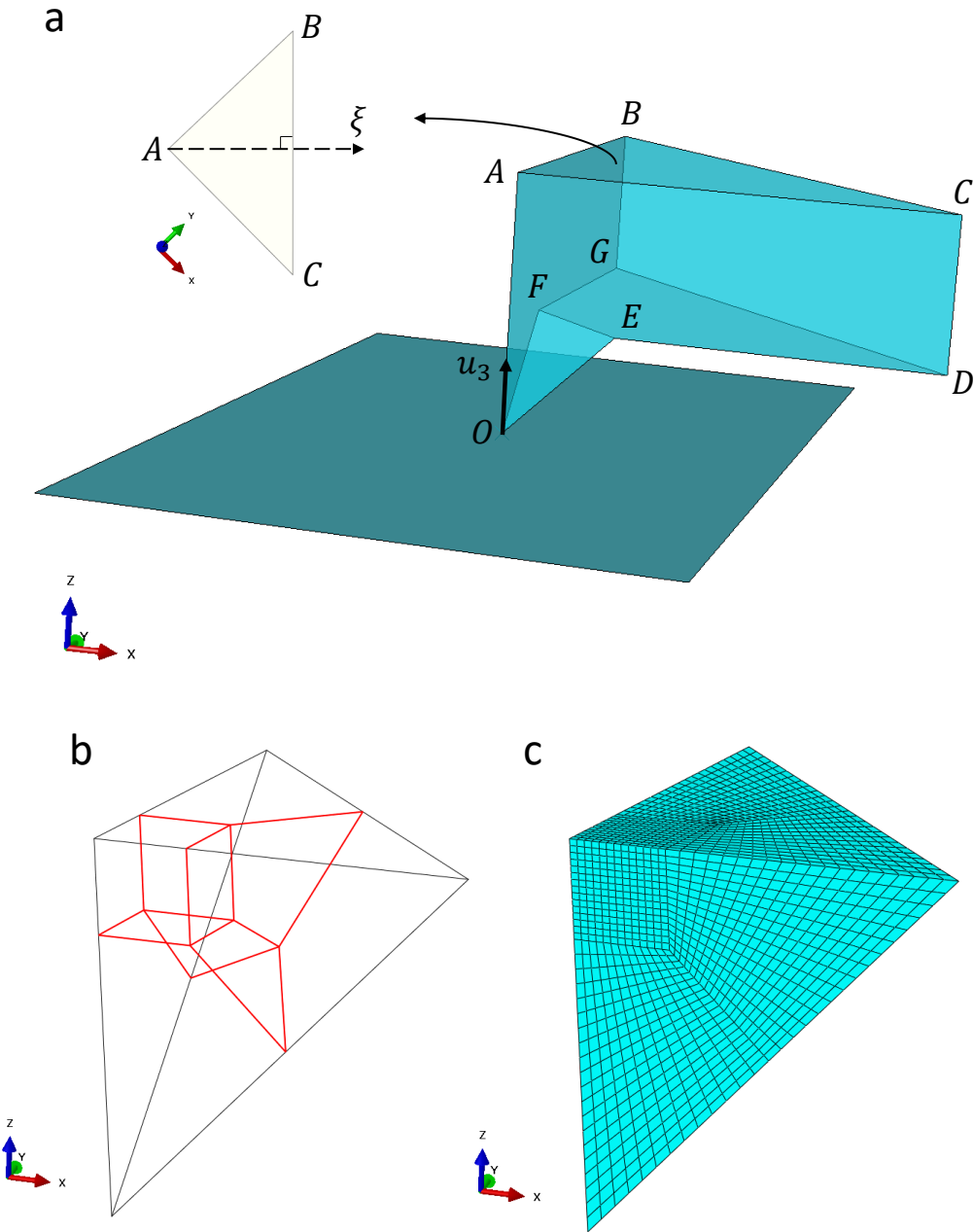


Figure 2.2. The geometry and mesh of the finite element model for an elastomeric pyramid array. (a) The geometry of a quarter of the unit cell. The loading and boundary conditions are listed in Table 2.1. (b) The partition method of the texahedron. (c) The hexahedral mesh of the texahedron.

Table 2.1. Parameters for finite element modeling of the compression of the elastomeric pyramid array. The notation of the geometrical parameters follows the same as Fig. 2.1. The vertices of the geometry in Fig. 2.2 are used to represent the faces for the boundary conditions.

<b>Geometry (<math>\mu\text{m}</math>)</b>		<b>Element</b>	
$L$ 8.0		C3D8R with enhanced hourglass control	
$H$ $L/\sqrt{2}$			
$W$ 64 (For a single pyramid)			
$t$ 32 (For a single pyramid)			
<b>Materials</b>		<b>Boundary conditions</b>	
$G$ Vary from 0.25 ~ 3.0MPa		$S_{ABC}$ Encasted $(\text{mdb.model[name].EncastreBC})$ $S_{OEF}$ and the substrate Nonadhesive and frictionless contact $S_{OACDE}$ Symmetric face $(\text{mdb.model[name].YsymmBC})$ $S_{OABGF}$ Symmetric face $(\text{mdb.model[name].XsymmBC})$ $S_{BCDG}$ Displacement $u_\xi = 0$ The substrate Displacement at the point $O$ : $u_1 = u_2 = 0$ , $u_3$ is non-zero. Rotations are not allowed.	

must be carefully meshed to ensure the precision and convergence of the simulations when the contact deformation becomes substantially large. Although it is natural to use tetrahedral elements to mesh the tetrahedron, the required mesh size has to be extremely small (millions of elements in total), which significantly raises the computational cost. A better choice is to construct the mesh with hexahedral elements which are expected to produce more accurate stress field with much less elements. However, the tetrahedron cannot be directly meshed with hexahedral elements, as ill-shaped elements are unavoidable in this situation, and convergence difficulties may occur. Indeed, the tetrahedron needs to be appropriately partitioned into hexahedrons which can be easily meshed using hexahedral elements. In Fig. 2.2b, six internal faces are introduced to partition the tetrahedron: each of these faces is determined by the geometric center of the tetrahedron and its vertical projections on two of the tetrahedron surfaces. A high quality hexahedral mesh is therefore achieved in Fig. 2.2c. This partitioning strategy can be implemented in ABAQUS

by directly connecting the vertices and crossing points following Fig. 2.2b, and constructing the faces and volumes accordingly. In the present study, the tetrahedron and the base are meshed using linear hexahedron structural elements (C3D8RH, the hybrid formulation is used due to the incompressibility of the material), and the mesh density is validated through convergence tests.

### 2.3.2. Loading and boundary conditions

The loadings and boundary conditions are illustrated in Fig. 2.2a and listed in Table 2.1. Periodic boundary conditions are imposed according to the geometric symmetry: the face  $S_{BCDG}$  will not undergo out-of-plane deformations. Indeed, all the nodes in  $S_{BCDG}$  should have the zero displacement along  $\xi$  direction (see the inset of Fig. 2.2a), as the  $S_{ABC}$  is anchored to a rigid back (encastred). In ABAQUS, this can be achieved by specifying a local coordinate system with  $x$ -axis pointing along  $\xi$  direction such that the displacement along the local  $x$ -axis can be manually set to zero. Additionally, it is worth mentioning that the discretization method for the contact surfaces  $x$  and the rigid substrate should be *node-to-surface*, which is suitable for the contact problem between a sharp point and a surface. Overall, by specifying the displacement of the rigid substrate toward the base, and meanwhile fixing the bottom of the base, the deformation of the system can be simulated to obtain the desired information of contact and the compression force on the substrate.

## 2.4. Results and Discussion

We start by investigating the deformation of a pyramid array with negligible boundary effects, i.e., both the width of each unit cell and the thickness of the base are much larger than the size of the pyramid. As shown in the snapshots of Fig. 2.3a, the pyramid is gradually pressed into the base due to the increasing compression displacement denoted by  $d$  (i.e. the displacement of the substrate), and meanwhile a concave deformation occurs on the associated base of the pyramid. In particular,

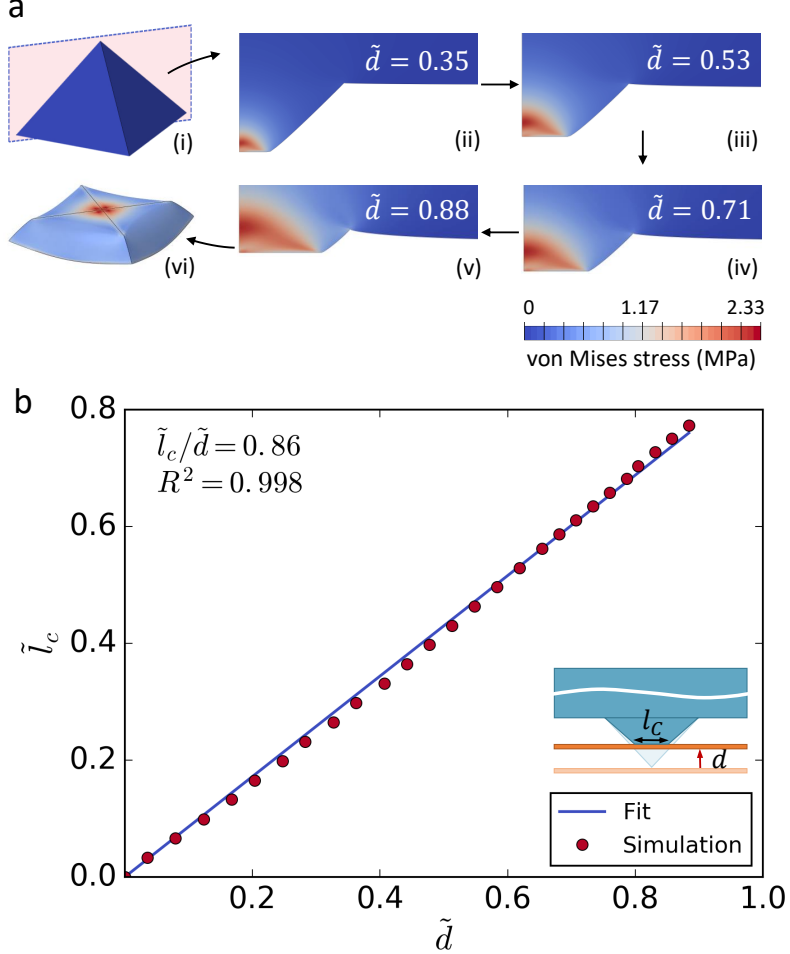


Figure 2.3. The simulated deformation of an elastomeric pyramid under compression. (a) The snapshots of the deformation process with the increasing compression displacement (normalized by  $H$ ). (ii) – (v) demonstrate the distributions of von Mises stress in the cross-section illustrated in (i). The elastomeric base is not displayed in (i) and (vi). (b) The normalized width of the contact surface ( $\tilde{l}_c$ ) as a function of the normalized compression displacement ( $\tilde{d}$ ). The fitting parameters are shown in the upper right corner. All the simulations in (a) and (b) are performed with  $L = 8 \mu\text{m}$  and  $G = 1.0 \text{ MPa}$ .

the growing contact area between the deformed pyramid and the substrate is observed; Fig. 2.3b shows that the normalized width of the contact surface ( $\tilde{l}_c = l_c/L$ ) increases linearly as a function of the normalized compression displacement ( $\tilde{d} = d/H$ ), thus

$$(2.1) \quad \tilde{l}_c \propto \tilde{d}$$

Exactly the same contact behavior is also found in simulations for pyramids of various sizes ( $8\mu\text{m} \leq L \leq 32\mu\text{m}$ ), thus Eq. 2.1 is size independent. The linear fitting in Fig. 2.3b gives  $\tilde{l}_c/\tilde{d} \approx 0.86$ , while a simple truncated pyramid geometry assumes  $\tilde{l}_c/\tilde{d} = 1 > 0.86$ , which therefore overestimates the width of the contact surface for a specified  $\tilde{d}$ .

Our simulations further show that the normalized width of the contact surface increases in proportion to the square root of the compression force against the pyramid (see Fig. 2.4a) for different values of the initial shear modulus, that is,

$$(2.2) \quad \tilde{l}_c \propto f^{1/2}$$

To validate the simulation results, Eq. 2.2 is fitted to the reported experimental data measured from the features fabricated by PPL [5]. A fairly good agreement is obtained, as shown in Fig. 2.4b. The discrepancies may arise partly from the fact that the feature size in PPL monotonically increases with the dwell time between the pyramid pen and the substrate [5]. For different values of dwell time and compression force, the feature size can deviate significantly from the real contact area. Besides, the absence of the adhesion between the pyramid and the substrate in our model may also contribute to the discrepancies. It has been demonstrated that enhancing the adhesion of the contact surface can lead to a substantial increase of  $\tilde{l}_c$  for a specified  $f$  [95]. It is worth noting that, in the previous study [5], the experimental data in Fig. 2.4b have been explained with an empirical model assuming a two-stage linear dependence of  $l_c$  on  $f$  based on the analysis of a simple elastic truncated pyramid. The discontinuous transition of the mechanical properties between the two stages has been attributed to the nonlinear constitutive response of the elastomeric material. In our simulations, however, the same scaling behavior of Eq. 2.2 is also observed when employing other constitutive models such as linear elastic and Mooney-Rivlin model. Therefore, we conclude that

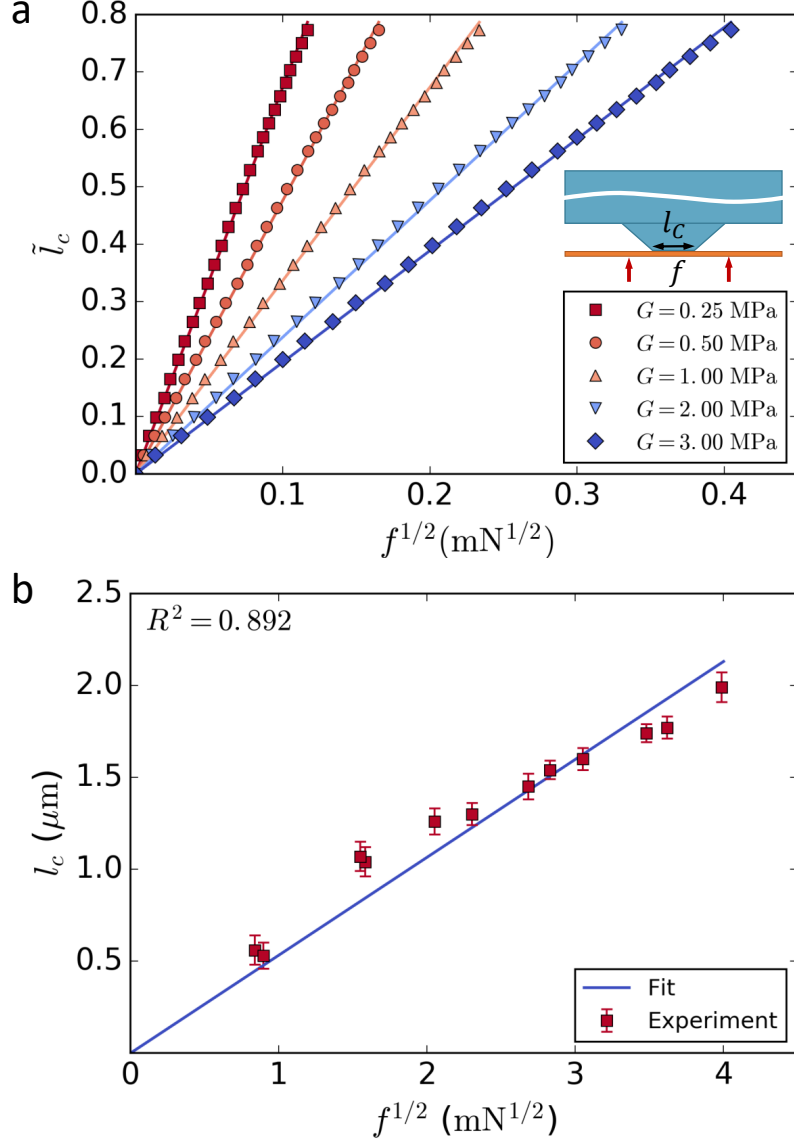


Figure 2.4. The scaling behaviors of the normalized width of the contact surface  $\tilde{l}_c$  in terms of the compression force  $f$ . (a)  $\tilde{l}_c$  as a function of  $f^{1/2}$  for different initial shear moduli of the elastomeric material. Linear fittings are performed for all of the five data sets and shown as straight lines; all  $R^2 > 0.999$ .  $L = 8 \mu\text{m}$  in all the simulations. (b) The linear fitting of the experimental data (redrawn from Ref. [5]) to the scaling  $l_c \sim f^{1/2}$ .

the scaling law of Eq. 2.2 is independent of the specific constitutive response of the elastomeric material composing the pyramid.

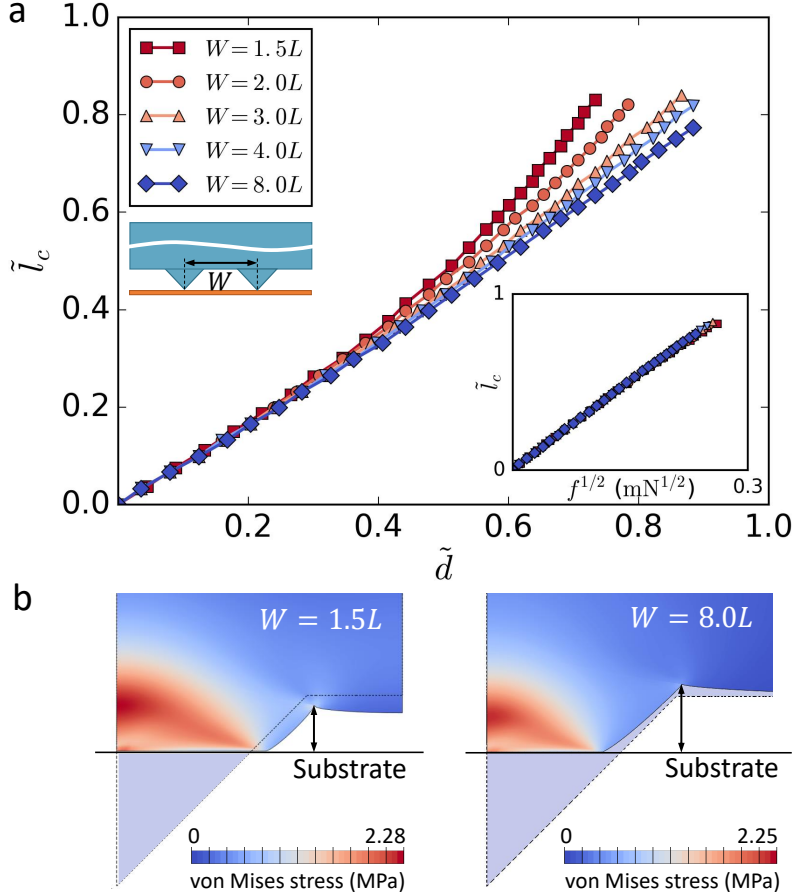


Figure 2.5. (a) The normalized width of the contact surface  $\tilde{l}_c$  as a function of the normalized compression displacement  $\tilde{d}$  for different inter-pyramid distances  $W$ . The bottom right inset shows the linear relationship between  $\tilde{l}_c$  and the square root of the compression force ( $f^{1/2}$ ) for all the inspected  $W$ . (b) The cross-sectional view of the deformed pyramid with  $W = 1.5L$  (left) and  $W = 8.0L$  (right).  $\tilde{d} = 0.71$  in both cases. The position of the inspected cross-section is the same as in Fig. 2.1a. The dashed contours depict the undeformed shape of the pyramid. The arrows indicate the separation between the deformed free surface of the base and the substrate. All the simulations in (a) and (b) are performed with  $L = 8 \mu\text{m}$  and  $G = 1.0 \text{ MPa}$

We further explore the deviations of the established scaling laws by varying the size of the unit cell (the inter-pyramid distance  $W$ ). Simulations show that  $\tilde{l}_c \propto f^{1/2}$  still holds for different values of  $W$  (see the inset of Fig. 2.5a), while the relationship between  $\tilde{l}_c$  and  $\tilde{d}$  presents substantial deviations from Eq. 2.1: when  $\tilde{d}$  is less than  $\sim 0.3$ , the deformation of the pyramid is mostly localized near the tip apex, thus  $\tilde{l}_c \propto \tilde{d}$  is still observed for all the inspected  $W$  (Fig. 2.5a). In

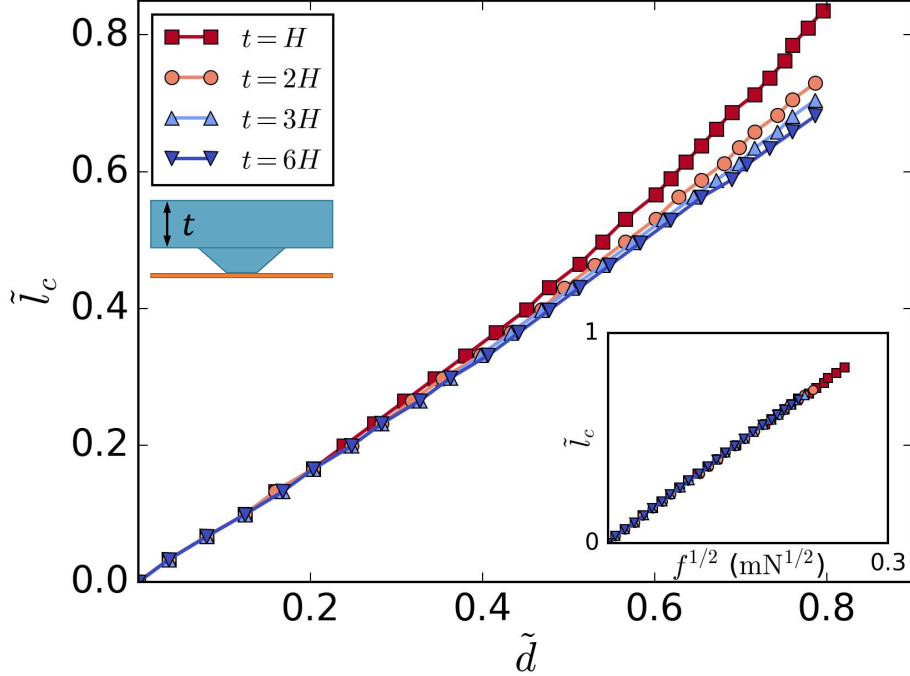


Figure 2.6. The normalized width of the contact surface  $\tilde{l}_c$  as a function of the normalized compression displacement  $\tilde{d}$  for different thicknesses ( $t$ ) of the base. The bottom right inset shows the linear relationship between  $\tilde{l}_c$  and the square root of the compression force ( $f^{1/2}$ ) for all the inspected  $t$ .  $L = 8 \mu\text{m}$ ,  $G = 1.0 \text{ MPa}$ .

the contrast, when  $\tilde{d} > 0.3$ ,  $\tilde{l}_c$  becomes significantly larger than predicted by Eq. 2.1, especially for smaller  $W$ . Such deviations arise from the deformation of the elastomeric base induced by the compression of the pyramid. The free surface of the base must at least partially move toward the substrate to compensate the lessened volume of the compressed pyramid; for smaller  $W$ , such responsive deformation becomes much more notable as can be identified in Fig. 2.5b, and it indeed propels the pyramid against the substrate, which promotes the compression of the pyramid and therefore enlarges the contact area. Consequently, we conclude that by decreasing the inter-pyramid distance, the width of the contact surface deviates toward larger values from the established scaling behavior  $\tilde{l}_c \propto \tilde{d}$ , notably at a large compression displacement.

Interestingly, similar deviations from the  $\tilde{l}_c \sim \tilde{d}$  scaling are also observed when varying the thickness of the base denoted by  $t$ , as shown in Fig. 2.6. However, the underlying mechanism is essentially different from above. For a specified compression displacement, a thinner base undergoes a larger strain on average near its connection with the pyramid, which in turn impedes the further compression of the pyramid; as such, it becomes more favorable for the deformation of the pyramid to develop along the lateral directions, hence leading to a larger contact area.

We note that the contact surface possesses a unique shape, which has also been reported in previous studies [93, 87, 95]. As shown in Fig. 2.7a, the edges of the contact surface are concave due to the recessed deformations of the lateral faces of the pyramid. Therefore, the total area of the contact surface ( $A_c$ ) must be less than  $l_c^2$ ; a rough estimation based on the discretized contact surface indicates that  $A_c/l_c^2 \approx 0.7$ . Such unique shape may lead to unexpected outcomes in the experiments sensitive to the shape of the contact surface. For example, the apertureless BPL technique, which generates photoresist patterns by directly delivering light through transparent, compressed pyramid arrays, sometimes produces inhomogeneous features with a rounded square hole in each of the feature center [6]. The simplified model with a truncated pyramid cannot fully explain this unusual phenomenon.

To address the cause of the these puzzling lithographic features, we perform finite-difference time-domain (FDTD) simulations with a commercial code (Lumerical FDTD solutions v.8.7.0) for both the compressed pyramids obtained from our FEA simulations and simple truncated pyramids. Specifically, a polarized plane wave pulse in time domain with wavelength ranging from  $300 \sim 500$  nm is incident normally from the elastomeric media to the pyramidal surface and the underlying photoresist layer (see Fig. 2.7b). The electric fields are monitored at the top, middle and bottom plane of the photoresist layer, and then fourier-transformed to frequency domain to generate intensity profiles for a specific wavelength (here a wavelength of 405 nm is inspected according to Ref. [6]).

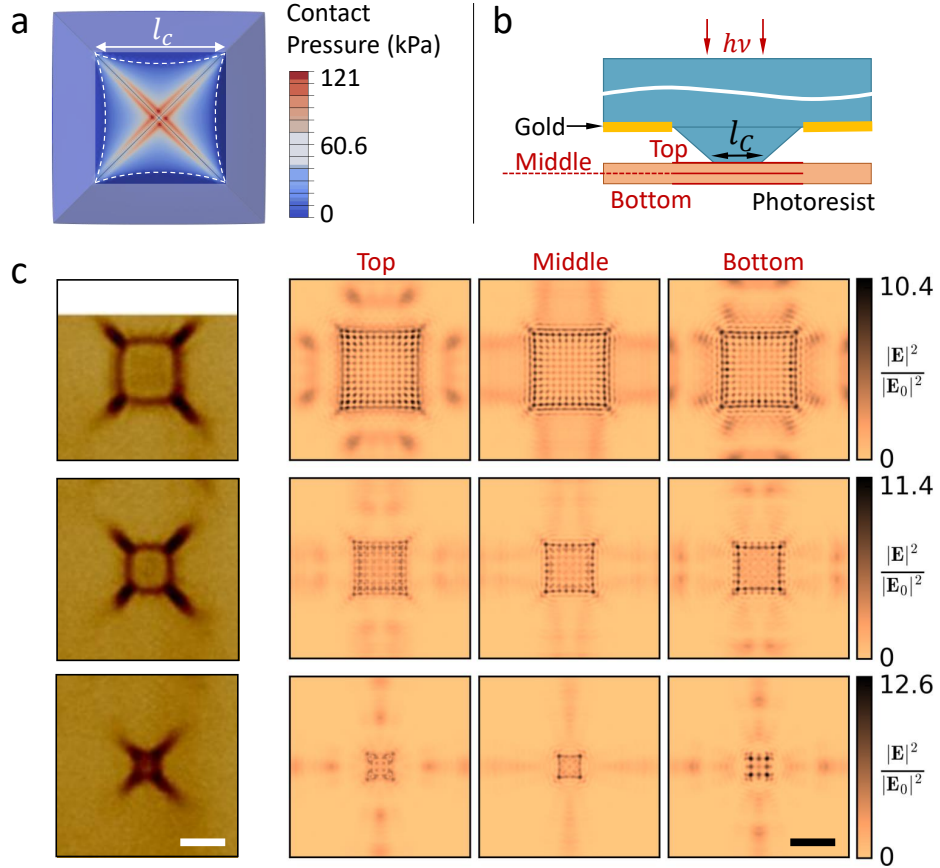


Figure 2.7. (a) The shape of the contact surface determined by the contact pressure.  $\tilde{d} = 0.8$ ,  $L = 8 \mu\text{m}$ ,  $G = 1.0 \text{ MPa}$ . (b) Lateral view of the FDTD simulation layout to model the patterning process of the apertureless BPL technique. The annotated red lines in the photoresist layer represent the three two-dimensional monitors to record the light intensity. (c) Left: the experimental photoresist patterns generated by the apertureless BPL technique. Copyright Wiley-VCH Verlag GmbH & Co. KGaA. Reproduced with permission from Ref. [6]. Feature sizes are  $3.40 \mu\text{m}$ ,  $2.58 \mu\text{m}$  and  $1.26 \mu\text{m}$  from top to bottom. Scale bar:  $2 \mu\text{m}$ . Right: near-field intensity profiles generated by FDTD simulations using the irregular shapes of the compressed pyramids. From top to bottom:  $l_c = 3.66 \mu\text{m}$ ,  $2.44 \mu\text{m}$ , and  $1.22 \mu\text{m}$  respectively. From left to right: the intensity profiles recorded by the top, middle and bottom monitors in the FDTD simulations. Scale bar:  $2 \mu\text{m}$ .

We superimpose the intensity profiles generated by two orthogonally polarized light sources to simulate an unpolarized incident light source for comparison with the experiments.

Simulations with the compressed pyramids show excellent agreement with the experimental results, as illustrated in Fig. 2.7c. The light intensities are mostly concentrated on the corners

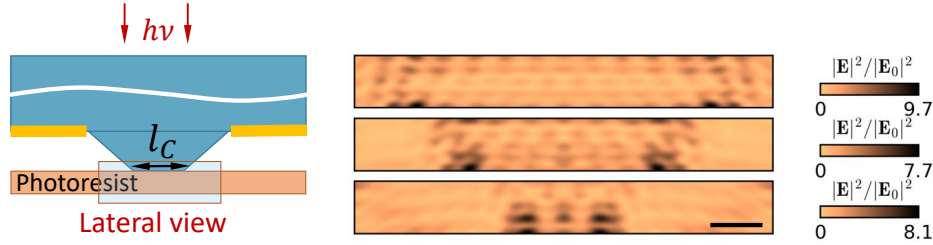


Figure 2.8. The lateral view of the near-field intensity profiles of the photoresist layer generated by FDTD simulations using the shapes of the compressed pyramids. The inspected plane is a symmetric plane of the pyramid parallel to one of its bottom edges. From top to bottom:  $l_c = 4.24 \mu\text{m}$ ,  $2.83 \mu\text{m}$ , and  $1.41 \mu\text{m}$  respectively. Scale bar:  $0.5 \mu\text{m}$ .

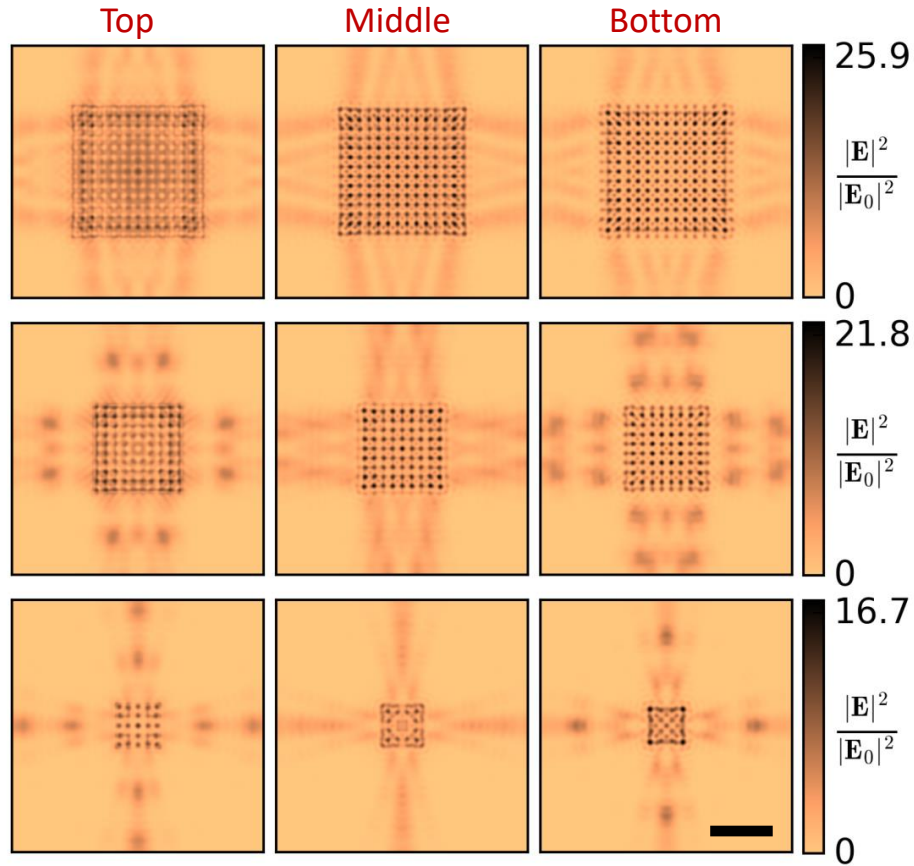


Figure 2.9. Near-field intensity profiles generated by FDTD simulations using the shapes of truncated pyramids. From top to bottom:  $l_c = 4.24 \mu\text{m}$ ,  $2.83 \mu\text{m}$ , and  $1.41 \mu\text{m}$  respectively. From left to right: the intensity profiles recorded by the top, middle and bottom monitors in the FDTD simulations. Scale bar:  $2 \mu\text{m}$ .

and edges of the contact surfaces, and relatively low intensities are found around the central area, therefore giving rise to the rounded square holes revealed in the experiments. Moreover, in consistency with the experimental findings, four “arms” of intensity are observed to extend from the corners of the square feature.

We note two major distinctions between the numerical and the experimental results: the presence of the coherent patterns, and the relatively weaker intensity of these “arms” observed in our simulations. These differences stem from the fact that Fig. 2.7c has not fully demonstrated the 3D intensity information recorded in the photoresist layer. The 2D photoresist patterns observed in experiments are essentially projected from the 3D intensity profile. As such, we further construct a lateral view of the 3D intensity profile of the photoresist layer as shown in Fig. 2.8. The inspected plane is a symmetric plane of the pyramid parallel to one of its bottom edges. It can be identified that the coherent patterns are divergent instead of parallel to the incident direction of the light. Therefore, the projected 2D photoresist patterns should possess a larger area than the real contact area, and exhibit less coherent features than those shown in Fig. 2.7c.

In contrast to the above agreement, simulations with a simple truncated pyramid fail to reproduce these unique characteristics of the experimental features, as evidenced by Fig. 2.9. Therefore, the distinct shape of the compressed pyramid plays a crucial role in developing these unusual BPL features, and may potentially be important in the applications of other cantilever-free SPL techniques using deformable pyramid pen arrays.

## 2.5. Conclusions

In summary, we numerically examine the compression of an elastomeric pyramid array that is widely employed as the pen structure in cantilever-free SPL, assuming a non-adhesive and frictionless contact with the rigid substrate. Our results reveal simple scaling laws for the width

of the contact surface with respect to the compression displacement and force. A reasonably good agreement is achieved between the existing experimental data and the scaling law Eq. 2.2 which is based on a more solid foundation than the previous empirical model. By reducing the inter-pyramid distances or the thickness of the elastomeric base, the width of the contact surface increases notably faster than the established scaling law at high compression displacement. We further inspect the unique contact surface shape that has yet been explicitly investigated in previous research. Using FDTD simulations, we successfully prove that the unusual features fabricated by the apertureless BPL techniques stem from the distinct shape of the compressed pyramid pen. As such, we believe that these results contribute to a better understanding of the deformation of the elastomeric pyramid pen array, which paves the way for a more precise control of the feature size and shape in the particular cantilever-free SPL techniques. Our findings may also be useful for designing novel functional devices where compressed elastomeric pyramid arrays play an important role, including highly sensitive pressure sensors, triboelectric nanogenerators, and beyond.

## CHAPTER 3

### **Emergent Perversions in the Buckling of Heterogeneous Elastic Strips**

Portions of this chapter were first published in *Proc. Natl. Acad. Sci.*: **113**, 7100-7105 (2016)

#### **3.1. Introduction**

Spontaneous symmetry breaking provides a unifying conceptual understanding of emergent ordered structures arising in various condensed matters [98]. In an elastic medium, which is one of the simplest organizations of matter, symmetry-breaking instabilities via buckling can lead to extraordinarily rich patterns and generate a wealth of shapes at multiple length scales that can be exploited in many scientific disciplines [99]. A prototype of elastic buckling is the Euler instability of an homogeneous elastic rod under uniaxial compression at the ends that finally breaks the rotational symmetry [100]. Introduction of extra structures in an elastic medium like mechanical heterogeneities [22], non-linearity of materials [99], geometric asymmetry [101] or intrinsic curvature [102] provides new dimensions that can produce even richer buckling modes, including helices and perversions [102, 103], wavy structures [104], regular networks of ridges [105], and even self-similar fractal patterns [99, 106]. Of these emergent symmetry broken structures, the helical shapes are of particular interest due to their ubiquitousness in nature and the strong connection with biological motifs, as noticed by Darwin in his 1875 book describing the curl of plant tendrils [107]. Remarkably, biological helical structures permeate over several length scales from the developed helical valve on opening seed pods [62], to the regular chiral structures in the flagella of bacteria [108], the spiral ramps of rough endoplasmic reticulum [109], and the chromosome of *E. coli* [110, 111].

The proliferation of perversions in an otherwise uniform helical structure can further break the helical symmetry (Fig. 3.1a shows a typical perversion in the helix) [102, 112, 22]. Here a perversion refers to a kink that connects two helices with opposite chiralities. Therefore, perversions belong to a large class of fundamental defects in systems with discrete symmetry which have the names of domain walls, solitons, or kinks depending on the particular context [98]. In contrast to domain walls in prototype spin systems, perversions embedded in both natural [102, 112] and artificial [22] helical systems have the unique freedom to wind around themselves in response to mechanical or geometric constraints. This salient feature of perversions accounts for several important observations, including the generation of more helices by a self-winding single perversion [102] and formation of the ripple patterns extensively found in animal guts and leaf edges through multiple perversions [29, 113]. Recent studies have further revealed that the perversion in the cucumber tendril, with its variable local stiffness, can unexpectedly overwind under tension rather than unwinding [23]. Previous theoretical studies using an ideal rod model with intrinsic curvature have qualitatively characterized the perversions [114, 115], yet cannot fully capture the postbuckling deformation or the interactions between perversions. These studies inspire us to have a closer look at the nature of perversions in helical structures, including perversions driven helical symmetry breaking and interactions between perversions.

The bistrip hyperelastic system provides an ideal model for studying the helical symmetry breaking and the physics of the resulting emergent perversions. The model hyperelastic system consists of two clamped strips with rectangular cross sections (see Fig. 3.1b); the shorter strip (strip A) is stretched and then attached to the longer one (strip B). With reduction of the strip length, we numerically observe the hierarchical buckling in the sequence of the development of helical shapes and then the spontaneous formation of perversions therein. Systematic simulations using different mesh sizes and initial perturbations show that the bistrip system can be easily trapped in

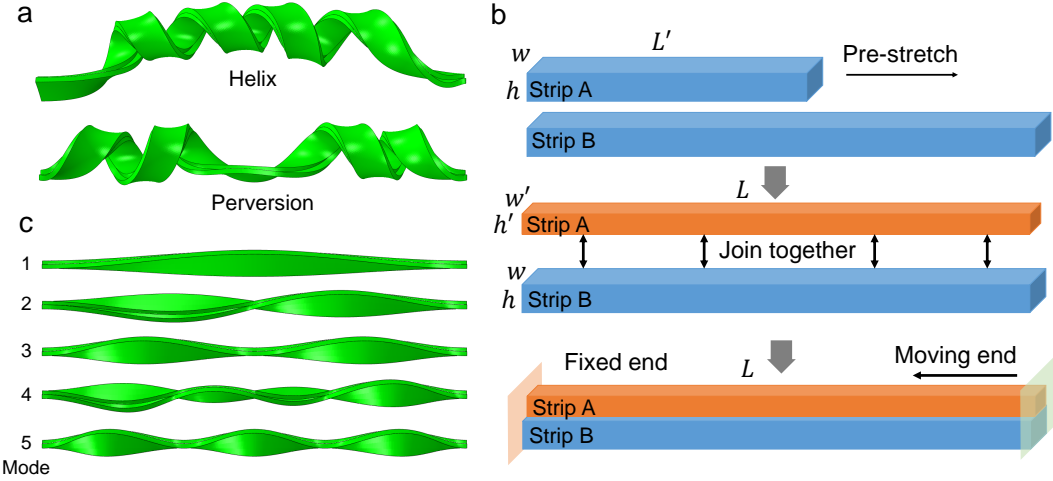


Figure 3.1. The illustration of the bistrip model. (a) shows a typical persion arising in an otherwise uniform helix (the upper figure) by controlling the boundary condition. (b) illustrates the bistrip model we used in the simulation. Strip A has the same cross section as strip B but shorter length in the initial state. Strip A is stretched and glued to strip B; both strips have the same length. One end of the bistrip system is fixed while the other end is allowed to translate but forbidden to rotate. (c) shows the first 5 buckling modes from eigenvalue buckling analysis.

metastable states; it is not guaranteed that the lowest energy conformation found by optimizing the simulation parameters are the true ground state. We therefore focus on the intrinsic features of perversions that are independent of specific shapes. Our study reveals the remarkable condensation of strain energy over perversions during their formation and the repulsive nature of the persion-persion interaction. These intrinsic properties of perversions may be exploited in the design of micro-muscles [116] and soft robotics [117].

### 3.2. Model

In the bistrip hyperelastic model, the strips have the same rectangular cross section but different lengths in their free states (see Fig. 3.1b). The upper shorter strip is firstly longitudinally stretched to the same length as the lower longer one, and then they are “glued” together such that both mutual slide and delamination are forbidden. In simulations, we carefully control the slow approach of the

anchored ends of the bistrrip whose orientations are fixed. The geometric and mechanical incompatibility of the strips is numerically observed to drive the out-of-plane deformations, including the helical shapes and perversions. The strips are made of the same material. Considering the involved large elastic deformations, we employ the compressible Neo-Hookean model which accounts for the volumetric variation compared with Eq. 1.10. Herein the stress and strain are related via the following form of the strain energy density  $U$  [45]:

$$(3.1) \quad U = \frac{G}{2} (\bar{I}_1 - 3) + \frac{K}{2} (J - 1)^2$$

where  $K$  characterize the resistance of the material to compression.  $J = \lambda_1 \lambda_2 \lambda_3$  representing the elastic volume ratio of the solid.  $\bar{I}_1 = J^{-2/3}(\lambda_1^2 + \lambda_2^2 + \lambda_3^2)$ . In our simulations, we employ a large  $K$  so that the material is treated as nearly incompressible, which is required for a quasi-static analysis introduced in the later texts. It seems that the appearance of perversions in the buckled helical system does not rely on the hyperelastic nature of materials; in soft elastic materials former finite element simulations have also revealed the existence of perversion structures [22].

In contrast with Euler's rod, the rectangular cross section in the pre-stretched bistrrip system is crucial for the appearance of nontrivial regular structures like the initially developed periodic helical shape and the scattered perversions therein with the reduction of the strip length. We first perform qualitative geometric analysis of helices and perversions in an originally flat strip whose ends are clamped without allowing any movement and rotation (see Fig. 3.2). A perversion can be produced by grabbing a point on the strip and rotating the strip (Fig. 3.2b). This generated perversion connects two helices with opposite chiralities. Further rotation from Fig. 3.2b to 3.2c leads to a reduction of the pitch and an increase of the number of helices in the paper strip. More perversions can be produced by grabbing other points and rotating in the region of helices. Therefore, the strip-like geometry does not impose a constraint on the allowed number of perversions. Multiple

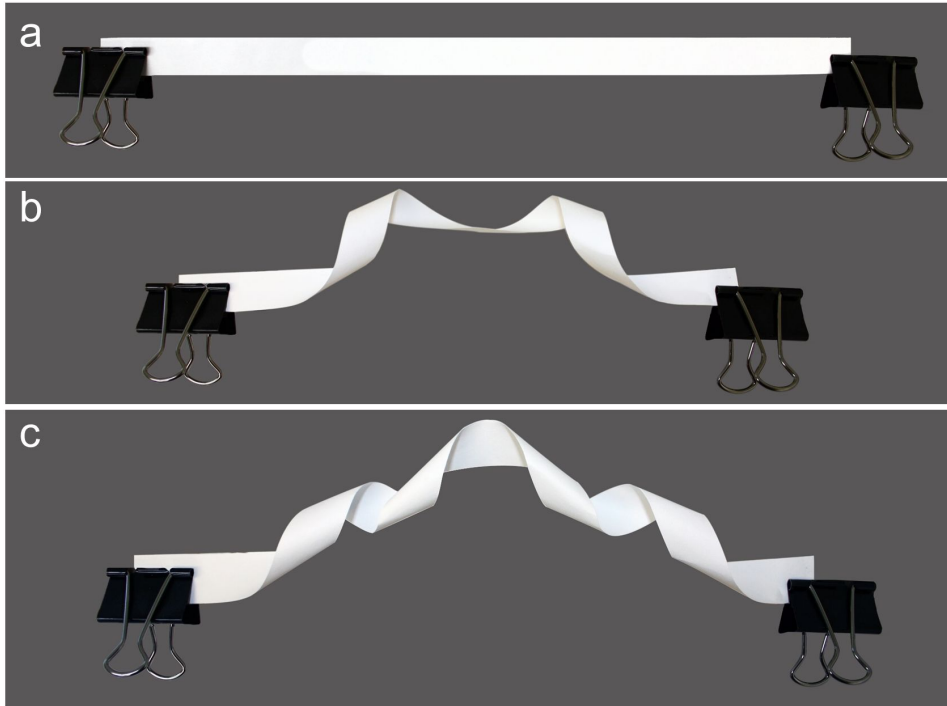


Figure 3.2. Paper experiments to illustrate that the number of perversions on the helical system is not geometrically constrained. By grabbing and rotating a point on the initially straight paper band (a), a perversion can be manually produced as shown in (b). Further rotation of the perversion in (c) can generate more helices.

perversions have been found in animal guts [29] and in the bistrip model [22]. The specific number of perversions in a helical strip is determined by several factors, such as the materials property and the external constraints [22, 118].

### 3.3. Implementation of the Finite Element Model

We resort to finite element analysis to track the shape evolution of the heterogeneous bistrip. The modeling parameters and boundary conditions are listed in Table 3.1 unless otherwise noted. As elaborated in 1.2.4, we first perform an eigenvalue buckling analysis to examine the stability of the bistrip under the constraints in Fig. 3.1b. The eigenvalue buckling analysis is performed using the Buckle Module in ABAQUS/Standard using the 3D linear reduced integration elements

Table 3.1. Parameters for finite element modeling of the postbuckling of a bistrip. The bistrip is assumed to be longitudinally oriented to  $z$ -axis. The notation of the geometrical parameters follows the same as Fig. 3.1.

<b>Geometry (cm)</b>		<b>Element</b>
$w$	Vary from 0.5 ~ 0.9	
$h$	0.3	C3D8R (Explicit) with enhanced hourglass control
$L$	30	
$L'$	$L/3.5$	
<b>Materials</b>		<b>Boundary conditions</b>
$G$	1.5 MPa	Fixed end of the bistrip ( $z = 0$ ), Encasted
$K$	40 MPa	Moving end of the bistrip ( $z = L$ ) $u_1 = u_2 = 0, u_3 < 0$ Connected surfaces of the bistrip Tie constraint applied ( <code>mdb.model[name].Tie</code> in Python script)

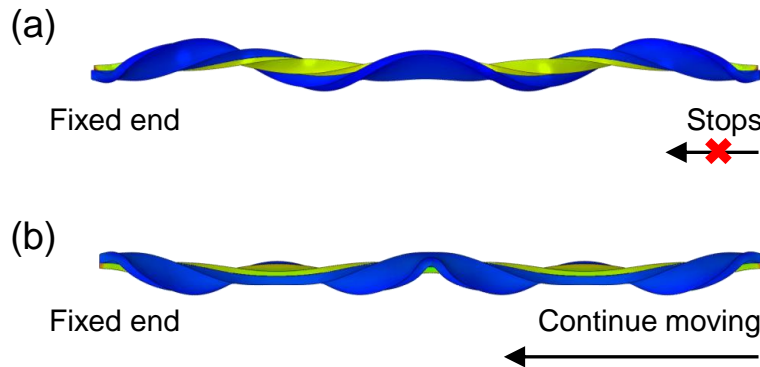


Figure 3.3. The effect of the displacement loading rate on the buckling shape of the bistrip. The original lengths of the bistrip in (a) and (b) are both 30.0 cm. (a) shows the buckling shape when the moving end stops at 23.3 cm. (b) shows the buckling shape at 23.3 cm while the end-to-end distance will continue shrinking to 9.0 cm.

(C3D8R). The eigenmodes of the bistrip include two types of perturbation shapes depending on the shape symmetry. Among the 5 modes listed in Fig. 3.1c, modes 1, 3 and 5 have mirror symmetry, while the others do not have apparent symmetry. Further simulations show that the postbuckling shapes of the bistrip do not appear dependent on the type of these eigenmodes.

The obtained eigenmodes are used as initial perturbations for the explicit dynamical finite element analysis performed in ABAQUS/Explicit using C3D8R elements (\*Imperfection in the .inp file). A Python code snippet for seeding imperfections to the geometry is shown below:

---

```

1 def GetKeywordPosition(model, prefix, maxTimes = 1):
2     keywordPos = 0
3     found = 0
4
5     if prefix == "":
6         return len(model.keywordBlock.sieBlocks) - 1
7
8     for block in model.keywordBlock.sieBlocks:
9         if block[0 : len(prefix)].lower() == prefix.lower():
10             found = found + 1
11             if found >= maxTimes:
12                 return keywordPos
13             keywordPos = keywordPos + 1
14
15     return 1
16
17 modelBistrip.keywordBlock.synchVersions()
18 keywordPos = GetKeywordPosition(modelBistrip, '*Boundary\n_M8, ENCASTRE')
19 modelBistrip.keywordBlock.insert(position = keywordPos,
20     text = '*Imperfection, file=Buckling_Analysis_Job, step=1\n1, 1e-3'
21 )
22 modBistrip.keywordBlock.synchVersions()

```

---

The initial stress of the prestretched strip can be imported using `mdb.model[name].Stress` in Python script.

In our simulations, the quasi-static equilibrium is enforced by carefully controlling the displacement loading rate of the moving end such that the kinetic energy of the system (ALLKE in the history output of ABAQUS) is negligible compared with strain energy (ALLSE in the history output of ABAQUS). A smoothing amplitude (`mdb.model[name].SmoothStepAmplitude`) is applied to the displacement loading for stabilizing the early response of the bistrip. The shape evolution of the bistrip system will be perturbed by this displacement loading rate, so changing the total loading time and distance can result in different buckling states of the bistrip even at the same end-to-end distance. For instance, both the bistrip shapes shown in Fig. 3.3a and 3.3b are obtained by reducing

the end-to-end distance from 30 cm to 23.3 cm. However, the moving end in Fig. 3.3a will stop exactly at 23.3 cm, while in Fig. 3.3b the end will continue moving until the end-to-end distance reduces to 9.0 cm. Consequently, different numbers of perversions emerge in Fig. 3.3a and 3.3b.

A careful mesh refinement study is performed to determine the best mesh size and fineness for the simulations, meanwhile ensuring that the total strain energy is converged. However, our results also indicate that the bistrip system can reach multiple metastable states by varying the mesh densities. These states have very close strain energy but different numbers of perversions. Since we are only concerned with the intrinsic properties of perversions, the presence of these metastable states does not influence our major conclusions.

### 3.4. Results and Discussion

In the simulations, the ends of the bistrip are carefully controlled to approach each other without allowing any rotation. This constraint ensures that the helices formed near the ends have opposite chiralities and guarantees the appearance of a perversion. Figure 3.4a demonstrates the growing of the initially slight out-of-plane deformation and the subsequent development of the single perversion in the helical state (For convenience of visualization, the end-to-end distances of the buckled bistrip are normalized in Fig. 3.4a; the buckling process with unnormalized end-to-end distances is shown in Fig. 3.5). The emergent perversion is located at the center of the strip, breaking the helical symmetry while preserving the mirror symmetry. The perversion is observed to wind around itself to generate more helices and meanwhile suppressing its own size. It has been observed that climbing tendrils also conform to the same winding scheme while growing longer [102]. In our case, the winding perversion plays the opposite role; it winds to reduce the pitch of helices in response to the reduction of the end-to-end distance of the bistrip.

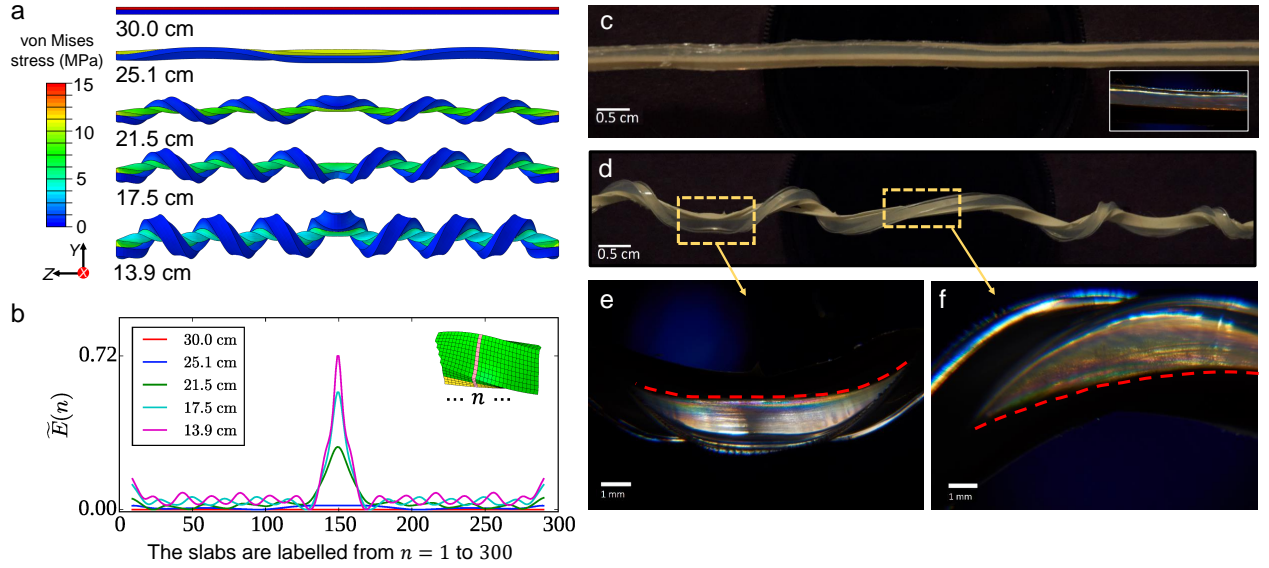


Figure 3.4. The energy condensation in the perversion of the bistrip system. (a) The formation and evolution of one perversion with the reduction of the strip length  $L$ ,  $w = 5 \text{ mm}$ ,  $h = 3 \text{ mm}$ ,  $L = 30 \text{ cm}$  and  $L' = L/3.5$  following the notation labeled in Figure 3.1b. The stress state of the bistrip is characterized by the distribution of the scalar von Mises stress which is originally proposed to analyze the yielding of materials [7]. (b) The scaled strain energy profile of the strips in (a).  $\tilde{E}(n) = E(n) / \min_{\{n\}}\{E(n)\} - 1$ , where  $n$  labels the slab of elements as shown in the inset, and  $E(n)$  is the total strain energy of all these elements in the  $n$ -th slab. (c-f) The designed bistrip system made of polyethylene and pre-stretched rubber strip to confirm the numerically observed energy condensation over the perversions. (c) and (d) show the shape of the bistrip before and after buckling. The inset in (c) shows the featureless birefringence pattern of the initial bistrip. The dashed red lines in (e) and (f) indicate the interface of the two strips. The different birefringence patterns in the perversion (e) and the helical (f) regions reflect the distinct strain energy distributions.

Simulations show that as the perversion is winding, the strain energy is concentrating. Figure 3.4b shows the energy distribution along the strip with the conformations in Fig. 3.4b. The energy is obtained by dividing the bistrip into  $n$  slabs and summing the strain energy across the cross sectional area of the slab. This quantity is then re-scaled to capture the relative energy changes in the perversions and in the helices. The energy condensation in the perversion region is clearly seen in Fig. 3.4b. The winding of the perversion provides the specific mechanism to focus energy locally in the perversion region. The amount of energy condensation will eventually saturate

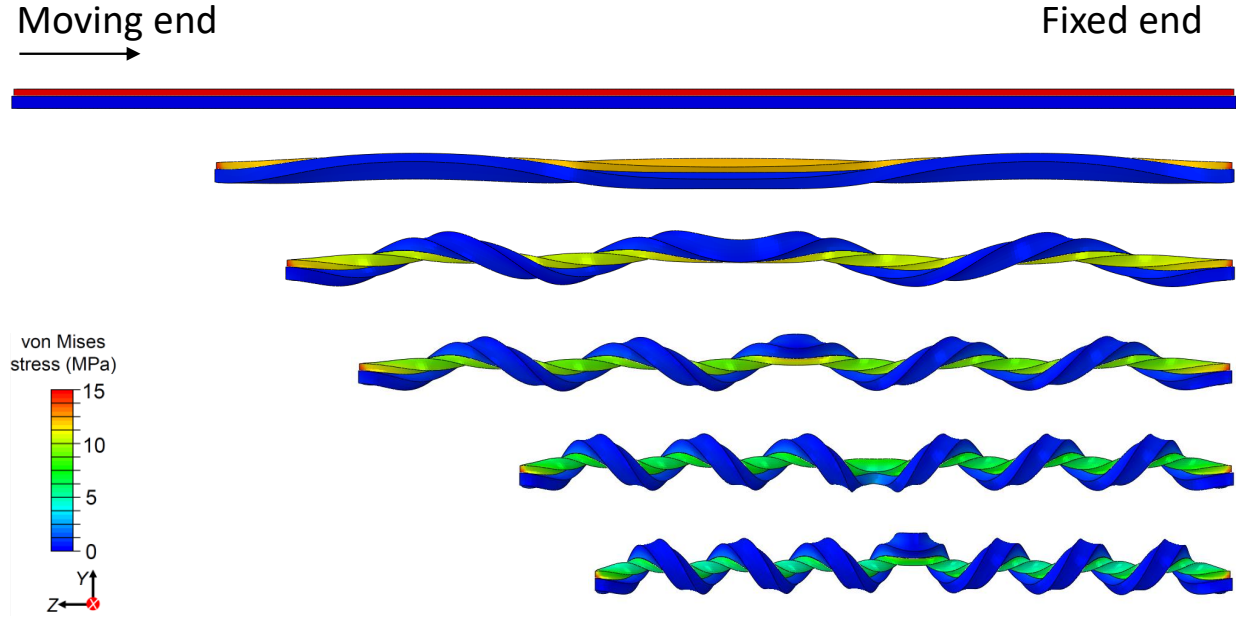


Figure 3.5. The buckling process of the bistrip in Fig. 3.4a without normalizing the end-to-end distances.

if the two ends of the bistrip are sufficiently close, since the perversion and helices under high compression will have contact with each other, and the whole structure may collapse at the position of the perversion. The spontaneous focusing of energy is a rich concept that permeates in fields as diverse as fluid mechanics, electrostatics, and elasticity of 2D materials [105]. Similar energy condensation phenomena occur on ridges in two-dimensional elastic medium where the stress is focused [105]. Here the revealed strain energy concentration is the demonstration of the energy focusing in three-dimensional elastic medium. The perversions as energy-absorbing singularity structures in helical systems may find applications in the design of micro-muscles [116] and soft robotics [117].

To check the reliability of numerical simulations and to exclude the possibility that the numerically observed energy focusing phenomenon is due to any hidden artifacts in simulations,

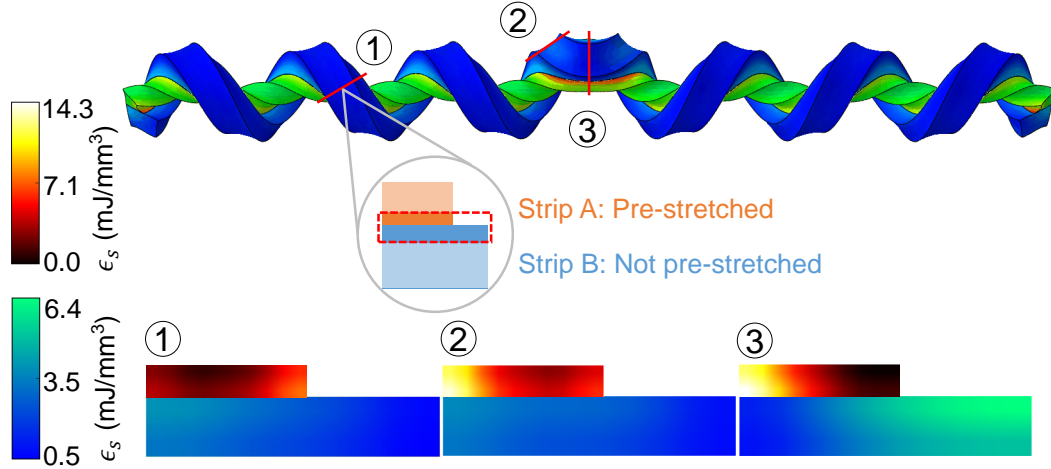


Figure 3.6. Analysis of the strain energy distribution over the cross section at different sites demonstrates distinct energy transfer modes in the perversion and helical regions. The images below show the distribution of strain energy density ( $\epsilon_s$ ) at sites 1, 2 and 3 in the above image, respectively. The cross sections of strip A and B share different scale bars for the different energy density ranges. The middle inset in the circle depicts the region over the cross section where we inspect.

we perform experiments to substantiate that the perversion structure is indeed energetically distinguishable from helices. The bistrip system is created by carefully casting melt polyethylene onto a pre-stretched rubber strip; the melt polyethylene becomes an initially stress-free elastic strip once it cooled. Figure 3.4c-f show the shapes of the bistrip with the controlled shrinking as in Fig. 3.4a. The differentials in the energy distribution over the strip is characterized by analyzing the birefringence of the elastic medium. No birefringence occurs in the initially straight strip (see the inset in Figure 3.4c). Birefringence patterns start to emerge at both the perversion (Fig. 3.4e) and the helical regions (Fig. 3.4f). Closer examinations show that in the perversion region the colored pattern only spreads around the edge of the pre-stretched strip, while at the helical region, the pattern distributes smoothly across the strip. To conclude, the distinct optical responses in the perversion and helical regions reflect the energetically distinguishable local states.

We resort to numerical simulations to perform quantitative analysis of the strain energy distribution over the strip, as the optical patterns in experiments can only reveal limited information. The

distinct birefringence patterns in Fig. 3.4e and 3.4f imply different modes of transferring strain energy over the cross section from the high energy pre-stretched strip to the other one in contact. Fig. 3.6 illustrates the energy distributions over the cross sections at typical sites at the bistrip. In the helical region labeled 1 in Fig. 3.6, the strain energy is evenly distributed along the interface. At the edge of the perversion labeled 2, the distribution of the energy over the cross section at the side of the strip B is similar to that in the helical region, while in the cross section of strip A the strain energy mostly concentrates at the lower-left corner attached to strip B. This trend is more pronounced over the cross section at the center of the perversion labeled 3; the strain energy in strip A is focused on the left side, while at the side of the strip B the strain energy is concentrated at the upper right corner where the strip B is highly squeezed. To conclude, the strain energy is transferred highly unevenly within the perversion from strip A to strip B compared with that in the helical region. In other words, in the perversion region the transferred energy distribution in strip B is obviously uneven. The obvious discontinuity in the strain energy distribution over the thickness of the bistrip system in Fig. 3.6 suggests that the basic features in the deformation of the bistrip system cannot be fully captured by a two-dimensional elastic model.

We study the case of multiple perversions on a single bistrip. These can be introduced by adjusting the geometric parameters of the strip and the loading rate. Figure 3.7a shows that the mirror symmetry of the system is broken while the three perversions are winding around themselves (see the last two conformations). Specifically, the broken mirror symmetry results from asynchronous rotation of the two perversions at the sides of the central perversion. As in the case of single perversion, all three perversions are observed to wind around themselves to shrink the strip length to fit the boundary condition and to reduce the energy of the system. The longitudinal energy distribution in Fig. 3.7b reveals the repulsive nature of the perversion-perversion interaction; the elevated energy profile between the perversions 1 and 2 in Fig. 3.7b is an indicator of repulsive

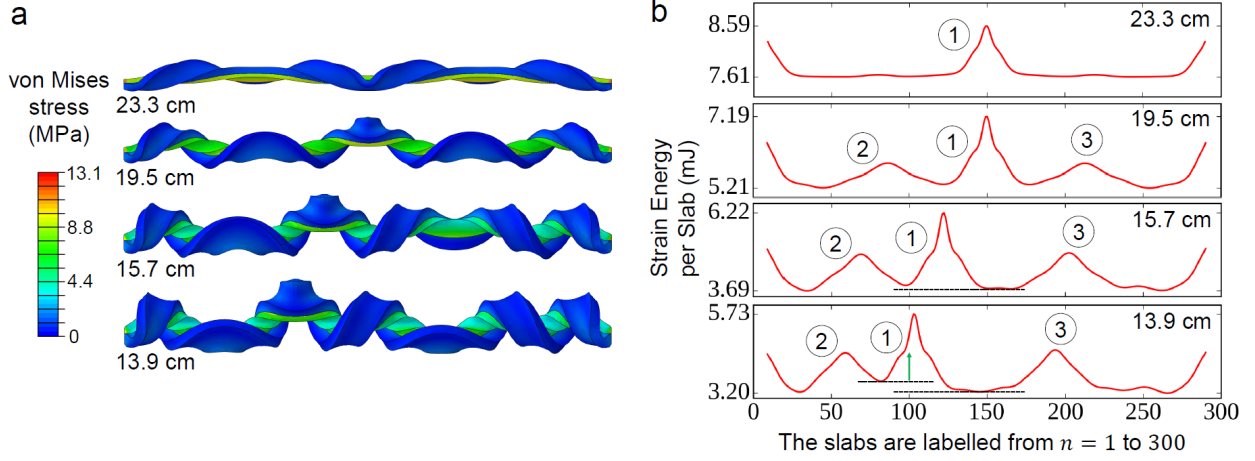


Figure 3.7. The formation and evolution of three perversions in a single bistrip. (a) and (b) show the conformations and the corresponding strain energy distribution. (a) shows that the symmetric bucklings of the perversions are broken by the winding of the rightmost perversion where the strip length is reduced by 35%. In (b), the energy peaks labeled as 1, 2 and 3 correspond to the perversions formed in the buckling. The green arrow in the last figure indicates energy elevation and therefore repulsion between perversions. The geometric parameters of the strips are:  $w = 9$  mm,  $h = 3$  mm,  $L = 30$  cm and  $L' = L/3.5$  following the notation labeled in Fig. 3.1.

interaction. Although the exact energy-distance relation is difficult to define in this system, the repulsion is expected to be short-ranged since we can only observe the energy elevation when the perversions are closer enough with each other. The shape evolution under quasi-static loading demonstrates the repulsion of perversions: the rightmost perversion rotates approximately 360° more than the other two while the end-to-end distance of the bistrip is reduced from 23.3 cm to 13.9 cm. This process pushes the central perversion to move towards the leftmost perversion. The energy focusing phenomenon is also observed in the multi-perversion systems. The condensation of the strain energy over all the perversions suggests that the energy focusing feature is an intrinsic property of the perversion structure. The geometric conformation of the central perversion is different from the other two perversions as shown in Fig. 3.7a. Consequently, the energy peak 1 in the energy profile of Fig. 3.7b corresponding to the central perversion is more focused and much higher than the other perversions.

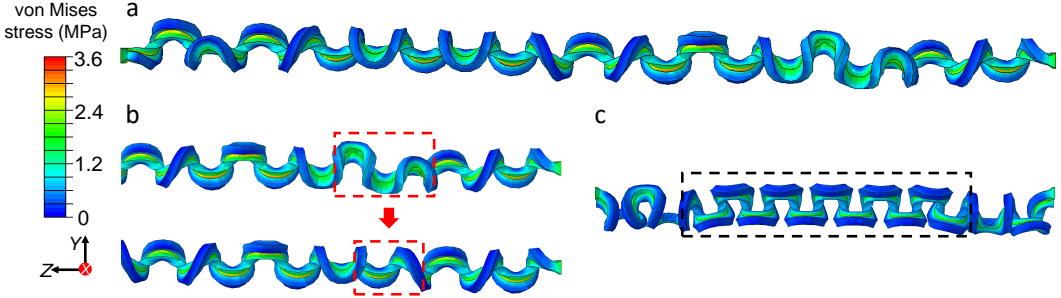


Figure 3.8. The formation and evolution of the perversions in a bistrip where one of the strips is pre-compressed. (a) shows that eighteen perversions emerges when two ends of the bistrip approaches. (b) In the right half of this bistrip, the two perversions in the red dashed boxes annihilate and coalesce into the nearby perversion. (c) shows the ordered perversion line structure (labeled in the black dashed box) eventually formed when the moving end is close enough with the other one. The geometric parameters of the strip are:  $w = 3$  mm,  $h = 3$  mm,  $L = 30$  cm and  $L' = 75$  cm following the notation labeled in Fig. 3.1.

We also explore a distinct routine to introduce the mechanical incompatibility over the bistrip system and observe new behaviors of emergent perversions not found in the pre-stretched bistrips described above. Specifically, we use a pre-compressed strip to replace the pre-stretched one in the bistrip. We find that further compression of the pre-compressed bistrip introduces perversions; around 20 perversions form when the bistrip length shrinks by only a tiny amount ( $\sim 1\%$ ) as can be seen in Fig. 3.8a. During the controlled shrinking of such a bistrip system, we numerically observe the merge of neighboring perversions and the development of an ordered helical section (see Fig. 3.8b). Remarkably, through this perversion annihilation mechanism, combined with the aforementioned winding behavior, perversions over a single bistrip can self-assemble to form some highly ordered linear structure, dubbed perversion lines as shown in Fig. 3.8c.

Perversions are the emergent defects in the helical pre-stressed bistrip. The spontaneous formation of the perversion line from individual perversions (as shown in Fig. 3.8c), which are defects themselves in an otherwise uniform helical structure, is strongly analogous to the self-organization of individual disclinations to form ordered compound defects like scars and pleats

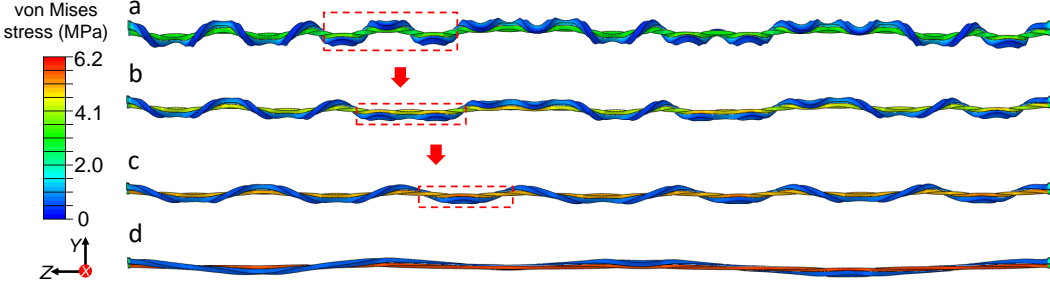


Figure 3.9. The evolution of the multiple perversions over a pre-compressed bistrip under stretching. The red dashed boxes in (a)-(c) is tracking a typical coalescence and annihilation of perversions. The total number of perversions consequently decreases as shown in (c)&(d). The length of the bistrip is becoming longer from (a) to (d). The geometric parameters of the strips are:  $w = 9$  mm,  $h = 3$  mm,  $L = 30$  cm and  $L' = L/3.5$  following the notation labeled in Fig. 3.1.

over curved crystals [119, 120, 121]. Note that the coalescence of perversions is not observed when their separation exceeds about two helical periods in the surveys of typical bistrip systems. In contrast, by uniformly stretching the pre-compressed bistrip, we numerically observe a series of dynamical events: the initial reduction of the amplitude of the out-of-plane deformation patterns (see Fig. 3.9a-b), the coalescence and annihilation of neighboring perversions (see Fig. 3.9a-c), and the reduction of the number of resulting helical periods (see Fig. 3.9d). Obviously, external stretching significantly facilitates the unknotting of perversions. To conclude, the examination of the pre-compressed bistrip system reveals new physics of perversions not found in the pre-stretched bistrips, including the coalescence of neighboring perversions that is crucial for the formation of ordered perversion lines.

We further investigate the essential material features that are crucial for producing the helical and perversion structures to break the symmetry. It is obvious that the pre-stretching in one of the strips in the bistrip system provides the driving force for the deformation of the entire system due to the elastic instability. Further simulations show that the geometries of the strips' cross sections can also critically control the resulting deformation patterns. In the preceding discussions, we focus on the bistrip system where the two strips in their relaxed states have an identical cross section profile.

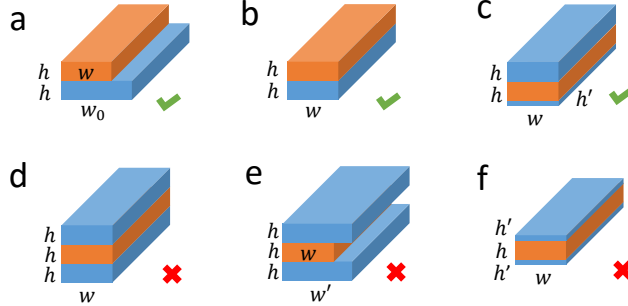


Figure 3.10. The cross section profiles of the strips inspected. The orange color of the strips indicate pre-stretching state; blue strips are stress-free in the initial state. As indicated by the ticks and crosses at the lower-right corner of each figure, (a)-(c) can produce helices and perversions, while (d)-(e) only deform to V-like shape. The geometric parameters of the strips are:  $w_0 = 9$  mm,  $w$  is the width after pre-stretching,  $w'$  can vary from  $5.4 \sim 6.3$  mm,  $h = 3$  mm,  $h' = 0.2$  mm.

The cross section of the pre-stretched strip shrinks as schematically shown in Fig. 3.10b due to the small volume compressibility of the material, leading to the geometric asymmetry. In addition, the pre-stretched strip breaks the up-down symmetry in the stress state of the bistrrip system. It is natural to ask if these pre-existent asymmetries are responsible for the out-of-plane deformation of the entire bistrrip and the emergence of the helical structure.

To address this question, we first prepare a bistrrip system as illustrated in Fig. 3.10b. In contrast to Fig. 3.10a, the upper strip, in its pre-stretched state, has the same cross section profile as the lower one. We numerically observe the formation of helical structure over such a bistrrip with the reduction of the end-to-end length. Therefore, the asymmetry of the cross section width in the bistrrip system can be excluded to be responsible for the formation of helical structures. Furthermore, we prepare tristrip systems that preserve the up-down symmetry in the initial state (see Fig. 3.10d and 3.10e). In both systems, the tristrips are numerically observed to buckle and form a V-like shape with the reduction of their lengths; no helical shapes are numerically observed. When the thickness of an outer strip in the tristrip system is reduced to be sufficiently small (see Fig. 3.10c; Fig. 3.10b can be regarded as the case where an outer strip is of zero thickness), helical structures appear again over such a tristrip system with the broken up-down symmetry.

These numerical results are still not sufficient to conclude that the asymmetry of the cross section thickness controls the formation of helical structures. It is well known that the bending of elastic plates or shells strongly depends on the thickness. To clarify whether it is the total thickness of the tristrip system or the differences between the two outer strips that determines the helical deformation, we simulate the system in Fig. 3.10f with the up-down symmetry but much thinner outer strips compared with the one in Fig. 3.10c. Similar to the case of Fig. 3.10d and 3.10e, no perversions are observed. The strips only buckle to a V-like shape with slight twisting around the center. Therefore, we can conclude that the up-down asymmetry in the strip thickness is more crucial to the emergence of the helices and perversions than the total thickness of the strip system.

### 3.5. Conclusions

This study uncovers several intrinsic properties of perversions that naturally occur to release stress in designed heterogeneous elastic bistrips. Besides playing a fundamental role as a generic domain wall that connects states of distinct symmetries, perversions exhibit richer physics in the three-dimensional elastic system. Specifically, we numerically observe the strain energy condensation over perversions during their formation, which is well confirmed in our designed experiments. We further identify distinct modes of energy transfer from a stretched strip to an initially unstretched one, and the repulsive nature of perversion-perversion interaction. Examination of the pre-compressed bistrip system reveals the coalescence of neighboring perversions which is crucial for their self-assembly into a highly ordered linear defect structure; it is in strong analogy with the formation of scars and pleats out of the elementary crystallographic defects in curved crystals. These intrinsic properties of perversions may be applicable to understanding and designing micro-muscles and soft robotics where perversions can be introduced in relevant helical structures to realize desired functions. Perversions as defects in the helical state may also share the common

attributes of defects in generic ordered phases, so there is much room for further exploration, notably regarding their possible coalescence, annihilation and intriguing interactions in response to various external constraints.

## CHAPTER 4

### Anisotropic Contraction of Fiber-Reinforced Hydrogels

#### 4.1. Introduction

Hydrogels, which can undergo dramatic volumetric changes in response to diverse stimuli such as temperature, pH, light and electric field [14, 15], have emerged in a broad range of applications in tissue engineering [17], soft robotics [122, 38], drug delivery [16], intelligent biosensors [20], and 3D printing [59]. In particular, great attention is being focused on developing hydrogels with anisotropic mechanical properties that can be utilized to mimic a variety of biological tissues with anisotropic morphologies, including cornea [33], skins [30], striated muscles[34, 123] and articular cartilages [35, 124]. Anisotropic hydrogels are also exploited for the fabrication of soft robotic actuators to trigger unidirectional motion [63]; in 3D printing, the anisotropic swelling of the hydrogel-based ink is critical to transform 2D patterns into the desired 3D shapes [59]. Thus designing hydrogels with ordered microstructures that impart controllable anisotropic mechanical properties is of both theoretical and experimental interest.

Previous research shows the diverse morphologies of the underlying microstructures that endow the isotropic hydrogels with anisotropic mechanical behaviors. For example, carbon nanotubes have been aligned in an otherwise isotropic hydrogel matrix using dielectrophoresis to generate both mechanical and electrical anisotropy [125]. Charged titania nanosheets can be cofacially oriented as layered structures which resist the hydrogels to shrink along the orthogonal direction to the sheets [63]. More types of morphologies including lamellar [31], porous [32] and liquid crystalline structures [126] are also reported in previous studies. In particular, hydrogels with

fibrous microstructures have been extensively explored and commonly adopted in biomimetics to simulate many soft tissues [30, 123, 127, 35, 128]. More importantly, remarkable anisotropic swelling and contraction of fiber-reinforced hydrogels have been reported in recent studies. Chin, *et al.* have fabricated the thermo-responsive tubular polymer hydrogel from a scaffold consisting of aligned self-assembled peptide amphiphile (PA) nanofibers; with specified temperature changes, the contraction strain perpendicular to the PA nanofibers is observed to be  $\sim 100\%$  higher than that along the PA nanofibers [73]. Similar anisotropy is also found in the swelling of the 3D printing ink based on hydrogels filled with aligned cellulose fibrils [59].

The anisotropic swelling and contraction of fiber-reinforced hydrogels stem from the directional constraints enforced by the oriented fibers. In the homogenization-based constitutive models for anisotropic hydrogels [129], these constraints are incorporated as an energetic contribution with extra parameters defined to characterize the strength of the fiber reinforcement. Previous studies following this paradigm have investigated the anisotropic swelling of fiber-reinforced hydrogels in various geometries such as thin sheets [67] and cylindrical tubes [68]. However, fiber properties, such as their dimensions and distributions, are not available in these phenomenological models; such morphological information is necessary for experiments to fabricate hydrogels with desired anisotropy. In fact, it still remains poorly understood how to maximize the swelling and contraction anisotropy of hydrogels by tuning the underlying microstructures.

In this contribution, we aim to achieve an in-depth understanding of the mechanisms maximizing the anisotropic contraction of fiber-reinforced hydrogels. Based on the Flory-Rehner theory, we firstly inspect the contraction anisotropy of a uniaxially constrained hydrogel, a simplified model which retains the directional constraint of the fibers. An upper bound of the contraction anisotropy determined by the prescribed isotropic contraction ratio is discovered when the hydrogel is initially strain-free. We further investigate potential improvements of this upper bound by applying prestrains

to the hydrogel. Our study reveals a remarkable enhancement of the contraction anisotropy when the uniaxially constrained hydrogel is prestretched along the constrained direction.

To examine the anisotropic contraction under the impact of the finite dimensions of fibers, we perform finite element simulations with periodic boundary conditions incorporated. By releasing the longitudinal restrictions of the fibers, maximum contraction anisotropies are identified when varying the transverse fiber-fiber distance. More approaches to improve the maximum anisotropy are noticed and explained, such as reducing the longitudinal fiber-fiber distance and increasing the fiber length. Our study provides new perspectives to control the anisotropic contraction of fiber-reinforced hydrogels, thus suggesting potential utilizations in designing novel anisotropic hydrogels for soft robotics, tissue engineering and biomedical devices.

#### 4.2. Flory-Rehner theory

We describe the deformation and contraction of the hydrogel using the classical Flory-Rehner theory [130]. The free energy of a hydrogel consists of the elastic energy of the polymer network and the polymer-solvent mixing energy:

$$(4.1) \quad F = F_{\text{el}} + F_{\text{mix}}$$

Various forms of elastic energy have been proposed in former research to characterize the reduction of entropy by stretching the cross-linked polymer network [44, 131, 132]. In the present work,  $F_{\text{el}}$  follows the simplest form derived by Wall and Flory based on the Gaussian statistics [44]:

$$(4.2) \quad F_{\text{el}}(\lambda_1, \lambda_2, \lambda_3, T) = \frac{1}{2} NkT [\lambda_1^2 + \lambda_2^2 + \lambda_3^2 - 3 - \ln(\lambda_1 \lambda_2 \lambda_3)]$$

where  $N$  is the number of polymer chain segments between the crosslinking junctions and  $\lambda_1, \lambda_2, \lambda_3$  are the stretch ratios along the three principal axes in reference to the molten state of the polymer.

The polymer-solvent mixing energy  $F_{\text{mix}}$  is given by the Flory-Huggins theory [9]

$$(4.3) \quad F_{\text{mix}}(\phi, T) = kT \frac{V}{\nu} [(1 - \phi) \ln(1 - \phi) + \chi \phi(1 - \phi)]$$

where  $V$  is the volume of the whole hydrogel,  $\nu$  is the volume of each solvent molecule,  $\phi$  is the volume fraction of the monomers and  $\chi$  is the Flory-Huggins interaction parameter between polymer chains and the solvent molecules. Let  $V_m$  be the volume of the polymer chains in the molten state, the volume fraction of the monomers is defined as

$$(4.4) \quad \phi = \frac{V_m}{V} = (\lambda_1 \lambda_2 \lambda_3)^{-1}$$

Next, we apply the above material model to two simple cases, a free-swelling and a uniaxially constrained hydrogel, which will be employed to model the fiber-reinforced hydrogel in the subsequent discussions.

#### 4.2.1. Free-shrinking hydrogel

For an isotropic free-shrinking hydrogel,  $\lambda_1 = \lambda_2 = \lambda_3 = \phi^{-1/3}$ , thus the total free energy given by Eq. 4.1, 4.2 and 4.3 can be rewritten in terms of  $\phi$  and  $T$ :

$$(4.5) \quad \begin{aligned} F(\phi, T) &= \frac{1}{2} N k T \left( \frac{3}{\phi^{2/3}} - 3 + \ln \phi \right) \\ &\quad + k T \frac{V_m}{\nu} \left[ \left( \frac{1}{\phi} - 1 \right) \ln(1 - \phi) + \chi(1 - \phi) \right] \end{aligned}$$

When the free swelling gel is in equilibrium with the external solvent, its osmotic pressure  $\Pi$  must be zero, i.e.,

$$(4.6) \quad \Pi = - \left( \frac{\partial F}{\partial V} \right)_T = \frac{\phi^2}{V_m} \left( \frac{\partial F}{\partial \phi} \right)_T = 0$$

For simplicity we assume that  $\chi$  is independent of  $\phi$  and only varies in response to the external stimuli. Substituting Eq. 4.5 in 4.6, we obtain that

$$(4.7) \quad \chi = \frac{1}{2} \frac{N\nu}{V_m} \left( \frac{1}{\phi} - \frac{2}{\phi^{5/3}} \right) - \frac{1}{\phi^2} \ln(1 - \phi) - \frac{1}{\phi}$$

As a result, the volume fraction of the monomers  $\phi$  must follow Eq. 4.7 at the thermodynamic equilibrium, which drives the hydrogel to swell or shrink through the diffusion of the solvent molecules under external stimuli. It is noteworthy that  $\chi$  may depend on  $\phi$  in some polymer solutions [133], which will be separately addressed later on in this paper; for now we just consider a  $\phi$ -independent  $\chi$ .

#### 4.2.2. Uniaxially constrained hydrogel

We proceed to study the contraction of a hydrogel subject to a uniaxial stress along the longitudinal direction. Without loss of generality, let  $\lambda_1 = \lambda_2 = \lambda_{\perp}$  be the transverse stretch ratio, and  $\lambda_3 = \lambda_{\parallel}$  is the longitudinal stretch ratio, hence  $\phi = (\lambda_{\perp}^2 \lambda_{\parallel})^{-1}$ . Following Eq. 4.1, 4.2 and 4.3, the free energy of a hydrogel under a uniaxial constraint is written as

$$(4.8) \quad F(\lambda, \lambda_c, T) = \frac{1}{2} NkT \left( \frac{2}{\phi \lambda_{\parallel}} + \lambda_{\parallel}^2 - 3 + \ln \phi \right) + kT \frac{V_m}{\nu} \left[ \left( \frac{1}{\phi} - 1 \right) \ln(1 - \phi) + \chi(1 - \phi) \right]$$

The principal stress  $\sigma_1$  and  $\sigma_2$  along the transverse directions should vanish when the hydrogel is at thermodynamic equilibrium:

$$(4.9) \quad \sigma_1 = \sigma_2 = \frac{1}{V_m \lambda_{\perp} \lambda_{\parallel}} \left( \frac{\partial F}{\partial \lambda_{\perp}} \right)_{T, \lambda_{\parallel}} = 0$$

Therefore, the Flory-Huggins parameter  $\chi$  and the volume fraction  $\phi$  for a uniaxially constrained hydrogel must satisfy Eq. 4.8 and 4.9 at equilibrium, which delivers

$$(4.10) \quad \chi = \frac{1}{2} \frac{N\nu}{V_m} \left( \frac{1}{\phi} - \frac{2}{\phi^2 \lambda_{||}} \right) - \frac{1}{\phi^2} \ln(1 - \phi) - \frac{1}{\phi}$$

The principal stress in the longitudinal direction  $\sigma_3$  is written as

$$(4.11) \quad \sigma_3 = \frac{1}{V_m \lambda_{||}^2} \left( \frac{\partial F}{\partial \lambda_{||}} \right)_{T, \lambda_{||}} = \frac{NkT}{V_m} \frac{\phi}{\lambda_{||}} \left( \frac{1}{\phi_c} - \frac{1}{\phi} \right)$$

where  $\phi_c = \lambda_{||}^{-3}$  and Eq. 4.10 is used to eliminate  $\chi$ . Eq. 4.11 suggests that give a fixed value of  $\lambda_{||}$ ,  $\sigma_3 > 0$  when  $\phi > \phi_c$ , hence the hydrogel is in stretching state along the longitudinal direction. On the contrary, if  $\phi < \phi_c$ ,  $\sigma_3 < 0$  such that the hydrogel is compressed under the constraint. At  $\phi = \phi_c$ ,  $\sigma_3 = 0$ , indicating that the hydrogel stays in a free swelling state because the longitudinal stress vanishes. Herein, we introduce the longitudinal strain  $\epsilon_{||}$  to describe the longitudinal deformation of the hydrogel; at a specified  $\chi$ ,  $\epsilon_{||}$  can be defined as:

$$(4.12) \quad \epsilon_{||} = \frac{\lambda_{||} - \lambda}{\lambda}$$

where  $\lambda$  is the equilibrated stretch ratio of a free-shrinking hydrogel at the same  $\chi$ .

### 4.3. Anisotropic contraction of a uniaxially constrained hydrogel

Based on the Flory-Rehner theory, we formulate a simplified model of fiber-reinforced hydrogels to explore the potential mechanisms enhancing the contraction anisotropy. Specifically, the anisotropic contraction of the aforementioned uniaxially constrained hydrogel is investigated in the absence of the oriented fibers (see Fig. 4.1a): in the longitudinal direction (parallel to the fiber direction) the contraction of the hydrogel is restricted, whereas in the transverse directions the hydrogel can shrink freely. Herein we essentially preserve the directional constraint from the fibers

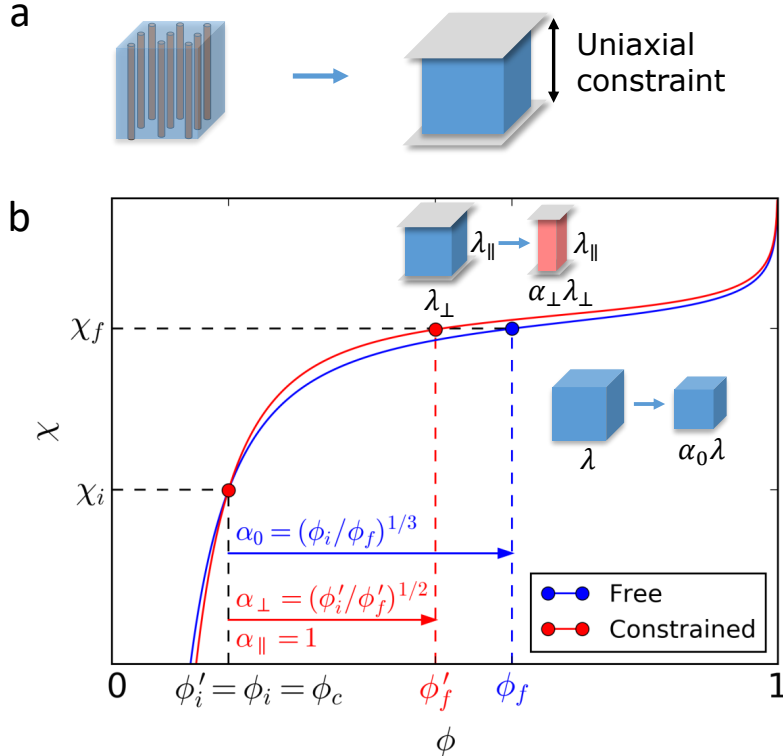


Figure 4.1. Schematic plots of hydrogel contractions in response to increasing  $\chi$ . (a) A fiber-reinforced hydrogel is simplified as a uniform hydrogel subject to a uniaxial constraint along the fiber direction. (b) The contraction of a free-shrinking hydrogel (blue curve) and a uniaxially constrained hydrogel (red curve) with a fixed  $\lambda_{\parallel}$  ( $\alpha_{\parallel} = 1$ ). Both of the contractions start at the intersection point  $\phi_i = \phi'_i = \phi_c = \lambda_{\parallel}^{-3}$ . The arrows represent the direction of contractions along the  $\phi$  axis.

which apparently plays a critical role in the anisotropic contraction, and meanwhile eliminate the complex local deformations introduced by the fibers for simplicity.

In experiments, the anisotropic contraction of a hydrogel with non-trivial microstructures is often investigated and evaluated by comparing with the isotropic contraction of an unmodified hydrogel [73, 59, 63]. Following this paradigm, we firstly imagine that a free hydrogel undergoes an isotropic contraction in response to an external stimulus which increases its Flory-Huggins parameter from  $\chi_i$  to  $\chi_f$ , as depicted in Fig.4.1b. The stretch ratio of the hydrogel along each dimension is reduced from  $\lambda_i$  to  $\lambda_f$ , and correspondingly the volume fractions of the monomers

increases from  $\phi_i$  to  $\phi_f$  according to Eq. 4.4. The contraction ratio along each principal axis, denoted by  $\alpha_0$ , can be defined as

$$(4.13) \quad \alpha_0 = \frac{\lambda_f}{\lambda_i} = \left( \frac{\phi_i}{\phi_f} \right)^{1/3}$$

In the following analysis, we assume that  $\alpha_0$  is prescribed by the external stimulus, allowing us to use  $\alpha_0$  as a benchmark to analyze the anisotropic contraction of a uniaxially constrained hydrogel.

For a hydrogel uniaxially constrained along the longitudinal direction, it shrinks anisotropically if its  $\chi$  increases from  $\chi_i$  to  $\chi_f$ . The contraction ratio along the longitudinal and transverse directions are denoted by  $\alpha_{\parallel}$  and  $\alpha_{\perp}$  respectively. We can likewise define the contraction ratio  $\alpha_{\parallel}$  and  $\alpha_{\perp}$  as

$$(4.14) \quad \alpha_{\parallel} = \frac{\lambda_{\parallel,f}}{\lambda_{\parallel,i}} \quad \alpha_{\perp} = \frac{\lambda_{\perp,f}}{\lambda_{\perp,i}}$$

where  $\lambda_{\parallel}$  is the longitudinal stretch ratio and  $\lambda_{\perp}$  is the transverse stretch ratio. The subscripts  $i$  and  $f$  represent the initial and shrunken state respectively. We define the contraction anisotropy  $A$  as

$$(4.15) \quad A = \frac{\alpha_{\parallel}}{\alpha_{\perp}} = \frac{\lambda_{\parallel,f}}{\lambda_{\parallel,i}} \frac{\lambda_{\perp,i}}{\lambda_{\perp,f}}$$

Therefore, the larger  $A$ , the stronger the contraction anisotropy of the hydrogel.

For common hydrogels with positive Poisson's ratios, the longitudinal stretch ratio must decrease during contraction even though it is restricted externally, which indicates  $\Delta\lambda_{\parallel} = \lambda_{\parallel,f} - \lambda_{\parallel,i} \leq 0$ . Let  $\phi'_i$  and  $\phi'_f$  be the volume fractions of the monomers before and after the contraction; the contraction anisotropy  $A$  is bounded by the following inequality:

$$(4.16) \quad A = \frac{\lambda_{\parallel,f}}{\lambda_{\parallel,i}} \frac{\lambda_{\perp,i}}{\lambda_{\perp,f}} = \left( \frac{\phi'_f}{\phi'_i} \right)^{1/2} \left( \frac{\lambda_{\parallel,f}}{\lambda_{\parallel,i}} \right)^{3/2} \leq \left( \frac{\phi'_f}{\phi'_i} \right)^{1/2}$$

Eq.4.16 takes equality when  $\alpha_{\parallel} = 1$  and  $\alpha_{\perp} = (\phi'_i/\phi'_f)^{1/2}$ , indicating that the anisotropy of the contraction is maximized when the hydrogel is not allowed to shrink along the longitudinal direction (i.e.,  $\lambda_{\parallel}$  is constant). Using Eq. 4.7 and Eq. 4.10 with a fixed  $\lambda_{\parallel}$ , we can compare  $\phi'_f/\phi'_i$  with  $\phi_f/\phi_i$  given a specified increment of  $\chi$ , and therefore explore the possibilities to reduce the upper bound of  $A$ .

#### 4.3.1. Stress-free initial state

If the uniaxially constrained hydrogel starts to shrink from the stress-free state ( $\phi'_i = \phi_i = \phi_c$ ,  $\epsilon_{\parallel} = 0$ ), we find that the maximum contraction anisotropy ( $A_{\max}$ ) must be smaller than  $\alpha_0^{-3/2}$ . As illustrated in Fig. 4.1b, if  $\phi'_i = \phi_i = \phi_c$ ,  $\phi'_f < \phi_f$  for any  $\chi_f > \chi_i$ , i.e., the volumetric change of the uniaxially constrained hydrogel is always smaller than that of a free hydrogel, thus

$$(4.17) \quad A_{\max} = \left( \frac{\phi'_f}{\phi'_i} \right)^{1/2} < \left( \frac{\phi_f}{\phi_i} \right)^{1/2} = \alpha_0^{-3/2}$$

Eq. 4.17 can also be analytically proved by comparing Eq. 4.7 with 4.10. We firstly show that the  $\chi$  value of the uniaxially constrained hydrogel is always larger than that of the free hydrogel at the same  $\phi$  when  $\phi > \phi_c$ . Let  $\chi$  and  $\chi'$  denote the Flory parameter for the free hydrogel and the uniaxially constrained hydrogel respectively;  $\chi$  and  $\chi'$  intersect at  $\phi_c$  as shown in Fig. 4.1b. According to Eq. 4.7 and 4.10,  $\chi$  and  $\chi'$  differ by

$$(4.18) \quad \chi - \chi' = \frac{N\nu}{V_m\phi^2} \left( \frac{1}{\lambda_{\parallel}} - \phi^{1/3} \right)$$

which suggests that  $\chi < \chi'$  for arbitrary  $\phi > \phi_c$  and vice versa. If the initial state of the contraction has no prestrain, i.e.,  $\phi'_i = \phi_i = \phi_c$ ,  $\phi'_f$  and  $\phi_f$  must be larger than  $\phi_c$ . Thus

$$(4.19) \quad \chi'(\phi_f) > \chi(\phi_f) = \chi'(\phi'_f).$$

Since  $\chi'$  is monotonic as a function of  $\phi$ , we obtain  $\phi_f > \phi'_f$  which leads to  $(\phi'_f/\phi'_i)^{1/2} < (\phi_f/\phi_i)^{1/2} = \alpha_0^{-3/2}$ . Consequently,  $A_{\max}$  is upper bounded by  $\alpha_0^{-3/2}$  if there is no prestrain involved in the initial state of the shrinking process.

Contraction experiments of fiber-reinforced hydrogels satisfying Eq. 4.17 have been reported in previous research. For example, in Chin *et al.*'s work [73], the tubular polymer gel shrunk isotropically to 77% of its original size when the temperature ramped up from room temperature to  $\sim 70^\circ\text{C}$ , i.e.,  $\alpha_0 = 0.77$ . If the gel was reinforced with circumferentially aligned peptide amphiphile nanofibers, the height and diameter of the tube shrank respectively to 62% and 80% of the original dimensions upon the same variation of temperature; the contraction anisotropy  $A = 1.29$  is smaller than  $\alpha_0^{-3/2} \approx 1.48$  within the margin of error ( $|\Delta A| \approx 0.1$ ), which agrees with Eq. 4.17.

### 4.3.2. Prestrained initial state

If the uniaxially constrained hydrogel is prestrained before contraction ( $\phi_i, \phi'_i \neq \phi_c, \epsilon_{\parallel} \neq 0$ ), the upper bound suggested by Eq. 4.17 may not hold. As illustrated in Fig. 4.2a, for example, if  $\phi'_i > \phi_c$ ,  $\phi'_i$  and  $\phi_i$  at the same  $\chi_i$  no longer coincide with each other; it can be identified that at certain  $\chi_i$  and  $\chi_f$ ,  $\phi'_f/\phi'_i > \phi_f/\phi_i$  so that  $A_{\max} > \alpha_0^{-3/2}$ .

Indeed, our further analysis uncovers that  $A_{\max}$  can be significantly greater than  $\alpha_0^{-3/2}$  if the hydrogel is longitudinally prestretched before contraction. Specifically, for an arbitrary  $\phi_i$ , a prestrain within the range from  $-0.5$  to  $1.0$  is applied to the free-swelling hydrogel so that  $\phi'_i$  can be determined by equating Eq. 4.7 to Eq. 4.10 and meanwhile incorporating Eq. 4.12. By setting  $\alpha_0 = 0.8$ , we numerically calculate  $A_{\max}$  for different  $N\nu/V_m$ . Results (see Fig. 4.2b) clearly reveal that  $A_{\max}$  can be larger than  $\alpha_0^{-3/2} \approx 1.40$  only when  $\epsilon > 0$ . For example, for  $N\nu/V_m = 0.01$ ,  $A_{\max}$  can be as large as 1.54 when  $\epsilon_{\parallel} = 1.0$ . The value of  $A_{\max}$  becomes larger as a whole when  $\epsilon$  increases, and eventually converges to  $(\phi'_i)^{-1/2}$  when the hydrogel volume  $V$  approaches  $V_m$ . In

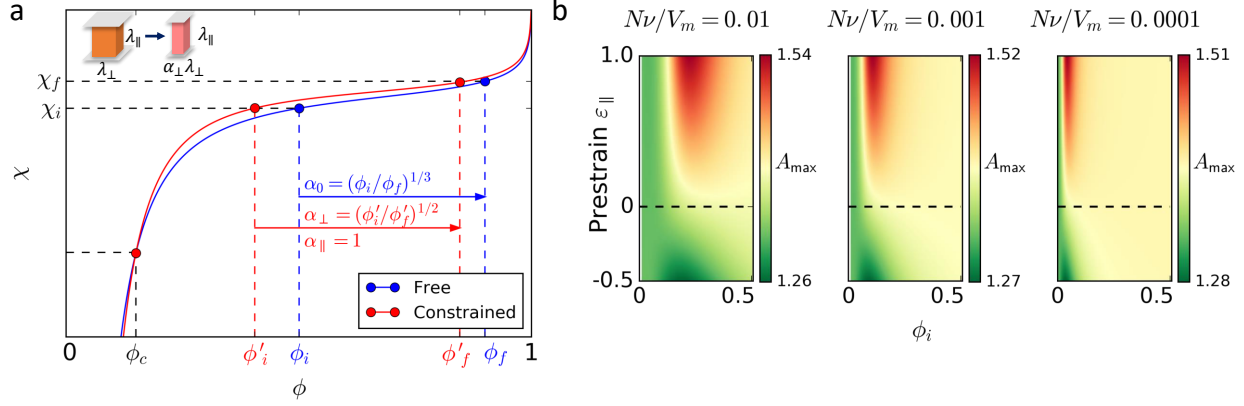


Figure 4.2. Contraction of uniaxially constrained hydrogels with prestrain  $\epsilon_{\parallel} \neq 0$ . (a) Schematic  $\chi \sim \phi$  plot of a uniaxially constrained hydrogel (red curve) undergoing a stronger volumetric contraction ( $\phi'_f/\phi'_i > \phi_f/\phi_i$ ) than a free-shrinking hydrogel (blue curve) with  $\epsilon_{\parallel} > 0$ . The arrows represent the direction of the contractions along the  $\phi$  axis. (b) The upper bound of the contraction anisotropy ( $A_{\max}$ ) as a function of  $\phi_i$  and  $\epsilon_{\parallel}$  for different  $N\nu/V_m$ .  $\alpha_0 = 0.8$  in all subfigures. The longitudinally prestretched ( $\epsilon_{\parallel} > 0$ ) and precompressed ( $\epsilon_{\parallel} < 0$ ) states are separated by the dashed lines.  $\phi_i$  is limited within the range  $0 \sim 0.5$  because the final volume fractions  $\phi_f$  and  $\phi'_f$  must be less than 1 due to the specified  $\alpha_0$ .

addition, the distribution patterns of  $A_{\max}$  in Fig. 4.2b demonstrate a significant shift when  $N\nu/V_m$  reduces. Since  $N\nu/V_m$  is only associated with the elastic terms in Eq. 4.2, our observation implies that initially more swollen states are favored to produce stronger contraction anisotropy when the hydrogel is less rigid. In conclusion, the contraction anisotropy of a uniaxially constrained hydrogel can be substantially stronger if the hydrogel is longitudinally prestretched.

For a practical fiber-reinforced hydrogel, the prestretching condition may be potentially realized in several approaches. The simplest approach is to apply an external control to the hydrogel along the fiber direction. Prestretching may also be introduced if the fiber-reinforced hydrogel is already in the shrunken state before performing the contraction experiments. Additionally, incorporating the fibers into the hydrogel matrix may lead to intrinsic prestretching due to the interaction between the fibers and the polymer chains.

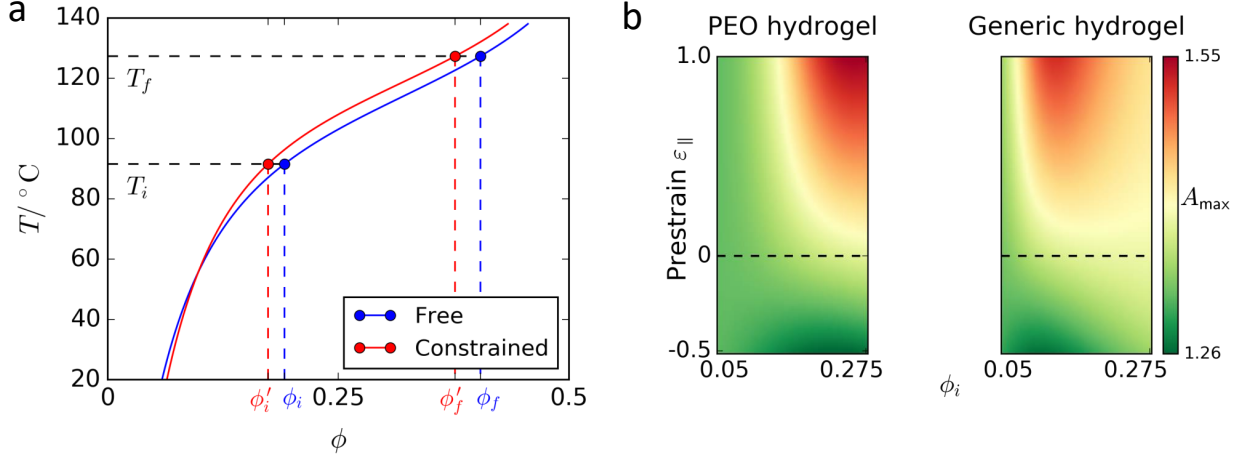


Figure 4.3. Contraction of PEO hydrogels upon increasing temperature. (a) The contraction of a free-shrinking (blue curve) and a uniaxially constrained (red curve) PEO hydrogel as the temperature increases from  $T_i$  to  $T_f$ . (b) The upper bound of the contraction anisotropy ( $A_{\max}$ ) as a function of  $\phi_i$  and  $\epsilon_{\parallel}$  for a PEO hydrogel (left) and a generic hydrogel with  $\phi$ -independent  $\chi$  (right).  $N\nu/V_m = 0.002$  and  $\alpha_0 = 0.8$  in all subfigures.

#### 4.3.3. $\phi$ -dependent $\chi$

If  $\chi$  varies as a function of  $\phi$ , an explicit dependence of  $\chi$  on both the stimulus intensity (denoted by  $T$ ) and  $\phi$  is required to analyze the contraction of hydrogels through the above approach. In previous discussions, we have assumed that  $\chi$  is independent of  $\phi$ , therefore the external stimulus and the deformation are naturally decoupled in Eq. 4.7 and 4.10, which allows us to investigate the contraction behaviors without knowing the specific form of  $\chi(T)$ . In contrast, if  $\chi$  also depends on  $\phi$ , we need to replace  $\chi$  with  $\bar{\chi}$  in Eq. 4.7 and 4.10:

$$(4.20) \quad \bar{\chi} = \chi - \phi \frac{\partial \chi}{\partial \phi}$$

With the knowledge of the function  $\chi(T, \phi)$ , the relation between  $T$  and  $\phi$  at equilibrium can be obtained and exploited to investigate the contraction behaviors.

To exemplify the above procedure for handling the  $\phi$ -dependent  $\chi$ , we analyze the contraction behaviors of a crosslinked poly(ethylene oxide) (PEO) hydrogel, a widely used thermoresponsive polymer with both upper and lower critical solution temperature phase behaviors [134]. The free energy of PEO in aqueous solutions can be formulated using the Dormidontova's model [135], which incorporates the free energy of both the PEO-water and water-water hydrogen bondings to successfully explain the unique phase behaviors of PEO/water solutions. Based on  $\bar{\chi}(T, \phi)$  derived from the Dormidontova's model (see Appendix A; here  $T$  represents temperature), we numerically calculate the  $T \sim \phi$  relation for both the free-shrinking and uniaxially constrained condition, as shown in Fig. 4.3a. Given a stimulus of temperature  $T_i \rightarrow T_f$ , we imagine that a free-shrinking PEO hydrogel undergoes an isotropic contraction from  $\phi_i$  to  $\phi_f$  with a contraction ratio of  $\alpha_0$  along each dimension, while a uniaxially constrained PEO hydrogel with a longitudinal prestrain  $\epsilon_{\parallel}$  shrinks from  $\phi'_i$  to  $\phi'_f$ . In a similar way as Fig. 4.2b, we calculate  $A_{\max}$  for  $-0.5 \leq \epsilon_{\parallel} \leq 1.0$  and  $0.050 \leq \phi_i \leq 0.275$  at a specified  $\alpha_0$  (see Fig. 4.3b). Using the same set of parameters, a similar diagram for a generic hydrogel with  $\phi$ -independent  $\chi$  is also constructed within the same range of  $\epsilon_{\parallel}$  and  $\phi_i$  for comparison purposes.

Results in Fig. 4.3b clearly indicate that the  $\phi$ -dependent  $\chi$  of PEO hydrogel alters the anisotropic contraction behavior by shifting the maximum of  $A_{\max}$  within the inspected range of  $\phi$  and  $\epsilon_{\parallel}$ . However, the prestretching mechanism to enhance the contraction anisotropy still works for PEO hydrogel:  $A_{\max}$  can be smaller than  $\alpha_0^{-3/2}$  only when  $\epsilon_{\parallel} > 0$ .

#### 4.4. Anisotropic contraction of fiber-reinforced hydrogels: finite element simulations

The finite dimensions of the fibers, which are absent in previous discussions, can introduce more complexity to the anisotropic contraction of hydrogels. Besides the inhomogeneous strain field around the fibers, compact packing of the oriented stiff fibers within a hydrogel may also dampen the

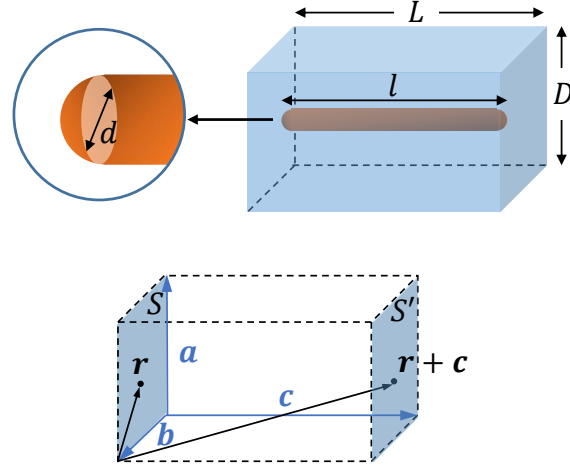


Figure 4.4. Schematics of the model geometry and periodic boundary conditions in the finite element simulations. Top right: The unit cell in rectangular solid shape with one rigid fiber embedded. Top left: The smoothed end of the fiber using a semi-sphere with the same radius as the fiber's. The bottom illustration shows the correspondence between points on the opposite faces of a unit cell.

overall contractions along the transverse directions. Meanwhile, the finite length of the fibers allows the hydrogel to shrink along the longitudinal direction instead of being completely constrained. As a result, the anisotropic behavior of the hydrogel significantly deviates from a uniaxially constrained hydrogel when the fibers have finite dimensions. Unfortunately, analytical solutions are difficult to obtain when the fibers are included in the model. Various approaches have been proposed in former research for numerical simulations of hydrogels [136, 41, 48, 137, 138]. In particular, the finite element method is well suited for understanding swelling hydrogels in complex geometries such as wrinkling, creasing, and other intriguing buckled structures [139, 140, 141, 142]. Therefore, we resort to the finite element method to explore the anisotropic contraction of a fiber-reinforced hydrogel in the following sections.

#### 4.4.1. Model geometry and boundary conditions

In our simulations, each fiber is modeled as a rigid cylinder with diameter  $d$  and length  $l$  attaching to the surrounding hydrogel matrix without allowing any relative sliding (see Fig. 4.4, top left). The ends of each fiber are smoothed with semi-spherical cups to avoid singular stress concentration at sharp corners. We arrange the fibers periodically within the hydrogel so that periodic boundary conditions can be applied to the model. Specifically, the periodic array of fibers and their surrounding hydrogel are described as identical unit cells spanned by a set of lattice vectors  $(\mathbf{a}, \mathbf{b}, \mathbf{c})$ . Let  $S$  and  $S'$  be the opposite faces along the direction of  $\mathbf{c}$  (see Fig. 4.4, bottom),  $\mathbf{u}(\mathbf{r})$  represent the displacement of an arbitrary point located at  $\mathbf{r}$  on  $S$  (thus  $\mathbf{u}(\mathbf{r} + \mathbf{c})$  lies on  $S'$ ), and  $(\mathbf{a}', \mathbf{b}', \mathbf{c}')$  denote the lattice vectors after deformation; the periodic boundary conditions require

$$(4.21) \quad \mathbf{u}(\mathbf{r} + \mathbf{c}) - \mathbf{u}(\mathbf{r}) = \mathbf{c}' - \mathbf{c}$$

which connects the local displacement vector of the unit cell with the global deformation of the lattice. In finite element simulations, the right-hand side of Eq. 4.21 is replaced with the displacement of a dummy node which is defined as

$$(4.22) \quad \mathbf{u}_c = \mathbf{c}' - \mathbf{c}$$

In our model,  $\mathbf{u}_c$  is not prescribed *a priori* but determined by the contraction behavior of the fiber-reinforced hydrogel. Therefore, constraints among the two opposite faces and the dummy node are enforced in our simulations to solve  $\mathbf{u}_c$  according to Eq. 4.21 and 4.22. Similar constraints can also be derived for the other two pairs of opposite faces. In ABAQUS, these constraints are implemented using `mdb.models[name].Equation` in Python script; an example code snippet is shown below:

---

```

1 dim = {'X': 1, 'Y': 2, 'Z': 3}
2 for C in ['X', 'Y', 'Z']:
3     mdb.models[name].Equation(
4         name = 'PBC-' + C + '-' + str(dim[C]),
5         terms = (
6             (1.0, 'RIGHT_FACE', dim[C]),
7             (-1.0, 'LEFT_FACE', dim[C]),
8             (-1.0, 'DUMMY', dim[C]),
9         )
10    )

```

---

The periodic boundary conditions provide a simple and intuitive approach to investigate the anisotropic behavior of the hydrogel induced by the distributed fibers. However, it is worth mentioning that although previous experiments have verified the orientational long range order of the fibers, no periodicity is found in the positions of the fibers. Therefore, it is apparently an idealization to use the periodic boundary conditions in our simulations.

The unit cell in our simulations is modeled using a rectangular solid with  $|a| = |b| = D$  and  $|c| = L$ , as illustrated in the Fig. 4.4 (topright). Here we assume that the unit cell has identical periodicity in the directions of  $a$  and  $b$ . Within each unit cell, a cylindrical fiber is symmetrically placed in the center and oriented to the direction of  $c$ ; thus  $L$  represents the longitudinal fiber-fiber distance, and the corresponding contraction ratio is  $\alpha_{\parallel}$ . Likewise  $D$  should be equal to the transverse fiber-fiber distance;  $\alpha_{\perp}$  is the transverse contraction ratio as previously defined.

#### 4.4.2. Constitutive model of hydrogel

We proceed to derive the constitutive model of the hydrogel within the context of finite element method. The thermodynamic equilibrium is achieved when the external work done on the hydrogel is equal to the change in the free energy:

$$(4.23) \quad \delta F = \int_V \delta \bar{F} dV = \int_V B_i \delta u_i dV + \int_S T_i \delta u_i dS$$

where  $\bar{F}$  is the nominal free energy density of the hydrogel,  $B_i$  is the external body force,  $T_i$  is the surface traction, and  $\delta u_i$  are arbitrary perturbation displacements. When the hydrogel reaches equilibrium, its chemical potential  $\mu = \mu_{\text{external}} = 0$ ; thus in Eq. 4.23 we neglect the work done by the external chemical potential of the water.

Eq. 4.23 possesses the same form as a hyperelastic solid, which enables us to implement a finite element method for a hydrogel. In the context of continuum mechanics, it is traditional to formulate the free energy density  $\bar{F}$  in terms of the strain invariants:

$$(4.24) \quad I_1 = \lambda_1^2 + \lambda_2^2 + \lambda_3^2 \quad \text{and} \quad J = \lambda_1 \lambda_2 \lambda_3 = \phi^{-1}$$

Substituting Eq. 4.24 to 4.2 and 4.3 gives

$$(4.25) \quad \begin{aligned} \bar{F}(I_1, J, T) &= \frac{1}{2} \frac{N}{V_m} kT(I_1 - 3 - \ln J) \\ &+ \frac{kT}{\nu} \left[ (J - 1) \ln \left( 1 - \frac{1}{J} \right) + \chi \left( 1 - \frac{1}{J} \right) \right] \end{aligned}$$

Eq. 4.25 is singular at the molten state of the hydrogel ( $J = 1$ ), which may lead to numerical problems if the molten state is involved in the calculations. To overcome this difficulty, we use an isotropic free swollen state with  $J > 1$  as the reference state inspired by the study of Hong *et al* [136]. At this reference state, the hydrogel has isotropic stretching ratio  $\lambda_0$  relative to the molten state. The volume fraction of the polymer is denoted by  $\phi_0 = \lambda_0^{-3}$ . Because the volume of the polymer  $V_m$  is assumed to be conserved,  $\phi$  and  $\phi_0$  can be connected via

$$(4.26) \quad V\phi = V_0\phi_0 = V_m$$

where  $V_0$  is the volume of the hydrogel at the reference state. The nominal free energy density  $\bar{F}$  and the strain invariants  $I_1, J$  are converted correspondingly to  $\bar{F}', I'_1, J'$  with respect to the new

reference state:

$$(4.27) \quad \begin{aligned} \bar{F}(I_1, J, T)V_m &= \bar{F}'(I'_1, J', T)V_0 \\ I_1 &= \phi_0^{-2/3}I'_1 \quad \text{and} \quad J = \phi_0^{-1}J' \end{aligned}$$

Substituting Eq. 4.26 and 4.27 to 4.25, we obtain that

$$(4.28) \quad \begin{aligned} \bar{F}'(I'_1, J', T) &= \frac{kT}{\nu} \left[ \frac{1}{2} \frac{N\nu}{V_m} \phi_0 \left( \phi_0^{-2/3} I'_1 - 3 - \ln \frac{J'}{\phi_0} \right) \right. \\ &\quad \left. + (J' - \phi_0) \ln \left( 1 - \frac{\phi_0}{J'} \right) + \chi \phi_0 \left( 1 - \frac{\phi_0}{J'} \right) \right] \end{aligned}$$

We implement the above constitutive model of the hydrogel by developing a user-defined subroutine for a hyperelastic material (UHYPER) in the commercial code ABAQUS (see Appendix B). The temperature is exploited as a uniform field parameter to control the contraction of the hydrogel in the following steps:

- (1) Calculate  $\chi_i$  and  $\chi_f$  Eq. 4.7 with the input values of  $\phi_i$ ,  $N\nu/V_m$  and  $\alpha_0$ .
- (2) Assuming a linear dependence of  $\chi$  on temperature:  $\chi = A + BT$ , calculate the value of  $A$  and  $B$  using  $(\chi_i, T_i)$  and  $(\chi_f, T_f)$ ;  $T_i$  and  $T_f$  are initial and final temperature respectively, and they are preset parameters in the simulations.
- (3) Use  $(N\nu/V_m, A, B, \phi_i)$  as the parameters for the UHYPER subroutine.
- (4) Set the initial temperature as  $T_i$  ( `mdb.models[name].Temperature` in Python script).
- (5) Set the final temperature as  $T_f$  ( `mdb.models[name].predefinedFields [fieldName].setValuesInStep` in Python script).

Due to the change of the temperature, a nontrivial stress field emerges such that the hydrogel needs to contract to reach the osmotic equilibrium.

Table 4.1. Parameters for finite element modeling of the fiber-reinforced hydrogel. The notation of the geometrical parameters follows the same as Fig. 4.4.

Geometry (nm)	Element
$d$	10
$l$	Vary from 25 ~ 500
$L$	Vary from 200 ~ 800
$D$	Vary from 20 ~ 67.5
Materials	Boundary conditions
$N\nu/V_m$	C3D8R, Enhanced hourglass control
$\phi_i$	Fiber surfaces Encastered
$\alpha_0$	Unit cell surfaces Periodic boundary conditions
Predefined field (K)	
$T_i$	298
$T_f$	363

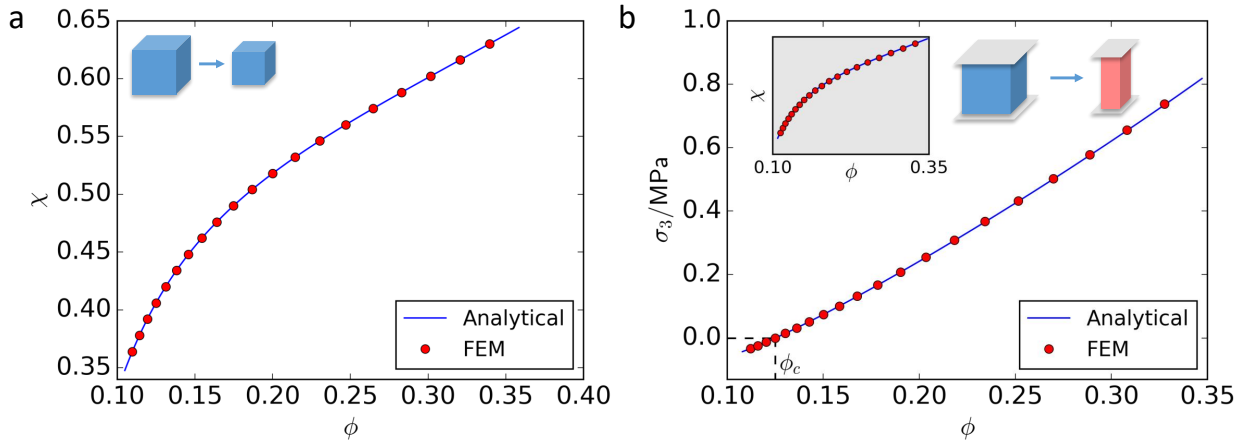


Figure 4.5. Verification of the implementation of the finite element user-defined subroutine. (a)  $\chi \sim \phi$  plot of a free swelling hydrogel. (b) The stress  $\sigma_3$  along the constrained direction for a uniaxially constrained hydrogel. At  $\phi = \phi_c$ , the stress vanished as expected. The inset illustrate the corresponding  $\chi \sim \phi$  curve of the uniaxially constrained hydrogel.

The simulation parameters are listed in Table 4.1 unless otherwise noted. No prestretching is involved in our simulations ( $\phi_i = \phi'_i = \phi_c$ ), as we are focusing on the effects of the fiber dimensions; prestretching may also induce excessive deformations which lead to convergence difficulties.

To verify our implementation, we numerically calculate the  $\chi \sim \phi$  relations for both an isotropic swelling hydrogel and a uniaxially constrained hydrogel. (see Fig. 4.5) The results show perfect

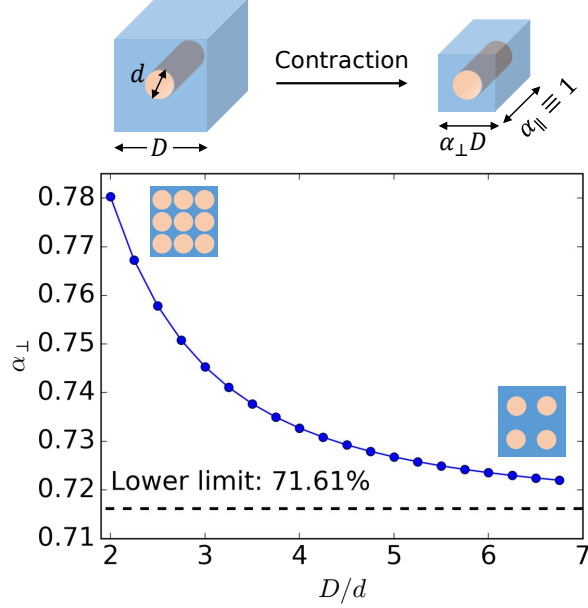


Figure 4.6. The transverse contraction ratio of the fiber-reinforced hydrogel as a function of the transverse fiber-fiber distance at  $L/l = 1$ . The fiber is modeled as a regular cylindrical rod throughout the hydrogel matrix rather than a smoothed one to avoid possible numerical difficulties. The simulations are performed with  $d = 10$  nm and  $L = l = 30$  nm. The lower limit is calculated from the contraction of a uniaxially constrained hydrogel illustrated in Fig. 4.1a with the same set of parameters as used in the finite element simulations.

agreement with Eq.4.7 and 4.10. In addition, the calculated uniaxial stress  $\sigma_3$  for the uniaxially constrained hydrogel also coincides with Eq. 4.11 (see Fig. 4.5b).

#### 4.4.3. Results and discussions

We firstly perform simulations for a limiting case where the fiber length is identical to the longitudinal length of the unit cell ( $L/l = 1$ ), as shown in Fig. 4.6 (top). The hydrogel is therefore completely constrained along the orientation of the fibers ( $\alpha_{\parallel} \equiv 1$ ). Simulations show that the transverse contraction ratio  $\alpha_{\perp}$  decreases when increasing the transverse fiber-fiber distance (see Fig. 4.6 bottom). At small  $D/d$ , the transverse contraction of the hydrogel is highly restricted by the rigid cross-sections of the tightly packed fibers. This restriction become less significant as

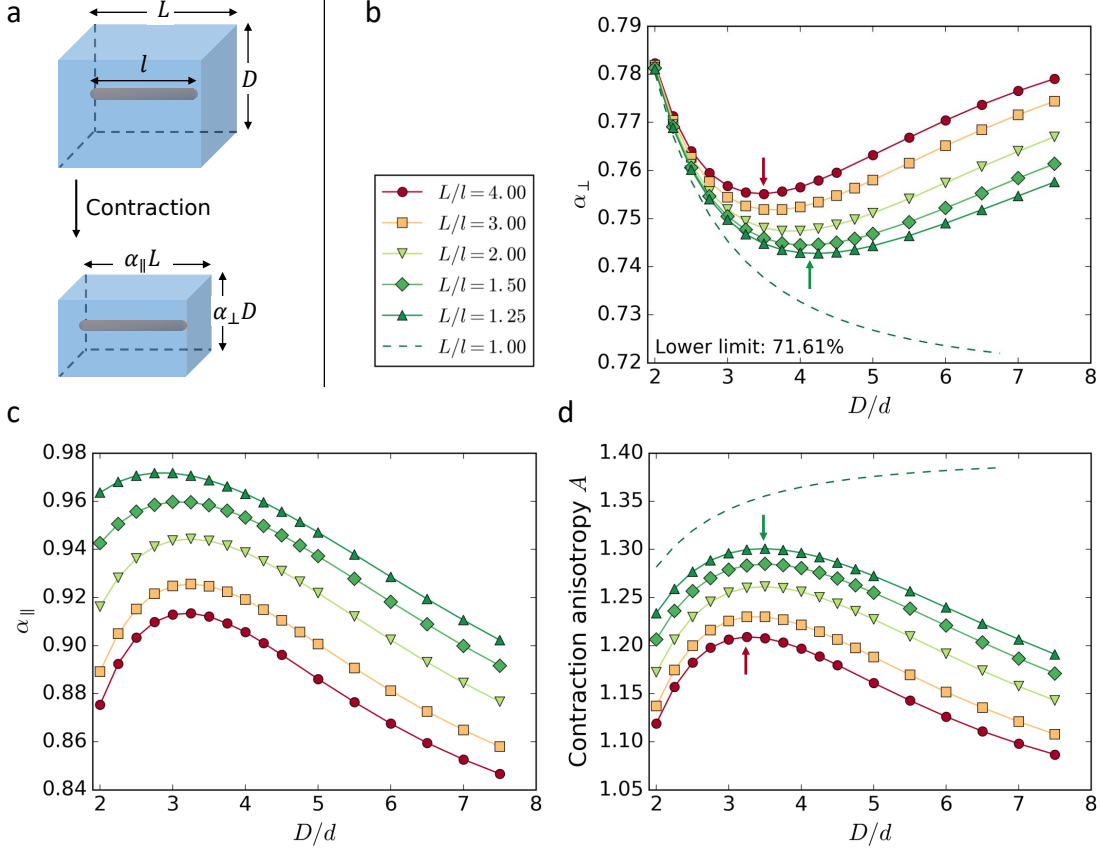


Figure 4.7. The anisotropic contraction of the fiber-reinforced hydrogel at  $L/l > 1.0$ . (a) Schematic of the geometry to model the anisotropic contraction when  $L > l$ . (b-d) The transverse contraction ratio (b), the longitudinal contraction ratio (c) and the contraction anisotropy (d) as functions of the reduced transverse fiber-fiber distance ( $D/d$ ). The data for  $L/l = 1$  in (b) (dashed curves) are identical to Fig. 4.6 as  $\alpha_{\parallel} \equiv 1$ . The arrows in both (b) and (d) indicate the shifts of the minimum  $\alpha_{\perp}$  and the maximum  $A$ . The legend in (b) is also shared by (c) and (d). All the simulations are performed with  $d = 10$  nm and  $l = 200$  nm.

$D/d$  increases, hence leading to stronger transverse contraction and decreasing  $\alpha_{\perp}$ . Eventually, the transverse dimensions of the fibers is negligible so that the hydrogel behaves as if it were uniaxially constrained without fibers embedded. Thus,  $\alpha_{\perp}$  converges to a lower limit that can be predicted from the uniaxially constrained hydrogel model discussed in previous sections. We also conduct similar simulations for a prestretching fiber-reinforced hydrogel; same behaviors of  $\alpha_{\perp}$  are found.

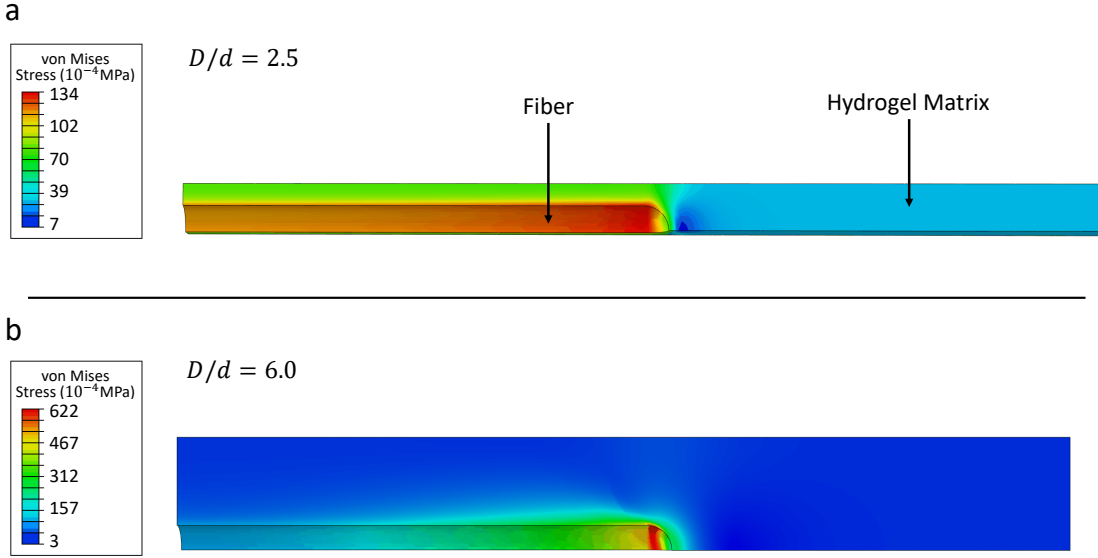


Figure 4.8. The von Mises stress distribution at (a)  $D/d = 2.5$  and (b)  $D/d = 6.0$ . Only one-eighth of unit cell is shown in the figure due to the symmetry of the model.

Intuitively, however, an infinitely large hydrogel with few fibers embedded (i.e.,  $D \gg d$ ) should shrink almost isotropically upon external stimuli, which can never be captured in the above simulations by assuming  $L/l = 1$  and  $\alpha_{\parallel} \equiv 1$ . Therefore, we proceed to investigate the anisotropic contraction at  $L/l > 1$  which allows the hydrogel to shrink longitudinally (see Fig. 4.7a). Figure 4.7b shows that the transverse contraction ratio  $\alpha_{\perp}$  has a minimum for each  $L/l$ , whereas  $\alpha_{\parallel}$  exhibits the opposite behavior (Fig. 4.7c). These results can be understood as follows. At small  $D/d$ , the transverse contraction can be significantly amplified by releasing the aforementioned restrictions from the rigid cross-sections of the fibers. In contrast, the longitudinal contraction is energetically disfavored due to the induced stress concentration near the ends of the fibers (see Fig. 4.8); meanwhile it is also restricted by the rigid length of the fibers. Consequently,  $\alpha_{\perp}$  exhibits rapid decrease at small  $D/d$  where increasing  $\alpha_{\parallel}$  is observed. When  $D/d$  becomes noticeably larger, both  $\alpha_{\perp}$  and  $\alpha_{\parallel}$  vary in the opposite way compared to the previous case. Stronger longitudinal contraction is instead preferred at large  $D/d$  when the fibers are more sparsely distributed: the bulky

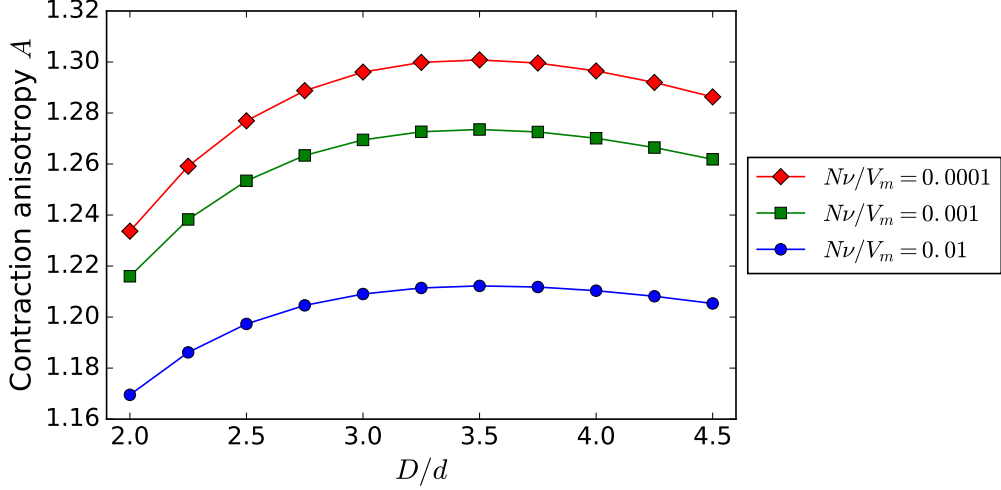


Figure 4.9. The contraction anisotropy at different  $Nv/V_m$ .  $L/l = 1.25$ .

hydrogel far from the fibers can undergo less longitudinal strain, thus mediating the local stress concentration near the fibers.

The anisotropy of the hydrogel contraction ( $A \equiv \alpha_{\parallel}/\alpha_{\perp}$ ) can be evaluated from Fig. 4.7b and 4.7c. As shown in Fig. 4.7d,  $A$  presents a maximum for each  $L/l$ , just as expected based on the behavior of  $\alpha_{\parallel}$  in Fig. 4.7c. A shift of the maxima toward higher  $D/d$  with decreasing  $L/l$  is observed in both Fig. 4.7b and Fig. 4.7d. Indeed, the stronger constraint from the fibers at lower  $L/l$  need to be balanced out with larger longitudinal contraction induced by increasing  $D/d$ , thus the optimum  $D/d$  increases when reducing  $L/l$ . Besides, we have also inspected the contraction anisotropies at different  $Nv/V_m$ , a dimensionless parameter characterizing the rigidity of the hydrogel; the maxima therein do not show any shift along the  $D/d$  axis (see Fig. 4.9). Additionally,  $A$  is observed to be enhanced at lower  $L/l$  in Fig. 4.7d. This increasing anisotropy stems from the dampening of the longitudinal contraction when decreasing  $L/l$ ; the longitudinal separation of the fibers is reduced such that the hydrogel has less freedom to shrink along the longitudinal direction. Overall, we conclude that the contraction anisotropy can be maximized by

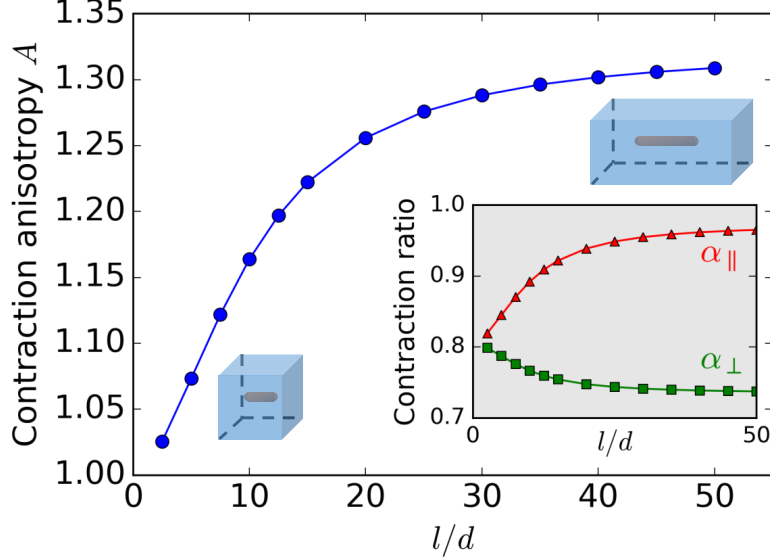


Figure 4.10. The contraction anisotropy of the fiber-reinforced hydrogel as a function of the shape aspect ratio of the fiber ( $l/d$ ).  $L/l = 2.0$ . The corresponding transverse contraction ratio ( $\alpha_{\perp}$ , green line) and longitudinal contraction ratio ( $\alpha_{\parallel}$ , red line) are depicted in the inset. The simulations are performed with  $d = 10$  nm and  $D = 40$  nm.

adjusting the transverse fiber-fiber distance  $D/d$ , and this maximum value can be further elevated by reducing the longitudinal fiber-fiber distance  $L/l$ .

Our simulations also reveal that fibers with larger aspect ratio ( $l/d$ ) can lead to stronger anisotropy of the hydrogel contractions. Note that  $L/l$  is kept as a constant for different  $l/d$  such that same portion of the hydrogel is restricted by the rigid fibers. Figure 4.10 clearly shows that  $A$  decreases with increasing  $l/d$ . More particularly, as depicted in the inset of Fig. 4.10,  $\alpha_{\parallel}$  exhibits a significant increase: at  $l/d = 5$ , it is only slightly larger than  $\alpha_0 = 0.8$ , whereas it reaches  $\sim 0.96$  when  $l/d$  increases to 50. The substantial increase of  $\alpha_{\parallel}$  at constant  $L/l$  implies that longer fibers can enforce much stronger longitudinal constraints on the hydrogel, thus facilitating the anisotropic contraction. This observation has been validated in former experiments [59, 73] where fibers with a high aspect ratio ( $l/d > 100$ ) are indeed adopted to achieve high anisotropy.

#### 4.5. Conclusions

This study focuses on the mechanisms controlling the anisotropic contraction of a fiber-reinforced hydrogel. By idealizing the reinforcement of the fibers as a uniaxial constraint, and assuming  $\chi$  is independent of  $\phi$ , we discover that the contraction anisotropy has an upper bound determined by the prescribed isotropic contraction. Numerical analysis of the  $\chi \sim \phi$  relations further reveals that it is possible to exceed this limit by introducing longitudinal prestretching into the hydrogel; such mechanism also applies for certain practical systems with  $\phi$ -dependent  $\chi$  such as PEO hydrogels. Assuming the fibers are rigid and periodically distributed, finite element simulations show that the contraction anisotropy can be maximized by varying the transverse fiber-fiber distance; this maximum value can be further improved by reducing the longitudinal fiber-fiber distance or increasing the fiber length, both of which essentially strengthen the longitudinal constraint of the fibers. These findings provide insights into designing fiber-reinforced hydrogels with desired anisotropic behavior under various stimuli, which can be applicable in soft robotics, tissue engineering and so on. Future studies are needed to elucidate the potential impact of other important factors on the anisotropic contraction, including deformable fibers, different fiber arrangements and interactions between fibers and the hydrogel matrix.

## CHAPTER 5

### **Summary and Future Work**

#### **5.1. Summary**

The aim of my research is to model, understand, control and ultimately harness the nonlinear, complex deformations of gels to facilitate the design of bio-inspired materials with improved performance and novel functionalities, and to provide an in-depth knowledge on biological growth and development. To achieve this goal, three homogeneous or heterogeneous systems with different architectures and broad applications are considered. We start by investigating the complicated deformation of a homogeneous elastomeric structure that is widely adopted in advanced nanopatterning techniques: a periodic pyramid array in contact with a rigid substrate. Simulations clearly prove that the unexplained photoresist patterns in previous experiments stem from the distinct morphology of the deformed pyramid, which perfectly exemplify the significant role of large deformation in applications of soft materials. The scaling laws of such controllable deformations are also established and compared with experiments, which can be useful for designing bio-inspired devices, notably artificial skins with high pressure sensitivity.

Next we inspect the mechanical instability of a simple heterogeneous system: a bistrrip gel with different prestrains in each strip. Perversions and helices proliferate as a result of the helical symmetry breaking induced by the misfit of the two strips. It is numerically observed that, during the formation of perversions, the strain energy concentrates over each perversion, and distinct modes of energy transfer between the strips are identified. The repulsive nature of the perversion-perversion interaction and the coalescence of perversions are also presented and discussed. These findings

provide a fundamental understanding of the biological motifs present in growing tendrils [23] and animal guts [29].

Finally, we proceed to examine the anisotropic contraction of fiber-reinforced hydrogels, where the aligned fibrous heterogeneities are massively incorporated into gel networks. The theoretical and numerical analysis indicates that the contraction anisotropy can be enhanced by prestretching the hydrogels along the fiber direction; it can be further maximized by tuning the parameters of the fibrous microstructures such as the fiber radius, fiber length, and fiber-fiber distances. These results offer possible strategies for controlling the contraction anisotropy of fiber-reinforced hydrogels, therefore paving the way for creating artificial muscles and soft actuators with desired performance.

## 5.2. Recommended Future Work

### 5.2.1. Inverse Design Problem of Soft Structures

As an extended work of the bistrrip buckling introduced in Chapter 3, a more general problem is how to design a demanded soft structure by prescribing strains, growth rates, intrinsic curvatures and misfit heterogeneities in a homogeneous object. Solutions to this problem have broad engineering applications, particularly in advanced 3D printing techniques [59, 60, 143]. Combined with the stimuli-responsiveness of gels, it is also possible to construct versatile and active soft materials with tunable morphologies [144]. In addition, this problem has strong connections to biological growth and development. The recent work by van Rees *et. al.* [8] has demonstrated that with orthotropically growing thin bilayers, any target shape of surface can be attained from an isotropic flat state, as shown in Fig. 5.1. Therefore, there are great opportunities to conduct research on various inverse design problems of soft structures using analytical and numerical methods. For example, simulations can be performed to design the growing patterns of bilayers with significant thicknesses, and the nonlinear constitutive behavior of gels can also be considered.

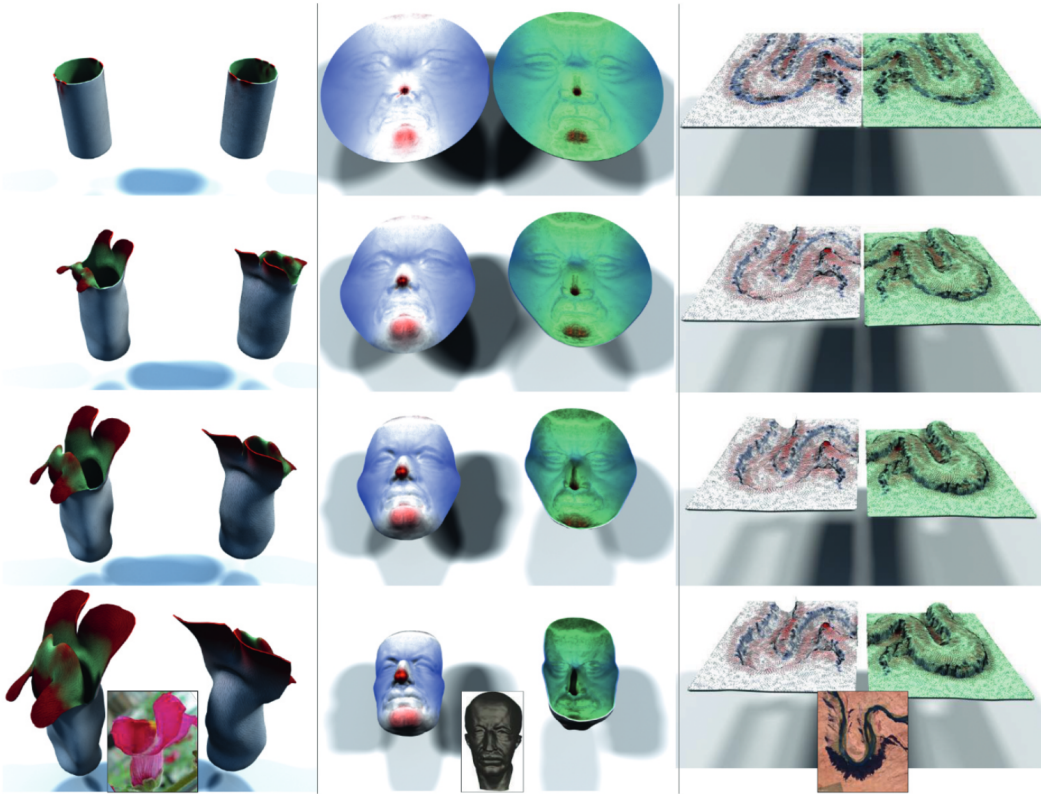


Figure 5.1. Inverse design of surfaces using bilayers with orthotropic growing directions. Three columns from left to right: the growing process of a snapdragon, a human face and a river horseshoe respectively. Within each column, the initial state (top), two intermediate states(middle) and final state (bottom) are shown. For each state, the growing factors of the top layer (left) and bottom layer (right) are illustrated. Adapted from [8]. Copyright 2017 National Academy of Sciences, U.S.A.

### 5.2.2. Double-Network Hydrogels with High Toughness

Besides the anisotropic response of hydrogels described in Chapter 4, another highly demanded feature in biomedical applications of hydrogels is high toughness (resistance to fracture). Most of the conventional synthetic hydrogels are mechanically weak and brittle to be used as substitutes for load-bearing soft tissues such as cartilage, ligaments and tendons [145]. The recently emerging double-network hydrogels (DN gels) are promising synthetic soft materials to achieve very high toughness (fracture energy of  $10^2 \sim 10^3 \text{ J/m}^2$ ) as well as mechanical strength (fracture tensile stress of  $1 \sim 10 \text{ MPa}$ ) which are comparable with cartilages [145, 146]. As the name suggests,

DN gels possess a heterogeneous structure with two contrasting polymer networks: the first one is rigid and brittle, usually a swollen polyelectrolyte network, and the second network is soft and loosely crosslinked. The high toughness of DN gels is therefore partially attributed to the effective energy dissipation by breaking bonds in the first network while keeping the second network intact. Extensive experimental works on DN gels have been performed in recent years, while the relative theoretical and computational works are limited. There are still open questions in producing novel DN gels: what is the effect of the second network structure and properties on the mechanical performance of the gels? How to increase the fatigue resistance of the gels to make it “self-heal” or “self-recover”? Multiscale computational models may shed some light on these questions by establishing the connections between the macroscopic mechanical properties of DN gels with the characteristics of the molecular-level architectures. For example, in atomic scale, molecular dynamics and Monte Carlo simulations can be carried out to investigate the structural and energetic information of the gel networks and intra-/inter-network interactions; in the macroscopic level, the finite element method can be employed to examine the energy dissipation and the fracture process of DN gels.

## Bibliography

- [1] Tallinen, T, Chung, J. Y, Rousseau, F, Girard, N, Lefèvre, J, & Mahadevan, L. (2016) On the growth and form of cortical convolutions. *Nature Physics* **12**, 588–593.
- [2] Klein, Y, Efrati, E, & Sharon, E. (2007) Shaping of elastic sheets by prescription of non-euclidean metrics. *Science* **315**, 1116–1120.
- [3] Zhao, R, Zhang, T, Diab, M, Gao, H, & Kim, K.-S. (2015) The primary bilayer ruga-phase diagram i: Localizations in ruga evolution. *Extreme Mechanics Letters* **4**, 76 – 82.
- [4] Cendula, P, Kiravittaya, S, Mei, Y. F, Deneke, C, & Schmidt, O. G. (2009) Bending and wrinkling as competing relaxation pathways for strained free-hanging films. *Physical Review B* **79**, 085429.
- [5] Liao, X, Braunschweig, A. B, Zheng, Z, & Mirkin, C. A. (2010) Force- and time-dependent feature size and shape control in molecular printing via polymer-pen lithography. *Small* **6**, 1082–1086.
- [6] Zhou, Y, Xie, Z, Brown, K. A, Park, D. J, Zhou, X, Chen, P, Hirtz, M, Lin, Q, Dravid, V. P, Schatz, G. C, Zheng, Z, & Mirkin, C. A. (2015) Apertureless cantilever-free pen arrays for scanning photochemical printing. *Small* **11**, 913–918.
- [7] Dowling, N. E. (2012) *Mechanical Behavior of Materials*. (Prentice Hall).

- [8] Rees, W. M. v, Vouga, E, & Mahadevan, L. (2017) Growth patterns for shape-shifting elastic bilayers. *Proceedings of the National Academy of Sciences* **114**, 11597–11602.
- [9] Flory, P. J. (1953) *Principles of polymer chemistry*. (Cornell University Press), p. 672.
- [10] Doi, M. (1996) *Introduction to Polymer Physics*. (Clarendon Press).
- [11] Tanaka, T, Sun, S.-T, Hirokawa, Y, Katayama, S, Kucera, J, Hirose, Y, & Amiya, T. (1987) Mechanical instability of gels at the phase transition. *Nature* **325**, 325796a0.
- [12] Trujillo, V, Kim, J, & Hayward, R. C. (2008) Creasing instability of surface-attached hydrogels. *Soft Matter* **4**, 564–569.
- [13] Matsuo, E. S & Tanaka, T. (1992) Patterns in shrinking gels. *Nature* **358**, 482–485.
- [14] Li, Y & Tanaka, T. (1992) Phase transitions of gels. *Annual Review of Materials Science* **22**, 243–277.
- [15] Koetting, M. C, Peters, J. T, Steichen, S. D, & Peppas, N. A. (2015) Stimulus-responsive hydrogels: Theory, modern advances, and applications. *Materials Science and Engineering: R: Reports* **93**, 1–49.
- [16] Hoare, T. R & Kohane, D. S. (2008) Hydrogels in drug delivery: Progress and challenges. *Polymer* **49**, 1993–2007.
- [17] Hoffman, A. S. (2012) Hydrogels for biomedical applications. *Advanced Drug Delivery Reviews* **64**, 18–23.
- [18] Kim, J. J & Park, K. (1998) Smart hydrogels for bioseparation. *Bioseparation* **7**, 177–184.

- [19] Shin, H, Jo, S, & Mikos, A. G. (2003) Biomimetic materials for tissue engineering. *Biomaterials* **24**, 4353–4364.
- [20] Richter, A, Paschew, G, Klatt, S, Lienig, J, Arndt, K.-F, & Adler, H.-J. P. (2008) Review on hydrogel-based ph sensors and microsensors. *Sensors* **8**, 561–581.
- [21] Yu, Q, Bauer, J. M, Moore, J. S, & Beebe, D. J. (2001) Responsive biomimetic hydrogel valve for microfluidics. *Applied Physics Letters* **78**, 2589–2591.
- [22] Huang, J, Liu, J, Kroll, B, Bertoldi, K, & Clarke, D. R. (2012) Spontaneous and deterministic three-dimensional curling of pre-strained elastomeric bi-strips. *Soft Matter* **8**, 6291–6300.
- [23] Gerbode, S. J, Puzey, J. R, McCormick, A. G, & Mahadevan, L. (2012) How the cucumber tendril coils and overwinds. *Science* **337**, 1087–1091.
- [24] Li, W, Huang, G, Yan, H, Wang, J, Yu, Y, Hu, X, Wu, X, & Mei, Y. (2012) Fabrication and stimuli-responsive behavior of flexible micro-scrolls. *Soft Matter* **8**, 7103–7107.
- [25] Abbott, J. J, Peyer, K. E, Lagomarsino, M. C, Zhang, L, Dong, L, Kaliakatsos, I. K, & Nelson, B. J. (2009) How should microrobots swim? *The International Journal of Robotics Research* **28**, 1434–1447.
- [26] Majidi, C, Kramer, R, & Wood, R. J. (2011) A non-differential elastomer curvature sensor for softer-than-skin electronics. *Smart Materials and Structures* **20**, 105017.
- [27] Kim, D & Rogers, J. A. (2008) Stretchable electronics: Materials strategies and devices. *Advanced Materials* **20**, 4887–4892.

- [28] Yin, J, Cao, Z, Li, C, Sheinman, I, & Chen, X. (2008) Stress-driven buckling patterns in spheroidal core/shell structures. *Proceedings of the National Academy of Sciences* **105**, 19132–19135.
- [29] Savin, T, Kurpios, N. A, Shyer, A. E, Florescu, P, Liang, H, Mahadevan, L, & Tabin, C. J. (2011) On the growth and form of the gut. *Nature* **476**, 57–62.
- [30] Young, C.-D, Wu, J.-R, & Tsou, T.-L. (1998) High-strength, ultra-thin and fiber-reinforced phema artificial skin. *Biomaterials* **19**, 1745–1752.
- [31] Haque, M, Kamita, G, Kurokawa, T, Tsujii, K, & Gong, J. (2010) Unidirectional alignment of lamellar bilayer in hydrogel: One-dimensional swelling, anisotropic modulus, and stress/strain tunable structural color. *Advanced Materials* **22**, 5110–5114.
- [32] Chau, M, France, K. J, Kopera, B, Machado, V. R, Rosenfeldt, S, Reyes, L, Chan, K. J, Förster, S, Cranston, E. D, Hoare, T, & Kumacheva, E. (2016) Composite hydrogels with tunable anisotropic morphologies and mechanical properties. *Chemistry of Materials* **28**, 3406–3415.
- [33] Rafat, M, Li, F, Fagerholm, P, Lagali, N. S, Watsky, M. A, Munger, R, Matsuura, T, & Griffith, M. (2008) Peg-stabilized carbodiimide crosslinked collagen–chitosan hydrogels for corneal tissue engineering. *Biomaterials* **29**, 3960–3972.
- [34] Drury, J. L & Mooney, D. J. (2003) Hydrogels for tissue engineering: scaffold design variables and applications. *Biomaterials* **24**, 4337–4351.
- [35] Agrawal, A, Rahbar, N, & Calvert, P. D. (2013) Strong fiber-reinforced hydrogel. *Acta Biomaterialia* **9**, 5313–5318.

- [36] Huang, Y, King, D. R, Sun, T. L, Nonoyama, T, Kurokawa, T, Nakajima, T, & Gong, J. P. (2017) Energy-dissipative matrices enable synergistic toughening in fiber reinforced soft composites. *Advanced Functional Materials* **27**, 1605350.
- [37] Illeperuma, W. R, Sun, J.-Y, Suo, Z, & Vlassak, J. J. (2014) Fiber-reinforced tough hydrogels. *Extreme Mechanics Letters* **1**, 90–96.
- [38] Ionov, L. (2014) Hydrogel-based actuators: possibilities and limitations. *Materials Today* **17**, 494–503.
- [39] Flory, P. J & Rehner, J. (1943) Statistical mechanics of cross-linked polymer networks ii. swelling. *The Journal of Chemical Physics* **11**, 521.
- [40] Hong, W, Zhao, X, & Suo, Z. (2010) Large deformation and electrochemistry of polyelectrolyte gels. *Journal of the Mechanics and Physics of Solids* **58**, 558–577.
- [41] Marcombe, R, Cai, S, Hong, W, Zhao, X, Lapusta, Y, & Suo, Z. (2010) A theory of constrained swelling of a ph-sensitive hydrogel. *Soft Matter* **6**, 784–793.
- [42] Liu, Z, Toh, W, & Ng, T. (2015) Advances in mechanics of soft materials: A review of large deformation behavior of hydrogels. *International Journal of Applied Mechanics* **07**, 1530001.
- [43] Han, Y, Hong, W, & Faidley, L. (2011) Coupled magnetic field and viscoelasticity of ferrogel. *International Journal of Applied Mechanics* **03**, 259–278.
- [44] Wall, F. T & Flory, P. J. (1951) Statistical thermodynamics of rubber elasticity. *The Journal of Chemical Physics* **19**, 1435–1439.
- [45] Bower, A. F. (2009) *Applied Mechanics of Solids*. (CRC Press).

- [46] Deng, H & Pence, T. (2010) Shear induced loss of saturation in a fluid infused swollen hyperelastic cylinder. *International Journal of Engineering Science* **48**, 624–646.
- [47] Westbrook, K. K & Qi, H. J. (2008) Actuator designs using environmentally responsive hydrogels. *Journal of Intelligent Material Systems and Structures* **19**, 597–607.
- [48] Chester, S. A & Anand, L. (2010) A coupled theory of fluid permeation and large deformations for elastomeric materials. *Journal of the Mechanics and Physics of Solids* **58**, 1879–1906.
- [49] Tanaka, T & Fillmore, D. J. (1979) Kinetics of swelling of gels. *The Journal of Chemical Physics* **70**, 1214–1218.
- [50] Sun, J.-Y, Zhao, X, Illeperuma, W. R, Chaudhuri, O, Oh, K, Mooney, D. J, Vlassak, J. J, & Suo, Z. (2012) Highly stretchable and tough hydrogels. *Nature* **489**, nature11409.
- [51] Xia, Y & Whitesides, G. M. (1998) Soft lithography. *Annual Review of Materials Science* **28**, 153–184.
- [52] Huo, F, Zheng, Z, Zheng, G, Giam, L. R, Zhang, H, & Mirkin, C. A. (2008) Polymer pen lithography. *Science* **321**, 1658–1660.
- [53] Sultan, E & Boudaoud, A. (2007) The buckling of a swollen thin gel layer bound to a compliant substrate. *Journal of Applied Mechanics* **75**, 051002.
- [54] Guo, Q, Mehta, A. K, Grover, M. A, Chen, W, Lynn, D. G, & Chen, Z. (2014) Shape selection and multi-stability in helical ribbons. *Applied Physics Letters* **104**, 211901.

- [55] Chen, Z. (2015) Shape transition and multi-stability of helical ribbons: a finite element method study. *Archive of Applied Mechanics* **85**, 331–338.
- [56] Palleau, E, Morales, D, Dickey, M. D, & Velev, O. D. (2013) Reversible patterning and actuation of hydrogels by electrically assisted ionoprinting. *Nature Communications* **4**, 2257.
- [57] Aharoni, H, Sharon, E, & Kupferman, R. (2014) Geometry of thin nematic elastomer sheets. *Physical Review Letters* **113**.
- [58] Erb, R. M, Sander, J. S, Grisch, R, & Studart, A. R. (2013) Self-shaping composites with programmable bioinspired microstructures. *Nature Communications* **4**, 1712.
- [59] Gladman, A. S, Matsumoto, E. A, Nuzzo, R. G, Mahadevan, L, & Lewis, J. A. (2016) Biomimetic 4d printing. *Nature Materials* **15**, 413–418.
- [60] Ding, Z, Yuan, C, Peng, X, Wang, T, Qi, J. H, & Dunn, M. L. (2017) Direct 4d printing via active composite materials. *Science Advances* **3**, e1602890.
- [61] Dawson, C, Vincent, J. F. V, & Rocca, A.-M. (1997) How pine cones open. *Nature* **390**, 37745.
- [62] Armon, S, Efrati, E, Kupferman, R, & Sharon, E. (2011) Geometry and mechanics in the opening of chiral seed pods. *Nature* **333**, 1726–1730.
- [63] Kim, Y, Liu, M, Ishida, Y, Ebina, Y, Osada, M, Sasaki, T, Hikima, T, Takata, M, & Aida, T. (2015) Thermoresponsive actuation enabled by permittivity switching in an electrostatically anisotropic hydrogel. *Nature Materials* **14**, 1002–1007.

- [64] Qiu, G & Pence, T. (1997) Remarks on the behavior of simple directionally reinforced incompressible nonlinearly elastic solids. *Journal of Elasticity* **49**, 1–30.
- [65] Agoras, M, Lopez-Pamies, O, & CastaÑeda, P. P. (2009) A general hyperelastic model for incompressible fiber-reinforced elastomers. *Journal of the Mechanics and Physics of Solids* **57**, 268–286.
- [66] Brun, M, Lopez-Pamies, O, & CastaÑeda, P. P. (2007) Homogenization estimates for fiber-reinforced elastomers with periodic microstructures. *International Journal of Solids and Structures* **44**, 5953–5979.
- [67] Nardinocchi, P, Pezzulla, M, & Teresi, L. (2015) Anisotropic swelling of thin gel sheets. *Soft matter* **11**, 1492–1499.
- [68] Liu, Y, Zhang, H, Zhang, J, & Zheng, Y. (2015) Constitutive modeling for polymer hydrogels: A new perspective and applications to anisotropic hydrogels in free swelling. *European Journal of Mechanics - A/Solids* **54**, 171–186.
- [69] Khennane, A. (2013) *Introduction to Finite Element Analysis Using MATLAB® and Abaqus*. (CRC Press).
- [70] Holzapfel, G. (2000) *Nonlinear Solid Mechanics: A Continuum Approach for Engineering*. (Wiley).
- [71] Destrade, M & Ogden, R. W. (2010) On the third- and fourth-order constants of incompressible isotropic elasticity. *The Journal of the Acoustical Society of America* **128**, 3334–3343.
- [72] Smith, M. (2014) *ABAQUS/Standard User's Manual, Version 6.14*. (SIMULIA).

- [73] Chin, S. M, Synatschke, C. V, Liu, S, Nap, R. J, Wang, Q, Álvarez Pinto, Z, Edelbrock, A. N, Fyrner, T, Palmer, L. C, Szleifer, I, Cruz, M. O. d. l, & Stupp, S. I. (2017) Covalent-supramolecular hybrid polymers as muscle-inspired anisotropic actuators. *In preparation.*
- [74] Liddle, A. J & Gallatin, G. M. (2016) Nanomanufacturing: A perspective. *ACS Nano* **10**, 2995–3014.
- [75] Giam, L. R & Mirkin, C. A. (2011) Cantilever-free scanning probe molecular printing. *Angewandte Chemie International Edition* **50**, 7482–7485.
- [76] He, Q, Tan, C, & Zhang, H. (2017) Recent advances in cantilever-free scanning probe lithography: High-throughput, space-confined synthesis of nanostructures and beyond. *ACS Nano* **11**, 4381–4386.
- [77] Huo, F, Zheng, G, Liao, X, Giam, L. R, Chai, J, Chen, X, Shim, W, & Mirkin, C. A. (2010) Beam pen lithography. *Nature Nanotechnology* **5**, 637–640.
- [78] Shim, W, Braunschweig, A. B, Liao, X, Chai, J, Lim, J, Zheng, G, & Mirkin, C. A. (2011) Hard-tip, soft-spring lithography. *Nature* **469**, 516–520.
- [79] Brinkmann, F, Hirtz, M, Greiner, A. M, Weschenfelder, M, Waterkotte, B, Bastmeyer, M, & Fuchs, H. (2013) Interdigitated multicolored bioink micropatterns by multiplexed polymer pen lithography. *Small* **9**, 3266–3275.
- [80] Bian, S, Zieba, S. B, Morris, W, Han, X, Richter, D. C, Brown, K. A, Mirkin, C. A, & Braunschweig, A. B. (2014) Beam pen lithography as a new tool for spatially controlled photochemistry, and its utilization in the synthesis of multivalent glycan arrays. *Chemical Science* **5**, 2023–2030.

- [81] Liao, X, Huang, Y.-K, Mirkin, C. A, & Dravid, V. P. (2017) High throughput synthesis of multifunctional oxide nanostructures within nanoreactors defined by beam pen lithography. *ACS nano* **11**, 4439–4444.
- [82] Agusil, J. P, Torras, N, Duch, M, Esteve, J, Pérez-García, L, Samitier, J, & Plaza, J. A. (2017) Highly anisotropic suspended planar-array chips with multidimensional sub-micrometric biomolecular patterns. *Advanced Functional Materials* **27**, 1605912.
- [83] Xie, Z, Gordiichuk, P, Lin, Q.-Y, Meckes, B, Chen, P.-C, Sun, L, Du, J. S, Zhu, J, Liu, Y, Dravid, V. P, & Mirkin, C. A. (2017) Solution-phase photochemical nanopatterning enabled by high-refractive-index beam pen arrays. *ACS nano* **11**, 8231–8241.
- [84] Eichelsdoerfer, D. J, Liao, X, Cabezas, M. D, Morris, W, Radha, B, Brown, K. A, Giam, L. R, Braunschweig, A. B, & Mirkin, C. A. (2013) Large-area molecular patterning with polymer pen lithography. *Nature Protocols* **8**, 2548–2560.
- [85] Sharp, K. G, Blackman, G. S, Glassmaker, N. J, Jagota, A, & Hui, C.-Y. (2004) Effect of stamp deformation on the quality of microcontact printing: A theory and experiment. *Langmuir* **20**, 6430–6438.
- [86] Hong, J. M, Ozkeskin, F. M, & Zou, J. (2008) A micromachined elastomeric tip array for contact printing with variable dot size and density. *Journal of Micromechanics and Microengineering* **18**, 015003.
- [87] Filipponi, L, Livingston, P, Kašpar, O, Tokárová, V, & Nicolau, D. V. (2016) Protein patterning by microcontact printing using pyramidal pdms stamps. *Biomedical Microdevices* **18**, 9.

- [88] Zhu, B, Niu, Z, Wang, H, Leow, W. R, Wang, H, Li, Y, Zheng, L, Wei, J, Huo, F, & Chen, X. (2014) Microstructured graphene arrays for highly sensitive flexible tactile sensors. *Small* **10**, 3625–3631.
- [89] Choong, C, Shim, M, Lee, B, Jeon, S, Ko, D, Kang, T, Bae, J, Lee, S. H, Byun, K, Im, J, Jeong, Y. J, Park, C. E, Park, J, & Chung, U. (2014) Highly stretchable resistive pressure sensors using a conductive elastomeric composite on a micropyramid array. *Advanced Materials* **26**, 3451–3458.
- [90] Chou, H.-H, Nguyen, A, Chortos, A, To, J. W, Lu, C, Mei, J, Kurosawa, T, Bae, W.-G, Tok, J. B.-H, & Bao, Z. (2015) A chameleon-inspired stretchable electronic skin with interactive colour changing controlled by tactile sensing. *Nature Communications* **6**, 8011.
- [91] Fan, F.-R, Lin, L, Zhu, G, Wu, W, Zhang, R, & Wang, Z. L. (2012) Transparent triboelectric nanogenerators and self-powered pressure sensors based on micropatterned plastic films. *Nano Letters* **12**, 3109–14.
- [92] Zhu, Y, Yang, B, Liu, J, Wang, X, Wang, L, Chen, X, & Yang, C. (2016) A flexible and biocompatible triboelectric nanogenerator with tunable internal resistance for powering wearable devices. *Scientific Reports* **6**, 22233.
- [93] Seol, M.-L, Lee, S.-H, Han, J.-W, Kim, D, Cho, G.-H, & Choi, Y.-K. (2015) Impact of contact pressure on output voltage of triboelectric nanogenerator based on deformation of interfacial structures. *Nano Energy* **17**, 63–71.
- [94] Kim, S, Wu, J, Carlson, A, Jin, S. H, Kovalsky, A, Glass, P, Liu, Z, Ahmed, N, Elgan, S. L, Chen, W, Ferreira, P. M, Sitti, M, Huang, Y, & Rogers, J. A. (2010) Microstructured

elastomeric surfaces with reversible adhesion and examples of their use in deterministic assembly by transfer printing. *Proceedings of the National Academy of Sciences* **107**, 17095–17100.

- [95] Jin, C & Qiao, Q. (2016) Deformation of pyramidal pdms stamps during microcontact printing. *Journal of Applied Mechanics* **83**, 071011.
- [96] Chen, Z, Huang, W, Zhang, X, & Yuen, M. M. (2016) *Modeling and Simulation of Electromechanical-Contact Based Elastomeric Pressure Sensor*. (2016 17th International Conference on Thermal, Mechanical and Multi-Physics Simulation and Experiments in Microelectronics and Microsystems (EuroSimE)), pp. 1–4.
- [97] Bean, K. E. (1978) Anisotropic etching of silicon. *IEEE Transactions on Electron Devices* **25**, 1185–1193.
- [98] Chaikin, P. M & Lubensky, T. C. (2000) *Principles of Condensed Matter Physics*. (Cambridge University Press).
- [99] Audoly, B & Pomeau, Y. (2010) *Elasticity and Geometry: From hair curls to the nonlinear response of shells*. (Oxford University Press).
- [100] Landau, L. D, Pitaevskii, L. P, Kosevich, A. M, & Lifshitz, E. M. (1986) *Theory of Elasticity, Third Edition: Volume 7*. (Butterworth-Heinemann).
- [101] Pham, J. T, Lawrence, J, Lee, D, Grason, G. M, Emrick, T, & Crosby, A. J. (2013) Highly stretchable nanoparticle helices through geometric asymmetry and surface forces. *Advanced Materials* **25**, 6703–6708.

- [102] Goriely, A & Tabor, M. (1998) Spontaneous helix hand reversal and tendril perversion in climbing plants. **80**, 1564–1567.
- [103] Dias, M. A & Santangelo, C. D. (2012) The shape and mechanics of curved-fold origami structures. *EPL (Europhysics Letters)* **100**, 54005.
- [104] Sun, Y, Choi, W, Jiang, H, Huang, Y. Y, & Rogers, J. A. (2006) Controlled buckling of semiconductor nanoribbons for stretchable electronics. *Nature Nanotechnology* **1**, 201–207.
- [105] Witten, T. (2007) Stress focusing in elastic sheets. **79**, 643–675.
- [106] Audoly, B & Boudaoud, A. (2003) Self-similar structures near boundaries in strained systems. *Physical Review Letters* **91**, 086105.
- [107] Darwin, C. (1888) *The movements and habits of climbing plants*. (D. Appleton).
- [108] Hotani, H. (1982) Micro-video study of moving bacterial flagellar filaments iii. cyclic transformation induced by mechanical force. *Journal of Molecular Biology* **156**, 791–806.
- [109] Guven, J, Huber, G, & Valencia, D. M. (2014) Terasaki spiral ramps in the rough endoplasmic reticulum. *Physical Review Letters* **113**, 188101.
- [110] Yazdi, N. H, Guet, C. C, Johnson, R. C, & Marko, J. F. (2012) Variation of the folding and dynamics of the escherichia coli chromosome with growth conditions. *Molecular Microbiology* **86**, 1318–1333.
- [111] Fisher, J. K, Bourniquel, A, Witz, G, Weiner, B, Prentiss, M, & Kleckner, N. (2013) Four-dimensional imaging of E. coli nucleoid organization and dynamics in living cells. *Cell* **153**, 882–895.

- [112] Goldstein, R, Goriely, A, Huber, G, & Wolgemuth, C. (2000) Bistable helices. *Physical review letters* **84**, 1631–4.
- [113] Sharon, E, Roman, B, Marder, M, Shin, G.-S, & Swinney, H. L. (2002) Mechanics: Buckling cascades in free sheets. *Nature* **419**, 579–579.
- [114] McMillen, T & Goriely, A. (2002) Tendril perversion in intrinsically curved rods. *12*, 241–281.
- [115] Domokos, G & Healey, T. J. (2005) Multiple helical perversions of finite, intristically curved rods. *15*, 871–890.
- [116] Liu, K, Cheng, C, Suh, J, Tang-Kong, R, Fu, D, Lee, S, Zhou, J, Chua, L. O, & Wu, J. (2014) Powerful, multifunctional torsional micromuscles activated by phase transition. *Advanced Materials* **26**, 1746–1750.
- [117] Martinez, R. V, Branch, J. L, Fish, C. R, Jin, L, Shepherd, R. F, Nunes, R. M, Suo, Z, & Whitesides, G. M. (2013) Robotic tentacles with three-dimensional mobility based on flexible elastomers. *Advanced Materials* **25**, 205–212.
- [118] Liu, J, Huang, J, Su, T, Bertoldi, K, & Clarke, D. R. (2014) Structural transition from helices to hemihelices. *PLoS ONE* **9**, e93183.
- [119] Irvine, W. T. M, Vitelli, V, & Chaikin, P. M. (2010) Pleats in crystals on curved surfaces. *Nature* **468**, 947–951.
- [120] Lipowsky, P, Bowick, M. J, Meinke, J. H, Nelson, D. R, & Bausch, A. R. (2005) Direct visualization of dislocation dynamics in grain-boundary scars. *Nature Materials* **4**, 407–411.

- [121] Bowick, M. J & Yao, Z. (2011) Crystalline order on catenoidal capillary bridges. *EPL (Europhysics Letters)* **93**, 36001.
- [122] Chan, V, Park, K, Collens, M. B, Kong, H, Saif, T. A, & Bashir, R. (2012) Development of miniaturized walking biological machines. *Scientific Reports* **2**, 857.
- [123] Dvir, T, Timko, B. P, Brigham, M. D, Naik, S. R, Karajanagi, S. S, Levy, O, Jin, H, Parker, K. K, Langer, R, & Kohane, D. S. (2011) Nanowired three-dimensional cardiac patches. *Nature Nanotechnology* **6**, 720–725.
- [124] Moutos, F. T, Freed, L. E, & Guilak, F. (2007) A biomimetic three-dimensional woven composite scaffold for functional tissue engineering of cartilage. *Nature Materials* **6**, 162–167.
- [125] Ahadian, S, Ramón-Azcón, J, Estili, M, Liang, X, Ostrovidov, S, Shiku, H, Ramalingam, M, Nakajima, K, Sakka, Y, Bae, H, Matsue, T, & Khademhosseini, A. (2014) Hybrid hydrogels containing vertically aligned carbon nanotubes with anisotropic electrical conductivity for muscle myofiber fabrication. *Scientific reports* **4**, 4271.
- [126] Wu, Z. L & Gong, J. P. (2011) Hydrogels with self-assembling ordered structures and their functions. *NPG Asia Materials* **3**, 57–64.
- [127] McClendon, M. T & Stupp, S. I. (2012) Tubular hydrogels of circumferentially aligned nanofibers to encapsulate and orient vascular cells. *33*, 5713–5722.
- [128] Visser, J, Melchels, F, Jeon, J. E, Bussel, E. M. v, Kimpton, L. S, Byrne, H. M, Dhert, W, Dalton, P. D, Hutmacher, D. W, & Malda, J. (2015) Reinforcement of hydrogels using three-dimensionally printed microfibres. *Nature Communications* **6**, 6933.

- [129] Merodio, J & Ogden, R. (2005) Mechanical response of fiber-reinforced incompressible non-linearly elastic solids. *International Journal of Non-Linear Mechanics* **40**, 213–227.
- [130] Flory, P. J & Rehner, J. (1943) Statistical mechanics of cross-linked polymer networks i. rubberlike elasticity. **11**, 512.
- [131] Anand, L. (1996) A constitutive model for compressible elastomeric solids. *Computational Mechanics* **18**, 339–355.
- [132] Boyce, M. C & Arruda, E. M. (2000) Constitutive models of rubber elasticity: A review. *Rubber Chemistry and Technology* **73**, 504–523.
- [133] Huggins, M. L. (1964) A revised theory of high polymer solutions. *Journal of the American Chemical Society* **86**, 3535–3540.
- [134] Bae, Y. C, Lambert, S. M, Soane, D. S, & Prausnitz, J. M. (1991) Cloud-point curves of polymer solutions from thermo-optical measurements. **24**, 4403–4407.
- [135] Dormidontova, E. E. (2002) Role of competitive peo–water and water–water hydrogen bonding in aqueous solution peo behavior. *Macromolecules* **35**, 987–1001.
- [136] Hong, W, Liu, Z, & Suo, Z. (2009) Inhomogeneous swelling of a gel in equilibrium with a solvent and mechanical load. *International Journal of Solids and Structures* **46**, 3282–3289.
- [137] Li, D, Zhang, Z, & Liew, K. (2014) A numerical framework for two-dimensional large deformation of inhomogeneous swelling of gels using the improved complex variable element-free galerkin method. *Computer Methods in Applied Mechanics and Engineering* **274**, 84–102.

- [138] Quesada-Pérez, M, Ramos, J, Forcada, J, & Martín-Molina, A. (2012) Computer simulations of thermo-sensitive microgels: quantitative comparison with experimental swelling data. *The Journal of chemical physics* **136**, 244903.
- [139] Ding, Z, Liu, Z, Hu, J, Swaddiwudhipong, S, & Yang, Z. (2013) Inhomogeneous large deformation study of temperature-sensitive hydrogel. *International Journal of Solids and Structures* **50**, 2610–2619.
- [140] Okumura, D, Kuwayama, T, & Ohno, N. (2014) Effect of geometrical imperfections on swelling-induced buckling patterns in gel films with a square lattice of holes. *International Journal of Solids and Structures* **51**, 154–163.
- [141] Lee, H, Zhang, J, Jiang, H, & Fang, N. X. (2012) Prescribed pattern transformation in swelling gel tubes by elastic instability. *Physical Review Letters* **108**, 214304.
- [142] Weiss, F, Cai, S, Hu, Y, Kang, M, Huang, R, & Suo, Z. (2013) Creases and wrinkles on the surface of a swollen gel. *Journal of Applied Physics* **114**, 073507.
- [143] Miao, S, Castro, N, Nowicki, M, Xia, L, Cui, H, Zhou, X, Zhu, W, Lee, S.-j, Sarkar, K, Vozzi, G, Tabata, Y, Fisher, J, & Zhang, L. G. (2017) 4d printing of polymeric materials for tissue and organ regeneration. *Materials Today*.
- [144] Kim, J, Hanna, J. A, Byun, M, Santangelo, C. D, & Hayward, R. C. (2012) Designing responsive buckled surfaces by halftone gel lithography. *Science* **335**, 1201–1205.
- [145] Gong, J. P. (2010) Why are double network hydrogels so tough? *Soft Matter* **6**, 2583–2590.

- [146] Chen, Q, Chen, H, Zhu, L, & Zheng, J. (2015) Fundamentals of double network hydrogels. *Journal of Materials Chemistry B* **3**, 3654–3676.
- [147] Baulin, V. A. (2003) Theses (Université Joseph-Fourier - Grenoble I). Membres de Jury  
Marcel Vallade Mohamed Daoud Albert Johner Loic Auvray Avi Halperin.

# Curriculum Vitae

Shuangping Liu

## **PERSONAL INFORMATION**

- Place of Birth: Changsha, Hunan, China; Born: 1988; Citizenship: China

EDUCATION

- Ph.D. Materials Science and Engineering

Northwestern University, Evanston, IL, 60201, USA December 2017 (expected)

- B.S. Physics

Eduan University, Shanghai, 200433, China July 2010

## PUBLICATIONS

- **Shuangping Liu**, Samuel I. Stupp, and Monica Olvera de la Cruz, “Anisotropic Contraction of Fiber-Reinforced Hydrogels” Prepared for submission to *Soft Matter*.
  - Stacey M. Chin, Christopher V. Synatschke, **Shuangping Liu**, Rikkert J. Nap, Qifeng Wang, Zaida Álvarez, Hussain Sangji, Alexandra N. Edelbrock, Timmy Fyrner, Liam C. Palmer, Igal Szleifer, Monica Olvera de la Cruz, Samuel I. Stupp, “Covalent-supramolecular hybrid polymers as muscle-inspired anisotropic actuators” Prepared for submission to *Nat. Mater.*

- **Shuangping Liu** and Monica Olvera de la Cruz, “Deformation of Elastomeric Pyramid Pen Arrays in Cantilever-free Scanning Probe Lithography” Submitted to *J. Polym. Sci. B*.
- **Shuangping Liu**, Zhenwei Yao, Kevin Chiou, Samuel I. Stupp and Monica Olvera de la Cruz, “Emergent perversions in the Buckling of Heterogeneous Elastic Strips” *Proc. Natl. Acad. Sci.*, **113**, 7100-7105 (2016).

## RESEARCH PRESENTATIONS

- Contributed talk on “Anisotropic Contraction of Fiber-Reinforced Hydrogels”, APS March Meeting, New Orleans, LA (2017)
- Poster Presentation “Shape and geometry: anisotropic contraction and dynamical assembly”, conference on Bio-Inspired Energy Science, Evanston, IL (2016)
- Contributed talk on “Perversions driven spontaneous symmetry breaking in heterogeneous elastic strips”, APS March Meeting, San Antonio, TX (2015)
- Contributed talk on “Spontaneous Formation and Evolution of the Perversions in Helical Structures”, APS March Meeting, Denver, CO (2014)

## APPENDIX A

### The Flory-Huggins Parameter of Poly(ethlyene oxide) (PEO) in Aqueous Solutions

We describe the PEO behavior in aqueous solutions with the Dormidontova's model [135] which is briefly introduced as follows. The free energy of PEO/water solutions is essentially formulated within the framework of Flory-Huggins theory. Each PEO chain has  $N$  monomers of volume  $v_p$ , and each water molecule is represented as a monomer of volume  $v$ , which is used as the reference volume for the free energy. The translational entropy contribution of the PEO solutions follows the same form as the Flory-Huggins theory:

$$(A.1) \quad \frac{F_{\text{trans}}}{kT} = \frac{v}{Nv_p} \phi \ln \phi + (1 - \phi) \ln(1 - \phi)$$

The interaction energy between PEO monomers and water without the hydrogen bondings involved is given by

$$(A.2) \quad \frac{F_{\text{int}}}{kT} = \chi \phi (1 - \phi)$$

Here  $\chi$  possesses the standard form  $A + B/T$ . According to the Dormidontova's model, the free energy due to the hydrogen bondings is presented in the form:

$$(A.3) \quad \begin{aligned} \frac{F_{\text{HB}}}{kT} &= 2\phi \frac{v}{v_p} \left[ p \ln p + (1 - p) \ln(1 - p) - p \frac{\Delta f_p}{kT} \right] \\ &+ 2(1 - \phi) \left[ q \ln q + (1 - q) \ln(1 - q) - q \frac{\Delta f_w}{kT} \right] \end{aligned}$$

$$\begin{aligned}
& + 2(1 - \phi) \left( 1 - q - p \frac{\phi}{1 - \phi} \frac{v}{v_p} \right) \ln \left( 1 - q - p \frac{\phi}{1 - \phi} \frac{v}{v_p} \right) \\
& - 2(1 - \phi) \left( q + p \frac{\phi}{1 - \phi} \frac{v}{v_p} \right) \ln \frac{2(1 - \phi)}{e} \\
& - 2(1 - \phi) \left[ q_0 \ln q_0 - q_0 \frac{\Delta f_w}{kT} + \right. \\
& \quad \left. 2(1 - q_0) \ln(1 - q_0) - q_0 \ln \frac{2}{e} \right]
\end{aligned}$$

where  $p$  represent the average fraction of hydrogen bonds between PEO and water, and  $q$  is the average fraction of association in water;  $q_0$  is the value of  $q$  at  $\phi = 0$ , i.e., the average fraction of association in pure water.  $\Delta f_p$  is the free energy of the formation of each PEO-water hydrogen bond, and  $\Delta f_w$  is the free energy of the formation of each water-water hydrogen bond. It is noteworthy that Eq. A.3 is obtained by subtracting the free energy of pure PEO ( $\phi = 1$ ) and water ( $\phi = 0$ ) from the mixed state. The detailed derivation of Eq. A.3 can be referred to Ref. [135, 147]. The total free energy per lattice site is therefore the sum of Eq. A.1, A.2 and A.3:

$$(A.4) \quad F = F_{\text{trans}} + F_{\text{int}} + F_{\text{HB}}$$

$p$  and  $q$  must satisfy  $\partial F / \partial p = 0$  and  $\partial F / \partial q = 0$  to minimize the total free energy, which delivers

$$(A.5) \quad \frac{p}{2(1 - p) \left[ (1 - \phi)(1 - q) - p\phi \frac{v}{v_p} \right]} = \exp \left( \frac{\Delta f_p}{kT} \right)$$

$$(A.6) \quad \frac{q}{2(1 - q) \left[ (1 - \phi)(1 - q) - p\phi \frac{v}{v_p} \right]} = \exp \left( \frac{\Delta f_w}{kT} \right)$$

The  $\phi$ -dependent  $\chi$  of PEO in aqueous solutions can be obtained by comparing Eq. A.1-A.3 with Eq. 4.3, and subsequently  $\bar{\chi}$  can be derived as:

$$(A.7) \quad \bar{\chi} = \chi + \frac{2}{\phi} \left( p \frac{v}{v_p} - q \right) + \frac{2}{\phi^2} \left[ q - q_0 + \ln \frac{q}{q_0(1-\phi)} \right]$$

Eq. A.7 exhibits a non-trivial dependence of  $\bar{\chi}$  on  $\phi$  which is in good agreement with experiments [147]. Using Eq. 4.20 to replace  $\chi$  in Eq. 4.7 and 4.10, and incorporating Eq. A.5-A.6, we are able to solve the  $T \sim \phi$  relations for PEO hydrogels as shown in Fig. 4.3a. All the parameters for our calculations are obtained from Ref. [135].

## APPENDIX B

**UHYPER Subroutine for Hydrogels**


---

```

1 SUBROUTINE UHYPER(BI1,BI2,AJ,U,UI1,UI2,UI3,TEMP,NOEL,
2 1 CMNAME,INCMPFLAG,NUMSTATEV,STATEV,NUMFIELDV,FIELDV,
3 2 FIELDVINC,NUMPROPS,PROPS)
4 !=====
5 !      UHYPER Subroutine for Abaqus/Standard
6 !      by Shuangping Liu, Oct 13, 2016
7 !
8 !      Swelling gel with Flory-Rehner free-energy. The Flory
9 !      interaction parameter  $\chi$  is given by
10 !       $\chi = \text{Chi}_A + \text{Chi}_B * T$ 
11 !      to get shrinking behavior at increasing temperature
12 !-----
13 !      Material properties:
14 !          PROPS(1) - Nv
15 !          PROPS(2) - Chi_A
16 !          PROPS(3) - Chi_B
17 !          PROPS(4) - phi0 - The volume fraction of the ref state
18 !          PROPS(5) - scale - Scale of the length
19 !      State variable:
20 !          TEMP: Temperature
21 !      Output:
22 !          Free-energy function ( $U_1$ , J) and its derivatives
23 !=====

24 !
25 INCLUDE 'ABA_PARAM.INC'
26
27 CHARACTER*80 CMNAME
28 DIMENSION U(2),UI1(3),UI2(6),UI3(6),STATEV(*),FIELDV(*),
29 1 FIELDVINC(*),PROPS(*)
30
31 REAL(8) Nv, kT_v, chi, chiA, chiB, phi0, scale
32
33 Nv = PROPS(1)
34 chiA = PROPS(2)
35 chiB = PROPS(3)
36 phi0 = PROPS(4)
37 scale = PROPS(5)
38 chi = chiA + chiB * TEMP
39 kT_v = 1.38064852E-23 / 2.99E-29 * TEMP * scale
40

```

---

```

41 U(1) = kT_v * (Nv / 2.0 * phi0 * (phi0**(-2.0/3.0) * BI1
42 &           * AJ**(2.0 / 3.0) - 3.0 - LOG(AJ / phi0))
43 &           - (AJ - phi0) * LOG(AJ / (AJ - phi0))
44 &           + chi * phi0 * (1.0 - phi0 / AJ))
45 U(2) = 0
46
47 UI1(1) = kT_v * Nv / 2.0 * phi0**(1.0 / 3.0) * AJ**(2.0 / 3.0)
48 UI1(2) = 0
49 UI1(3) = kT_v * (Nv / 3.0 * BI1 * phi0**(1.0 / 3.0)
50 &           * AJ**(-1.0 / 3.0) + (1 - Nv / 2.0) * phi0 / AJ
51 &           - LOG(AJ / (AJ - phi0)) + chi * phi0**2 / AJ**2)
52
53 IF (AJ <= phi0) THEN
54   U(1) = 1E30
55   UI1(3) = -1
56 END IF
57
58 UI2 = 0
59 UI2(3) = kT_v * (-Nv / 9.0 * BI1 * phi0**(1.0 / 3.0)
60 &           * AJ**(-4.0 / 3.0) - (1 - Nv / 2.0) * phi0 / AJ**2
61 &           + phi0 / AJ / (AJ - phi0) - 2.0 * chi * phi0**2 / AJ**3)
62 UI2(5) = kT_v * Nv / 3.0 * phi0**(1.0 / 3.0) * AJ**(-1.0 / 3.0)
63
64 UI3 = 0
65 UI3(4) = -kT_v * Nv / 9.0 * phi0**(1.0 / 3.0) * AJ**(-4.0 / 3.0)
66 UI3(6) = kT_v * (4.0 * Nv / 27.0 * BI1 * phi0**(1.0 / 3.0)
67 &           * AJ**(-7.0 / 3.0) + (2.0 - Nv) * phi0 / AJ**3
68 &           - phi0 * (2 * AJ - phi0) / (AJ * (AJ - phi0))**2
69 &           + 6 * chi * phi0**2 / AJ**4)
70
71 RETURN
72 END

```

---